

Computational design and additive manufacturing of electromagnetic coils

Présentée le 12 mai 2023

Faculté des sciences et techniques de l'ingénieur
Laboratoire d'actionneurs intégrés
Programme doctoral en manufacturing

pour l'obtention du grade de Docteur ès Sciences

par

Adrien Jean-Michel THABUIS

Acceptée sur proposition du jury

Prof. Y. Bellouard, président du jury
Prof. Y. Perriard, directeur de thèse
Prof. B. Dehez, rapporteur
Prof. C. Espanet, rapporteur
Prof. R. Logé, rapporteur

Science is a collaborative effort. The whole process depends on people being able to communicate their ideas openly, honestly and critically.

— Brian Cox

Acknowledgements

I would like to express my gratitude to the individuals who have contributed to my success and the completion of this thesis. The following lines will provide my acknowledgements and thanks to those who have made this achievement possible.

I am first grateful for the support and contributions of the many people who helped me on my learning journey at the Laboratory of Integrated Actuators (LAI) at EPFL. I am grateful to Prof. Yves Perriard for trusting me with this PhD, providing valuable guidance, and creating a supportive research environment. The positive atmosphere in the lab has been crucial to my success, and I am truly appreciative of his mentorship throughout my journey. Thank you to Xiaotao who supervised and guided me during this project. I learned a lot alongside you and will miss our long debates in front of the white board. Thank you to the pillars of the lab Paolo, Alexis, Christian, and Aline for their constant support and help. Many thanks to Yoan for his great ideas and guidance when I have encountered difficulties during the thesis. I feel grateful and fortunate to have had the opportunity to work alongside exceptional colleagues who made this adventure a memorable one. A special thank you to Sean, Patricio, Camilo, Raphael, Sofia, Pooneh, Kenny, and Thomas, who have been with me for most of my time at the laboratory, for their companionship, laughter, and shared experiences. I am also thankful to all the former and current lab members, including Armando, Stefania, Quentin, Marjan, Simon, Amine, Bhawnath, Ning, Marc, Francesco, Silje, Guillaume, Florian, Jonathan, Louis, Valentin, David, Xinchang, Trung and Morgan, for their contributions and for creating a vibrant and supportive lab atmosphere that made this journey truly enjoyable.

I extend my gratitude to the collaborators from ETEL, Alessandro, Daniele, and Ambroise, for their support, interest, and insightful contributions. My sincere thanks also go to the jury members, Prof. Roland Logé, Prof. Bruno Dehez, Prof. Christophe Espanet, and Prof. Yves Bellouard, for their time, valuable discussions, and feedback during the private defense. Lastly, I would like to thank Bruno Studach for his support and shared interest in additive manufacturing technologies.

During my thesis, I had the privilege of supervising several talented Master's students, and their work significantly contributed to the success of this project. My thanks go out to Elie, Gabriel, Andreas, Eloi, Pierre, Maribel, and Gybran for their hard work, dedication, and valuable contributions. I would also like to extend my gratitude to the unsung heroes who provided their support from the shadows. Specifically, I would like to thank the resourceful *dokken*, *kamensky*, and *sebastkm* from the FEniCS discourse forum, whose invaluable assistance helped me overcome some significant challenges when no one else could.

Acknowledgements

Je suis reconnaissant envers ma famille et mes amis pour leur soutien et encouragements tout au long de mon parcours académique. Je tiens aussi à remercier les différentes personnes qui ont partagé ma vie au cours de cette thèse. Mes anciens colocataires de Lausanne, Etienne et Aurélien, ainsi que Maude, ont été d'un grand soutien pendant la première moitié de ce parcours. Merci aussi à mon colocataire actuel, Guzmán, pour tous ces bons moments partagés. Je souhaite également remercier James pour nos pauses café quotidiennes sur le toit de Microcity, où nous avons tenté de refaire le monde ensemble. Ces moments vont me manquer.

Enfin, je suis incroyablement reconnaissant envers Delphine. Sa présence dans ma vie a été une source constante de bonheur et de motivation. Merci pour son amour, ses encouragements et son soutien continu tout au long de cette aventure.

Neuchâtel, April 26, 2023

Adrien Thabuis

Abstract

The modern world is heavily reliant on electromagnetic devices to convert mechanical energy into electrical energy and vice versa. These devices are fundamental to powering our society, and the growing need for automated production lines and electrified transportation is driving the demand for even more advanced electromagnetic actuators. A critical component of these devices is the electromagnetic coil, typically constructed from copper wire wound into simple shapes. Over the years, extensive research and industrial development have led to a deep understanding of this technology. Nevertheless, innovation is needed to improve upon state-of-the-art or to access applications with harsher requirements. In this thesis, we propose using additive manufacturing techniques to fabricate electromagnetic coils, which eliminates geometric limitations and opens up new design possibilities. We also utilize computational design methods, which reformulate the design problem as an optimization one. These tools generate complex shapes belonging to a broader solution set than the one accessible by a human designer.

The implemented method (topology optimization) investigates the ideal distribution of material in space. It first demonstrates the possibility of generating coils within a 2-D plane. This framework is expanded to consider the packing of multiple coils constituting motor windings without any assumptions on their position or shape. A 2.5-D approach is formulated to design overlapping coils while maintaining a low computational cost. A 3-D analysis is also explored for designing coils with different functions in an electromagnet manipulator. The generated designs exhibit significantly improved electromagnetic performance, such as a motor constant increased by 17% or regions with uniform magnetic field 7 times larger than the references. The feasibility of additively manufacturing electromagnetic coils is examined through a study case of a linear motor with a reference coil topology. Innovative design features, such as tracks with an evolving cross-section and "completed" linear windings, are proposed to fully harvest the design freedom provided by additive manufacturing. Additionally, we propose the concept of multi-functional windings, integrating heat sinks within the coils for improved efficiency and self-cooling capabilities. This results in the possibility of increasing the motor force by 17.3% without increasing the volume of permanent magnets or degrading the electric resistance of the winding. Prototypes of various coil geometries are fabricated and tested.

Overall, this thesis lays the foundation for a new generation of electromagnetic devices with improved performance through the combination of computational design methods and additive manufacturing technologies.

Abstract

Keywords: computational design, topology optimization, design optimization, electromagnetic coil, motor winding, electrical machines, additive manufacturing, 3D-printing, self-cooling coils

Résumé

Notre société moderne repose sur une abondance d'appareils électromagnétiques pour convertir l'énergie mécanique en électricité et vice versa. L'intérêt grandissant pour l'automatisation de la production et l'électrification de l'industrie du transport, renforce le besoin d'actionneurs électromagnétiques à hautes performances. L'un des éléments clés de ces appareils est la bobine électromagnétique traditionnellement composée d'un fil de cuivre bobiné. Afin d'atteindre des performances significativement plus élevées, une technologie disruptive est nécessaire. Nous proposons, dans cette thèse, d'utiliser des méthodes de fabrication additive pour réaliser les bobines électromagnétiques. Ces techniques permettent d'éliminer les limites sur la géométrie des pièces réalisées, laissant la possibilité à des formes plus variées. Nous utilisons aussi des méthodes de conception computationnelle, qui reformule le problème de conception, en un problème d'optimisation. Ces outils génèrent des formes complexes faisant parties d'un espace de solution plus grand que celui accessible par un concepteur humain.

La méthode implémentée (optimisation topologique) explore la distribution idéale de matière dans l'espace. Elle démontre premièrement la possibilité de générer des bobines dans un plan 2-D. Afin de résoudre des problèmes plus complexes, cette méthode est adaptée pour déterminer l'assemblage de multiples bobines formant un bobinage, sans connaissance requise de leur position initiale ou de leur forme. Une analyse dites "2.5-D" est proposée afin d'étendre les possibilités de conception à des bobines se chevauchant en dehors du plan tout en gardant un coût calcul raisonnable. La méthode a aussi été élargie à des problèmes 3-D au travers d'un problème de conception de bobines avec différentes fonctionnalités au sein d'un manipulateur électromagnétique. Les bobines générées atteignent des performances électromagnétiques significativement plus élevées comme une constante moteur augmentée de 17% ou une région avec une distribution uniforme de flux magnétique 7 fois plus grande que les références.

La faisabilité de fabriquer additivement des bobines électromagnétiques a aussi été validée. Ceci a été examiné au travers de l'étude d'un moteur linéaire et d'une forme de bobine référente. Des caractéristiques innovantes comme des pistes conductrices à section variable ou le concept de bobinage linéaire "complété" sont proposés pour démontrer la flexibilité de ces méthodes de fabrication. De plus, nous proposons le concept de bobine électromagnétique multifonctionnelles intégrant des radiateurs pour se refroidir toute seule et améliorer son efficacité. Cela aboutit à la possibilité d'augmenter la force des moteurs de 17.3% sans augmenter leur volume d'aimants permanents ou dégrader la résistance électrique du bobinage. Des

Résumé

prototypes de différentes géométries de bobines sont réalisés et testés.

Cette thèse établit les fondations d'une nouvelle génération d'appareils électromagnétiques à hautes-performances issue de la combinaison de méthodes de conception computationnelle et des technologies de fabrication additives

Mots clés : conception computationnelle, optimisation topologique, optimisation de design, méthodes numériques, bobine électromagnétique, bobinage de moteurs, machines électriques, fabrication additive, impression 3D, bobines auto-refroidissantes

Contents

Acknowledgements	i
Abstract	iii
Notation	ix
1 MOTIVATION	1
1.1 Introduction	2
1.2 Outlook	5
1.3 Context of the thesis.	6
2 STATE-OF-THE-ART	7
2.1 Computational design of electric conductors	8
2.1.1 Computational design	8
2.1.2 Topology optimization	9
2.1.3 Application to electric conductors	16
2.1.4 Room for improvement	20
2.2 Advanced manufacturing of electromagnetic coils	22
2.2.1 Winding types	22
2.2.2 Printed circuit board technology	23
2.2.3 Additive manufacturing technology	24
2.2.4 Room for improvement	27
3 COMPUTATIONAL DESIGN OF ELECTRIC CONDUCTORS	29
3.1 Topology optimization of conductor tracks in 2-D	30
3.1.1 Physics	30
3.1.2 Density-based topology optimization formulation	35
3.1.3 Study-cases and results	38
3.1.4 Discussion and conclusion	47
3.2 Winding design and 2.5-D topology optimization.	49
3.2.1 Winding design: a multi-coil interpolation scheme	49
3.2.2 2.5-D topology optimization for overlapping winding design	53
3.2.3 Discussion on the novel topology	57
3.2.4 Conclusion	59

Contents

3.3 Asymmetric winding design in 3-D topology optimization	60
3.3.1 Formulation	60
3.3.2 Design problem: a 3-D electromagnet manipulator	62
3.3.3 Conclusion	69
3.4 Fabricated topology-optimized coils.	70
3.5 Conclusion	72
4 ADDITIVELY MANUFACTURED COILS	73
4.1 Case study and first designs	74
4.1.1 Machine of interest: Coreless linear motor with permanent magnets . .	74
4.1.2 Coil topology and turn distributions	75
4.2 Harvesting the design freedom provided by additive manufacturing	77
4.2.1 Adaptation of conventional shapes to 3D-printing	77
4.2.2 Completed linear winding	78
4.2.3 Multi-functional winding	81
4.2.4 Conclusion	86
4.3 Experiments	88
4.3.1 Printing process	88
4.3.2 Post-processing of the coils	93
4.3.3 Electromagnetic properties	99
4.3.4 Thermal properties	103
4.3.5 Conclusion	105
4.4 Conclusion	106
5 SUMMARY AND PERSPECTIVES	107
5.1 Original contributions	108
5.2 Perspectives	109
5.3 List of publications	111
5.3.1 Patents	111
5.3.2 Journals	111
5.3.3 Conferences	112
A Weak form for electric conduction problem with current source	115
B Sizing and scaling of the diamond topology	117
Bibliography	121
Curriculum Vitae	

Notation

Acronyms (abbreviations)

AM	Additive Manufacturing
BC	Boundary Condition
DOFs	Degrees Of Freedom
EMF	Electromotive Force
EMI	Electromagnetic Interference
FEA	Finite Element Analysis
FFF	Filament Fused Fabrication
LC	Loading-Case
MIS	Material Interpolation Scheme
PA	Polyamide
PCB	Printed Circuit Board
PDE	Partial Differential Equation
PLA	Polylactic Acid
PM	Permanent Magnets
RAMP	Rational Approximation of Material Properties
ROI	Region Of Interest
SIMP	Solid Isotropic Material with Penalization
SLA	Stereolithography
SLS	Selective Laser Sintering
TO	Topology Optimization

Symbols

k_u	Back-EMF constant	V/(m/s)
σ	Electrical conductivity	S/m
I	Electric current	A
J_{crit}	Critical current density to not exceed	A/mm ²
J	Electric current density	A/mm ²
Ω	Design domain	—
U	Electric potential	V
\mathbf{E}	Electric field vector	V/m
θ	Electromagnetic potential (ampere turns product)	A
k_F	Force constant	N/A
h_{filt}	Filtering function	—
$h_{\text{Multi-Coil}}$	Multi-coil interpolation scheme	—
$h_{\text{SIMP:Multi-Coil}}$	Multi-coil interpolation and the SIMP scheme	—
h_{proj}	Projecting function	—
h_{RAMP}	RAMP scheme	—
$h_{\text{RAMP-2}}$	RAMP scheme combining two distributions	—
$h_{\alpha\text{-RAMP-2}}$	Weighted RAMP scheme combining two distributions	—
$h_{\alpha\text{-RAMP}}$	Weighted RAMP scheme	—
h_{SIMP}	SIMP scheme	—
C	Heat capacity	J/(kg · K)
\mathbf{q}	Heat flux vector	W/m ²
g	Inequality constraint	—
Ψ	Linkage flux through a coil	Wb
F	Lorentz force	N
Q	Joule Losses - Dissipated power	W
E_m	Magnetic energy	J
\mathbf{H}	Magnetic field vector	A/m
Φ	Magnetic flux vector	Wb
\mathbf{B}	Magnetic flux density vector	T
\mathbf{A}	Magnetic potential vector	T · m
k_m	Motor constant	N/√W
N_c	Number of coils	—
N	Number of turns constituting a coil	—
f	Objective function	—
r_{filt}	Filter radius	m
q	Penalty factor of the material interpolation scheme	—
β	Projection strength parameter	—
$\hat{\Psi}_0$	Magnitude of the fundamental component of the linkage flux	Wb
μ	Magnetic permeability	H/m

H_{PM}	Permanent magnet height	mm
W_{PM}	Magnetic pole pitch	mm
t_{PM}	Permanent magnet thickness	mm
w_{PM}	Permanent magnet width	mm
L_y^{PP}	Magnetic pole-pair length along y	mm
L_x^{PP}	Magnetic pole-pair length along x	mm
r	Relative change in resistance	–
R	Electrical resistance	m Ω
ε_R	Tolerance on phase resistance difference	–
ρ_0^{elec}	Reference electrical resistivity at 20°C	$\Omega \cdot m$
α	Resistivity temperature coefficient	s
ρ^{mass}	Mass density	g/cm ³
Δ_{coil}	Spatial shift between coils	mm
s	Sign indicating the flux direction	{+, -}
T	Temperature	K
T_{crit}	Critical temperature to not exceed	K
T_{stat}	Stationary temperature	s
k	Thermal conductivity	J/(kg · K)
t	Thickness of the considered tracks	m
τ	Time constant for a temperature rise	s
ρ	Distribution of artificial densities - design variables]0,1]
$\tilde{\rho}$	Distribution of filtered variables]0,1]
ρ^p	Distribution of penalized variables]0,1]
$\hat{\rho}$	Distribution of projected variables]0,1]
Vol^*	Volume fraction]0,1]
U^{RMS}	Voltage root mean square value	V
χ	Winding field]0,1]

1 MOTIVATION

Content

1.1 Introduction	2
1.2 Outlook	5
1.3 Context of the thesis.	6

1.1 Introduction

Electromagnetic devices



LECTROMAGNETIC devices are fundamental components of our modern society. The vast majority of power plants providing electricity to homes, businesses, and communities are built around electromagnetic generators. Whether considering hydroelectric plants such as dams, or wind and steam turbines, these devices are responsible for converting mechanical energy into electricity. Even future power plant concepts based on nuclear fusion energy, such as tokamaks, use electromagnetic coils to confine the burning plasma. Further down the energy transmission process, electromagnetic transformers are used at the output of power plants to increase the voltage to the high levels required to transmit electricity efficiently over large distances.

Other electromagnetic devices such as inductors are well spread in electronics. The general public may know more about electric motors largely present in the industry and our everyday lives. Many types of vehicles are now powered by electric motors, like electric cars, buses, trains, and even boats. They offer several benefits over traditional internal combustion engines, such as more energy efficiency and better controllability. This also makes them a more environmentally friendly choice for transportation, as they do not contribute to air pollution or greenhouse gas emissions. Electric motors are widely adopted in robotics too. They enabled the electrification and automation of our production lines with industrial robots and automated tools, which permitted the increase of production pace and quality. This drove down the cost of many products and consumables, providing more purchasing power to people. The interesting features of electric motors, such as lightweight and high power density, also made them key components in mobile robots and drones for applications such as monitoring or search and rescue. In the healthcare field, electromagnetic devices have also enabled important advances. One could cite Magnetic Resonance Imaging (MRI) which gives a better understanding of the human body for medicine, or proton therapy, which eliminates cancerous tumors. They both rely on powerful electromagnets to excite the spin polarization of certain nuclei or focus/deviate the beam of charged particles, respectively.

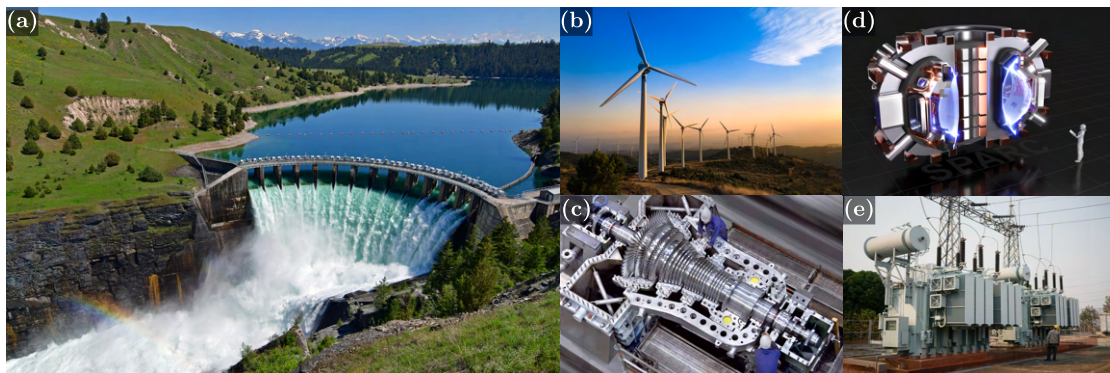


Figure 1.1: Power plants and electromagnetic devices: (a) hydroelectric [1]; (b) wind power [2]; (c) steam turbine [3]; (d) SPARC tokamak [4]; (e) transformers for high voltage in transmission lines [5].

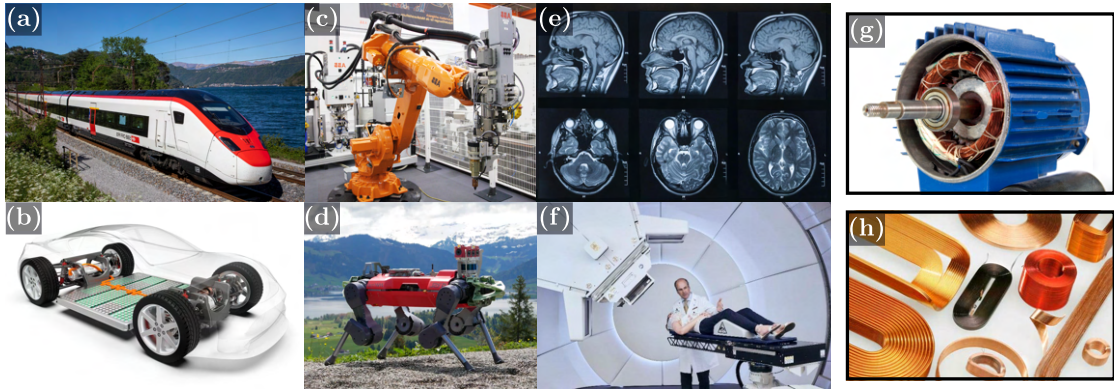


Figure 1.2: Electromagnetic devices in society: transport industry: (a) trains [6]; (b) electric cars [7]; (c) industrial [8] and (d) mobile [9] robots; (e) magnetic resonance imaging (MRI) [10]; (f) proton therapy [11]. Key electromagnetic devices: (g) the electric motor [12]; and more specifically, (h) the electromagnetic coil [13].

Finally, electromagnetic devices are staples in communications and optics by working with electromagnetic waves such as radio or light. This specific range of applications works at really high frequencies and often relies on significantly different hardware. The work presented in this manuscript does not consider such phenomena, focusing on devices working at lower operating frequencies or static operation.

There is a constant need for better electromagnetic devices as society's demands and technological capabilities continue to evolve. This need is driven by the desire for more efficient and reliable technology in a variety of industries, as well as the urgency for more sustainable and environmentally friendly solutions. High-performances are defined by market demands and application-specific requirements but often involve devices with larger output power, like larger forces, and lower losses for better efficiency. How does this thesis aim at contributing to such a goal? By focusing on the central component of most electromagnetic devices: the electromagnetic *coil*. It plays a key role in the generation and control of electromagnetic fields. For example, in an electric motor, coils of wire are used to create a rotating magnetic field, which drives the movement of the motor. In a transformer, coils transfer electrical energy from one circuit to another through electromagnetic induction. Overall, their proper design and implementation are crucial for the effective functioning of electromagnetic devices. This thesis presents novel design and fabrication methods for electromagnetic coils enabling a new generation of electromagnetic devices with improved performance.

Conventional coils

The basic physical phenomenon occurring in a coil is the generation of a magnetic field associated with a flowing electric current. Any metal can sustain an electric current, but the ones with high electric conductivity, such as copper, silver, or aluminum, are preferred due to their better ability to drive charged particles. The layout of these conductors in space affects the generated magnetic field distribution. Its concentration can be achieved by looping the conductors on themselves. If repeated multiple times, these connected loops (or turns) form a

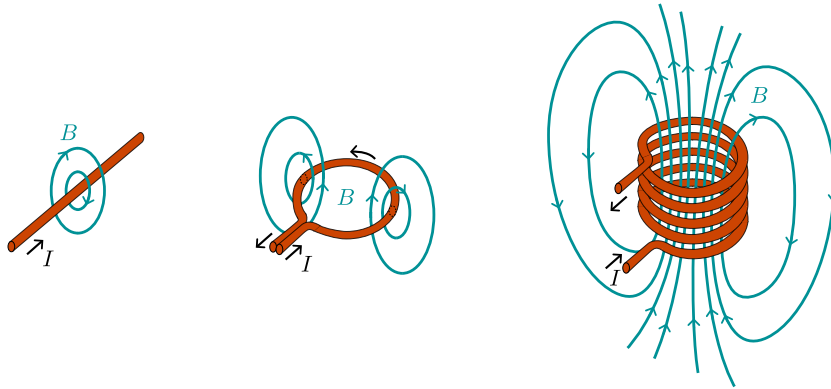


Figure 1.3: Basic electric conductors and resulting magnetic fields: wire, loop, solenoid.

solenoid (also known as a *coil*¹) which further concentrates the field at its center. Such basic conductor shapes are massively used in electromagnetic actuators. When multiple coils are considered, they can be referred to as a *winding*. Some works, like this one, use this term only when considering coils powered with different electric currents.

Conventionally, a coil is made of a conducting wire wound in a solenoid or other shapes. This form is simple to model and straightforward to manufacture and integrate into a device. Its design is often restricted to a few parameters, such as the coil span, the wire diameter, or the number of turns. As the geometry is fairly simple, analytical equations can be determined to evaluate the magnetic field distribution so as to determine the ideal coil layout.

How to improve upon a robust technology?

The design of electromagnetic coil is a mature process refined over years of research and industrial development. One could wonder how to improve on such a robust technology. Let us first identify the limitations of conventional coils. The fact that they are constituted of a wound wire is the first limitation because it constrains the possible geometries that it can take. The constant cross-section, often rounded, prevents a great packing of the different turns, which degrades the achievable power density and losses. The single path described by the wire limits the feasible magnetic field distributions and inherently the possible electromagnetic forces. The winding process of the wire may also be a burdensome operation. It requires either labor-intensive manual work or inflexible, custom-designed automated equipment. Additionally, electromagnetic devices generally consist of multiple components that must work together in order to function effectively. For example, the electromagnetic coils could need support to assure mechanical stability. They might also need suitable thermal management to prevent them from overheating. However, in practice, these functionalities are accomplished by different subsystems, often designed separately. This degrades the overall synergy of the device from a system engineering perspective. For example, the total footprint might be degraded due to assembly with multiple components, or the specifications of the different subsystems might not be fully adapted to each other. It would be better to consider the whole

¹The series of circled-shape conductors led to the designation: *coil*. Nowadays, more geometries exist, but the name persists.

system's different physics and intertwined functionalities at once while designing the coil.

The strategy chosen in this thesis is to harvest the design flexibility provided by AM technologies to fabricate novel electromagnetic coils and alleviate the aforementioned limitations to achieve better performance. Additive manufacturing, also known as 3D printing, is a process in which a three-dimensional object is created by depositing material layer by layer. This technology has the potential to revolutionize the way electromagnetic devices are designed and produced. One advantage of 3D printing is the ability to quickly and easily prototype and test different designs. It can significantly reduce the time and cost required to bring a new design to market. In addition, AM allows for producing custom and complex geometries that may not be possible using traditional manufacturing methods. For example, a 3D-printed electromagnetic coil could have a non-constant cross-section and be constituted of multiple paths that could freely split or merge. Furthermore, additive manufacturing provides additional design freedom to integrate multiple system functionalities into a single part. For example, the thermal management of the device can be integrated into the coil itself to improve efficiency and achieve larger maximal power. Finally, 3D printing can also reduce material waste, as excess material can be recycled and reused in the manufacturing process. It can lead to cost savings and a more sustainable production.



Figure 1.4: Additive manufacturing: (a) illustration of selective laser melting printing process [14], (b) example of parts printed in copper [15], and (c) multi-functional printed part combining fluid channels with heat exchanger [16].

In this thesis, we propose a computational design method to automatically design 3D printed electromagnetic coils. This choice is motivated by the fact that the great design flexibility provided by additive manufacturing technologies results in a large solution space that would be only partially explored with conventional design methods. Thus, in order to fully harvest the available room for improvement, it is proposed to rely on a dedicated tool combining numerical methods and optimization. Furthermore, this enables automation of the design step, resulting in a versatile tool that can be applied to many different problems without the need of repeating the development process. This is expected to save time and money for the designers of electromagnetic devices in the future.

1.2 Outlook

This thesis is split into two main parts: the description of the developed computational design methods and the demonstration of additively manufactured coils. It is preceded by a common state-of-the-art and followed by a conclusion.

Chapter 1. MOTIVATION

Chapter 2: STATE OF THE ART

This chapter puts in perspective the work presented here to the existing ones already proposed by other scientists and industries. It first defines computational design, then presents the specific topology optimization method. Different examples of computational design for electric conductors are then discussed and concluded by identifying the possible improvements and needs in the field. Then, the state-of-the-art on advanced manufacturing of electromagnetic coils is covered. The different types of winding are first defined, followed by the presentation of coils fabricated with two different manufacturing methods: printed circuit board technology and additive manufacturing technology. Finally, the room for improvement is discussed.

Chapter 3: COMPUTATIONAL DESIGN OF ELECTRIC CONDUCTORS

Firstly, the design of simple electric conductors in a 2-D space is studied. The physics and optimization problems associated with the method are presented. They are applied to different study cases and discussed, validating the possibility of designing a coil in 2-D. Secondly, the topology optimization method is extended to winding design, considering the packing of multiple coils without *a-priori* knowledge of their position or shape. Symmetric winding made of identical coils is first considered. A 2.5-D approach is formulated to enable the design of overlapping winding. Thirdly, the possibility of designing asymmetric winding with different coils is studied and demonstrated through a 3-D topology optimization problem. Finally, the fabrication of topology-optimized coils is discussed, introducing the next chapter.

Chapter 4: ADDITIVELY MANUFACTURED ELECTROMAGNETIC COILS

This chapter demonstrates the feasibility of additively manufacturing electromagnetic coils. First, the case study and the different coil topologies are presented. Multiple additional design features are proposed to tackle the challenges related to Joule losses and heat dissipation by harvesting the design freedom provided by AM technologies. The first one is the possibility of having tracks with evolving cross-sections, and the second is the principle of *completed* linear winding reducing the losses at fixed input current. The third one is the concept of a multi-functional coil with integrated heat sinks for better thermal management. Finally, experiments are presented by covering the fabrication process and different tests of the manufactured winding.

Chapter 5: CONCLUSION

This chapter concludes the manuscript by summarizing the different contributions of this thesis to the scientific literature. The opened perspectives in the field of computational design as well as AM of electromagnetic coils are also presented. Finally, the scientific papers and patents realized during this thesis are listed.

1.3 Context of the thesis

This thesis has been funded by an Innosuisse (Swiss innovation agency) project: 32925.1 IP-ENG and performed in collaboration with a Swiss industrial partner.

2 STATE-OF-THE-ART

Content

2.1 Computational design of electric conductors	8
2.1.1 Computational design	8
2.1.2 Topology optimization	9
2.1.3 Application to electric conductors	16
2.1.4 Room for improvement	20
2.2 Advanced manufacturing of electromagnetic coils	22
2.2.1 Winding types	22
2.2.2 Printed circuit board technology	23
2.2.3 Additive manufacturing technology	24
2.2.4 Room for improvement	27

This part presents the state-of-the-art on computational design in general and applied to electric conductors. Additionally, the state-of-the-art of advanced fabrication techniques for electromagnetic coils is also presented. The room for improvement is identified and discussed for both fields.

2.1 Computational design of electric conductors



ANY research work requires presenting state-of-the-art addressing the studied field. Here, computational design is first defined. Then, a specific computational design method: the topology optimization, is described more deeply as it will be the main one implemented in this work. A dedicated part covers the computational design of electric conductors to identify the missing elements. Finally, the contributions of this thesis to the state-of-the-art mentioned above are listed.

2.1.1 Computational design

In engineering, computational design is the process of determining the design of a device relying on computational resources. This can be achieved by formulating the design problem as an optimization one. It investigates the best set of parameters describing the geometry of the piece. These parameters are used as control variables to improve an objective function evaluating the performance of the design. This function is dependent on the physical properties of the geometry to optimize. They can be computed analytically or numerically. An optimization solver (a.k.a an optimizer) can then be used to update the control variables in order to improve (minimize or maximize) the objective. The strategy implemented by this solver depends on its nature and the type of optimization desired (local search or global search). It may require information on the sensitivity of the problem, corresponding to the gradient of the objective function with respect to the control variables.

The different natures of parameters describing the geometry create three prominent families of computational design: dimensional/size optimization, shape optimization, and topology optimization. The differences in the chosen parameters also impact the possible topologies/geometries (contours, holes). The first refers to the most common type, where a few dimensions describing the geometry are used to parametrize the design. Fig. 2.1 shows an example with the diameter of a circle as the controlling parameter, but it could be the length, width, or thickness of a plate, etc. This method uses only a few control variables to construct the geometry but requires *a-priori* knowledge of the desired geometry. The physical properties can be evaluated analytically or with numerical methods such as FEA. It has been extensively used in many fields due to its ease of implementation, and lower computational cost [18, 19, 20]. Shape optimization, on the other hand, enables the description of a geometry by an implicit definition of its boundaries. Such a method enables the boundary(ies) to evolve during the optimization to improve the properties of the design. It requires less *a-priori*

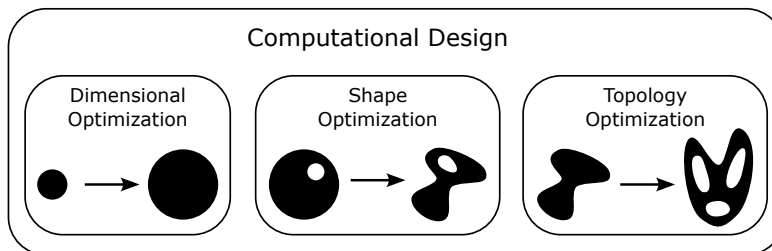


Figure 2.1: Main computational design methods. Figure modified from [17, ch. 1.].

knowledge of the desired geometry than before. However, this still restrains the possible solutions to a set with a fixed number of contours (external boundaries and holes). It has a higher computational cost than the previous method as more control variables are used to describe the shape. Nevertheless, it has been greatly investigated in structural mechanics [21, 22], and also extended to various physics like electromagnetism [23]. Finally, topology optimization is the most versatile method as it does not require *a-priori* knowledge of the desired geometry and can result in any form. As further described in Section 2.1.2, the topology is described implicitly using some parameters. The most common representations are the *density-based* and the *level-set* methods. The first describes the geometry with a distribution of material inside a discretized space. The second one is intrinsically a shape-optimization method. However, it artificially achieves topology optimization-like results by choosing an initial shape with many contours/holes allowed to merge/disappear while optimizing. This raises an important observation on computational design methods. Despite having numerous definitions and implementations that can be categorized straightforwardly, some hybrid or unconventional methods can not be classified or restricted to one family.

In this work, topology optimization is selected because it is more suited to establish a robust and versatile computational design framework for designing coils in electromagnetic actuators. Heuristic optimization is assumed here, but there is a growing interest from the community for stochastic optimization, especially when modeling uncertainty [24, 25].

2.1.2 Topology optimization

This section presents the TO method with two possible implementations in more detail. Numerous reviews exist in the literature [26, 27, 28], but a glimpse is reported here for clarity. Electromagnetic applications are described here as more relevant to the scope of this manuscript and possibly closer to the reader's interest. However, one should remember that these methods were initially developed for structural mechanics and that most of the work performed in topology optimization is dedicated to this field.

2.1.2.a General optimization

First, presenting a general formulation of an optimization problem is important. The optimized value should be a scalar, defined as the *objective function* f . This value is minimized (or maximized) by updating a set of *control variables* represented in a vector \mathbf{x} , which should satisfy some inequality constraints, also represented in a vector \mathbf{g} . The control variables are bounded by their lower $\underline{\mathbf{x}}$ and upper $\overline{\mathbf{x}}$ limits. The optimization problem is formulated as follows:

$$\begin{aligned}
 \text{Find:} & \quad \mathbf{x} \\
 \text{Minimize:} & \quad f \\
 \text{Subject to:} & \quad \mathbf{g}(\mathbf{x}) \leq \mathbf{0} \\
 & \quad \underline{\mathbf{x}} \leq \mathbf{x} \\
 & \quad \mathbf{x} \leq \overline{\mathbf{x}}.
 \end{aligned} \tag{2.1}$$

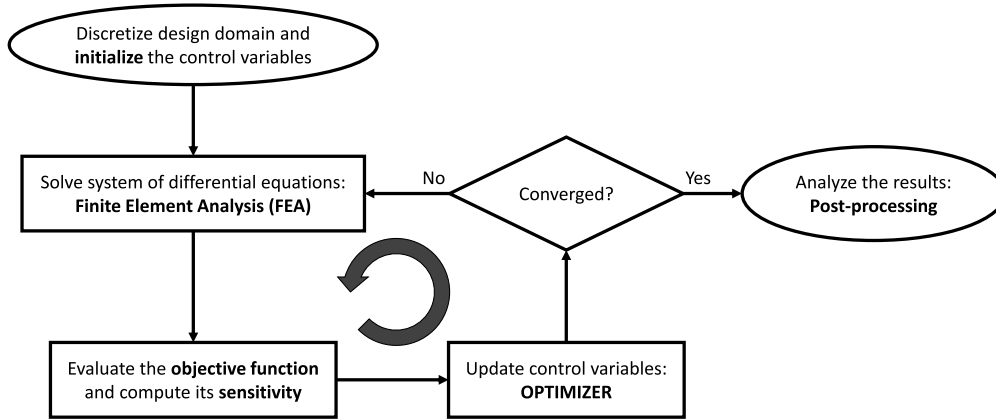


Figure 2.2: General topology optimization flowchart (modified from [17, ch. 4.1]).

The element that updates the control variables is called an *optimizer*. Its implementation and the nature of control variables characterize different families of optimization problems: *gradient*- and *non-gradient*-based optimization. This results in local-search and global-search optimizers, respectively. Local-search methods lead to the global optimum of the problem only if its formulation is convex [29, ch. 1.4.1]. Otherwise, they will end up with local solutions dependent on the initial guess of control variables. Formulating the optimization problem in a convex one is encouraged whenever possible. It assures finding the best solution and fast computation. Unfortunately, most real-world problems are non-convex [30, ch. 1.3.3]. Only gradient-based methods are considered in this work because they lead to faster computation and better scale to large dimensional problems [31]. However, some works still investigate global search methods [32]. Readers interested in the differences between *local*- and *global*-search TO are invited to read the following work [31]. As their name suggests, gradient-based methods require the gradient of the objective function with respect to the control variables: $\frac{df}{dx}$. It is also referred to as the *sensitivity* of the optimization problem. Its computation is further discussed in the following subsection. Once the objective function and its sensitivity have been computed, the optimizer can update the control variables. Examples of gradient-based solvers are the *Optimality Criterion (OC)* [33], the *Method of Moving Asymptotes (MMA)* [34], which is popular in many topology optimization problems, and the Interior Point Methods (IPOPT) [35]. A more extensive list can be found in [36]. A general flowchart of topology optimization is shown in Fig. 2.2.

2.1.2.b Finite element analysis

The physical properties of the piece being designed are crucial to evaluating its performance. These properties can be analytically derived when simple geometries are considered and when the desired information is limited to points or lines inside the physical space. Numerical tools are necessary when more complicated geometries are considered (such as in TO), and the physical properties are needed everywhere in space. A popular method is the FEA, which requires a mesh discretizing the physical space into finite elements. As the geometries of the different parts (to be designed) and/or the environment evolve during the optimization process, either this mesh needs to be updated and refined to match the geometries at every

iteration, or the evolving geometries are projected onto a fixed mesh. In this work, we will focus on the latter, but readers interested in refinement techniques are invited to read the following reference [37].

An FEA solves PDE. The weak form of such equations [38] can be discretized and solved onto the finite elements. Their unknowns are finite \mathbf{U} (also called *state-variables*) but can be evaluated everywhere in space by interpolating the discrete values with dedicated functions. The discrete nature of this method permits the formulation of the differential equation as matrix equality, which can be directly solved when linear phenomena are studied:

$$\mathbf{K}(\mathbf{x}) \cdot \mathbf{U} = \mathbf{L}, \quad (2.2)$$

with \mathbf{U} the vector of unknown (also called *state-variables*), \mathbf{K} the *system* (or *stiffness*) matrix depending on the geometry and material properties, and \mathbf{L} the *source* (also called *load*) vector. The system matrix is symmetric and often sparse. Depending on the physics solved, the source term of the equation may also depend on the state variable ($\mathbf{L} = \mathbf{L}(\mathbf{U})$), resulting in a non-linear PDE requiring specific iterative solvers that implement methods such as Newton-Raphson. In this work, this is not considered for simplicity. Further information on FEA and its implementation in electromagnetism can be found in [38]. As shown later, the source term can also depend on the control variables, which modifies the equations to solve but does not change the logic/development behind it.

2.1.2.c Adjoint Variable Method

Gradient-based optimization requires the sensitivity of the problem corresponding to the gradient of the objective function with respect to the control variables. The adjoint variable method is often implemented for TO as other methods, such as finite differences, do not scale well with the large number of control variables [39]. Its implementation is described here.

The adjoint variable method is based on constructing the augmented objective function (i.e., the Lagrangian) \mathcal{L} , which introduces the array of *adjoint-variables* Λ .

$$\mathcal{L} = f + \Lambda^\top (\mathbf{K}(\mathbf{x}) \cdot \mathbf{U} - \mathbf{L}). \quad (2.3)$$

Following Karush–Kuhn–Tucker theorem [29, ch. 5.5.3], the objective function and the augmented one are equal and have the same sensitivity for a set of optimal parameters. We can choose the values of Λ arbitrarily and keep the augmented objective function equal to the former one. The theory of the adjoint variable method goes beyond this introduction but is kept simple here for clarity. Interested readers are invited to investigate the following works for more details: [40, 41, 22, 42].

The sensitivity can be derived using the chain rule:

$$\frac{df}{dx} = \frac{d\mathcal{L}}{dx} = \frac{\partial f}{\partial \mathbf{U}} \frac{\partial \mathbf{U}}{\partial x} + \Lambda^\top \left(\frac{\partial \mathbf{K}(\mathbf{x})}{\partial x} \mathbf{U} + \mathbf{K}(\mathbf{x}) \frac{\partial \mathbf{U}}{\partial x} \right) \quad (2.4)$$

$$= \left(\frac{\partial f}{\partial \mathbf{U}} + \Lambda^\top \cdot \mathbf{K}(\mathbf{x}) \right) \frac{\partial \mathbf{U}}{\partial x} + \Lambda^\top \left(\frac{\partial \mathbf{K}(\mathbf{x})}{\partial x} \mathbf{U} \right) \quad (2.5)$$

$$= \Lambda^\top \left(\frac{\partial \mathbf{K}(\mathbf{x})}{\partial x} \mathbf{U} \right). \quad (2.6)$$

Equation (2.6) is satisfied only for a specific set of adjoint variables. They should satisfy the adjoint variable equation:

$$\frac{\partial f}{\partial \mathbf{U}} + \Lambda^\top \cdot \mathbf{K}(\mathbf{x}) = 0, \quad (2.7)$$

which can be reformulated to a single matrix equation similar to the form of the one describing the FEA in (2.2):

$$\mathbf{K}(\mathbf{x}) \cdot \Lambda = - \frac{\partial \mathcal{L}}{\partial \mathbf{U}}. \quad (2.8)$$

This shows the advantage of the adjoint variable method when the number of design variables is vast compared to the number of functionals to derive. Only one additional numerical analysis (matrix equation) has to be solved to compute the sensitivity, whatever the number of control variables considered. It permits a tremendous gain in computational time compared to other derivation methods [39], and is one of the features that made popular gradient-based topology optimization. Nowadays, this step is often automated and performed "behind the scenes" of topology optimization frameworks or finite element software thanks to automatic derivation tools [43, 44]. Nevertheless, it is essential to understand this concept as being at the core of many topology optimization methods. This also shows the need for differentiability for every possible intermediate step composing the objective function.

2.1.2.d Control variables in topology optimization

Among the numerous possibilities to do TO, only the two most known methods are described in this section: the *density-based* approach and the *level-set* method. These methods mainly differ in the nature of their control variables but still have some subtleties and different features (additional constraints and intermediate steps) not covered in this introduction. Interested readers are invited to browse the reviews on the previously mentioned subject or the dedicated books [30, 17, 45].

Level-set method

This approach implicitly defines the material distribution through boundaries that can evolve during optimization. These contours of the topology are obtained when an evolving surface (called the level-set function) intersects a fixed plane as shown in Fig. 2.3. The shape is evolving in time with a normal velocity, so the evolution of the level-set function is governed by a Hamilton-Jacobi equation [46]. This method is similar to Shape Optimization if not coupled with other techniques (such as topology derivative). No holes can be generated with such a function; they can only be merged or removed. To tackle this issue, the initial design can be composed of numerous holes to have them evolve (or disappear) to find an optimized structure

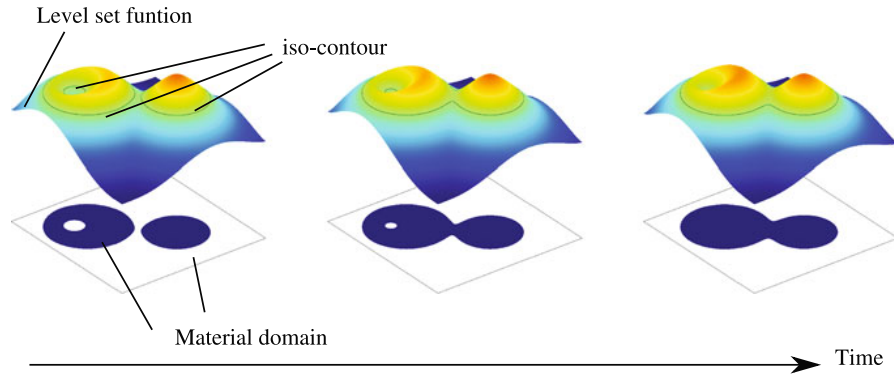


Figure 2.3: Level-set function evolution with time [17, ch.4.1.1].

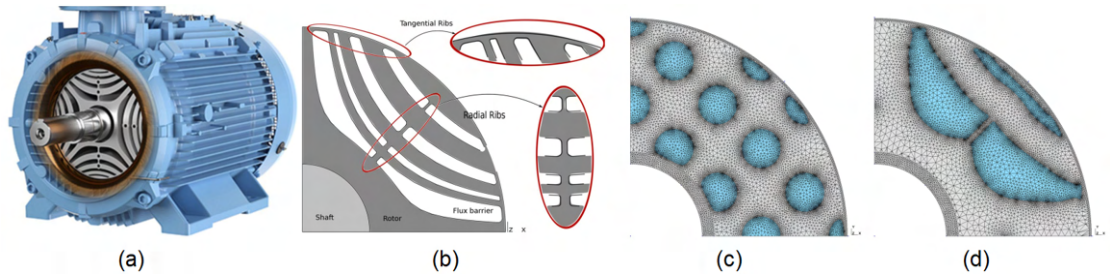


Figure 2.4: Topology optimization based on the level-set method applied to the design of the rotor of a synchronous reluctance motor: (a) machine of interest from ABB motors, (b) representation of the flux barriers and ribs composing the rotor, (c) initialization of the level-set-function enabling hole merging and thus topology optimization, and (d) topology resulting from joint electro-mechanical optimization [47].

without being too dependent on the initial conditions. Some regularization techniques are used with this approach to stabilize the numerical solution or control the evolution of the level set function. One example is to add a diffusive and reactive term to the convective one in the Hamilton-Jacobi equation. The level-set method can achieve *gray-scale free* designs resulting in a crisp definition of the structure being designed, as opposed to the popular *density-based* method (presented next). However, its strong need for regulation techniques for proper convergence makes it sometimes complicated to implement. This partially explains why most research in the field implements the most straightforward *density-based* approach.

Nevertheless, this method has been implemented in multiple applications such as structural [48], and thermal [49]. Naturally, it has also been applied to electromagnetic applications such as the design of an iron core inside a simple magnetic actuator [50], or the design of the ribs constituting the rotor of a synchronous reluctance motor as shown in Fig. 2.4.

Density-based approach

This approach describes the geometry as a distribution of artificial densities of material in space. Its basic implementation can be seen as a scalar field varying continuously between 0 no-material and 1 material. The continuous nature of the control variables is necessary to rely

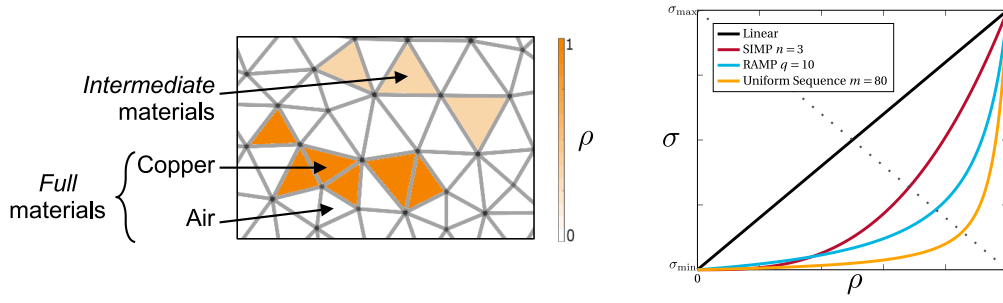


Figure 2.5: Density-based topology optimization principle illustrated for copper distribution, and examples of Material Interpolation Schemes (MIS).

on a fast gradient-based optimizer. However, it creates *intermediate*-materials (sometimes referred to as "gray-scale" materials) in between the *full*-materials describing the entire presence or absence of material as shown in Fig. 2.5. These intermediate materials do not have a physical meaning but are used as a mathematical tool to compute gradients. Ideally, the final topology should be free of these intermediate materials to describe the geometry adequately. The intuitive nature and straightforward implementation have made it the most popular topology optimization strategy, which will be implemented in this work.

Additional processing of the distribution of artificial densities can be performed before being mapped to actual material properties. It enables the enforcement of different behaviors or features within the designed topology. This is important as multiple intermediate steps will be proposed in this manuscript for different purposes. Nevertheless, a common step is *filtering* [51, 52], which imposes a minimal length scale inside the topology being designed (preventing mesh dependency and checkerboard patterns). It can be followed by a *projection*-step [53], which results in a crisper definition (full materials) of the topology as the previous filtering step blurs the boundaries of the topology (creating undesired intermediate materials).

Once intermediate steps have fully processed the density distribution, the resulting distribution can be mapped to material properties. This is done through a MISs. The most well-known is the SIMP [30, eq. 1.4]. It is important to clarify that the term SIMP only refers to a possible implementation of the MIS and not the complete *density-based* topology optimization method as sometimes done in the literature. Indeed, there is no limitation in the functions that can be used for the MIS. Different known schemes are the RAMP [26, eq. 5], and the uniform sequence [54, eq. 5]. The main goal of these schemes is to "penalize" intermediate materials so as to make them less attractive to the optimizer (often coupled with a volume limitation) and favor topologies made of full materials. It is achieved through different penalty factors that can also be continuously increased so as to prevent a too-fast convergence to local optimums [55].

The density-based topology optimization method has been implemented for electromagnetic applications. An example is the design of the iron yoke constituting a magnetic resonator [56]. As shown in Fig. 2.6, multiple topologies were obtained for different exciting frequencies. This is a good application of topology optimization as the same implementation enabled the design of multiple geometries that a human designer does not easily determine.

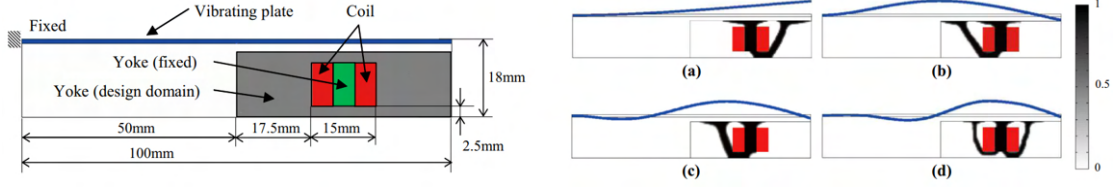


Figure 2.6: Density-based topology optimization of the iron yoke of a magnetic resonator with (left) design problem and (right) resulting topologies for different exciting current frequencies (a) 88.6Hz, (b) 554.9Hz, (c) 1552.9Hz, and (d) 3040.7Hz [56].

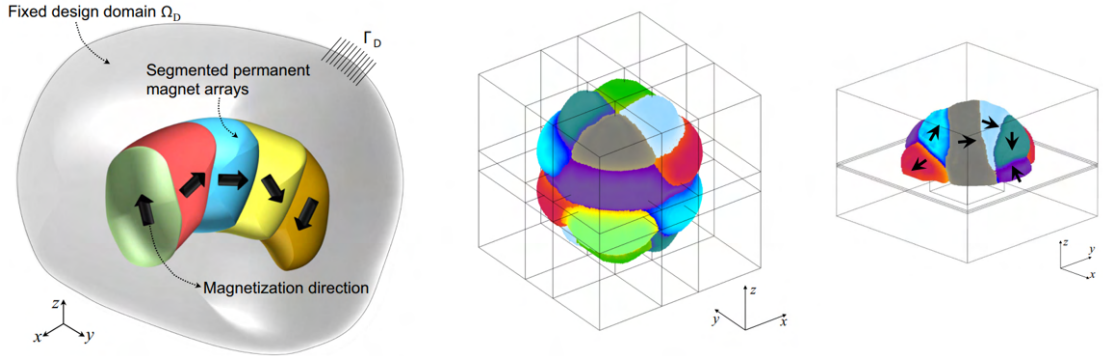


Figure 2.7: Density-based topology optimization in 3D of permanent magnet (PM) arrangement with magnetization direction. (Left) Schematic representing the design problem, (middle) resulting topology for 3D-dipole PM with eight different magnetization directions, and (right) resulting topology for 3D-PM array maximizing the magnetic force along the z-direction [57].

Another work investigated the design of iron pieces, and permanent magnets with different magnetization orientations [58]. It highlights the possibility of doing multi-material topology optimization. The maturity of the density-based approach also enabled the implementation of a 3D topology optimization framework investigating the ideal distribution of permanent magnets in space, as well as their magnetization directions [57] as shown in Fig. 2.7. One should remember that there is a significant increase in computational burden when moving from 2D problems to 3D ones. Nevertheless, the relatively fast computation enabled by gradient-based optimization and the improvement of computational resources (supercomputers [59], parallel computing [60]) still permit the implementation of such work.

The density-based approach is chosen for this research because robustness and efficiency are desired while preventing a too strong dependency on the initial guess. Furthermore, it has been and still is subject to a strong research interest from the community, which eases the implementation of newly developed features.

2.1.3 Application to electric conductors

Several works have already investigated the computational design of electric conductors. This reinforces the interest and the need to develop a robust and versatile method to design such devices better. This section is not restricted to topology optimization methods to properly establish the state-of-the-art. To the author's knowledge, only 2D designs have been performed by the community. It means that only 2D projections of the coils to be designed are covered. This results in either the design of the cross-section of the coil or the design of the tracks constituting the coil.

Dimensional optimization

Dimensional optimization is the most known and investigated method to perform computational design. It has been massively implemented for the design of winding tracks too [61, 62, 18]. A significant limitation shown in Fig. 2.8 is that the resulting geometry strongly depends on the initial guess and how the shape is parameterized. When assumed to be composed of four segments, the possible geometries of the coil are limited to such description, resulting in a simpler shape than when more are considered. This results in a difference of more than 17% in the performance criterion.

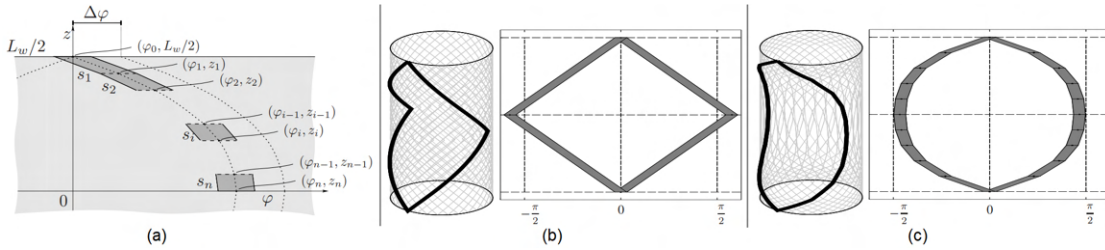


Figure 2.8: Dimensional optimization of flex-PCB winding for slotless permanent magnet machines [61]. (a) Design problem and control variables defining the mean path of the tracks and their width, (b) resulting coil using assuming 4 segments, and (c) resulting coil using 20 segments.

Shape optimization

Shape optimization has been applied to the design of the cross-section of a coil, such as an example of a solenoid made of high-temperature superconductors [63]. It has also been implemented to design tracks of electric conductors [64] aiming to minimize the Joule losses while being subject to a voltage source. It is equivalent to minimizing the resistance of the designed track. An example is shown in Fig. 2.9. As already mentioned, the shape optimization method is interesting but is limited to the initial guess on the design. The solution space is quite limited if no hole nucleation or merging is considered (corresponding to topology optimization methods).

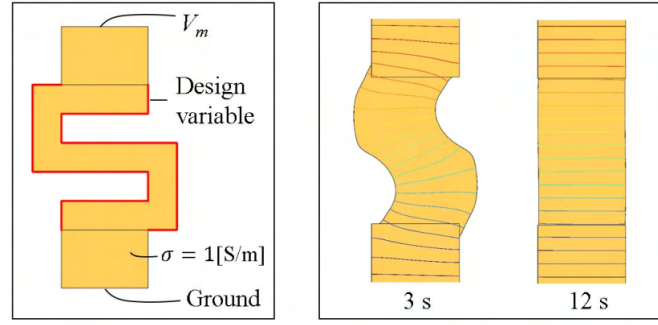


Figure 2.9: Shape optimization of conductor tracks subject to a voltage source aiming at minimizing losses [64]. (Left) Design problem and initial shape, (right) shape evolution.

Topology optimization of conductor cross-section

The first implementations of the topology optimization method to design electric conductors were limited to the design of its cross-section. It assumes a current normal to the design plane. An example is [65] studying the ideal layout of the cross-section of a coil achieving a desired magnetic field at specific measuring points as shown in Fig. 2.10.a. Another interesting example investigates the distribution of the cross-section of inductors and current direction (inward or outward) for electromagnetic casting [66] as shown in Fig. 2.10.b.

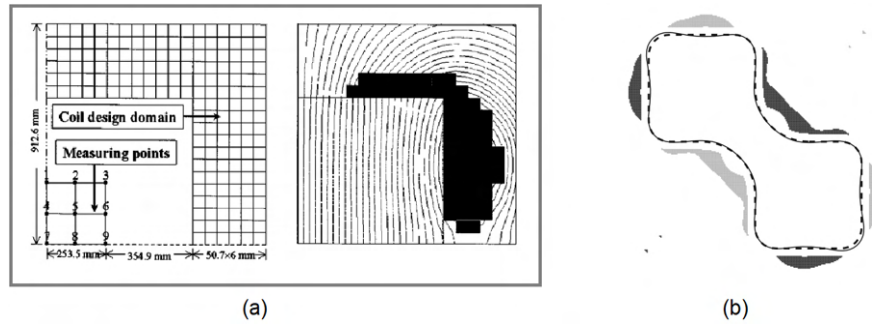


Figure 2.10: Design of conductor cross-section: (a) Design problem and resulting topology [65]; (b) Inductor design for electromagnetic casting - Black areas: positive inductors, gray areas: negative inductors, dashed line: target shape, thin solid line: equilibrium shape [66].

Additionally, researchers have explored multi-material topology optimization such as [67, 68] for the design of iron and coils inside the cross-section of a switched reluctance motor. Permanent magnet designs have also been added to such a framework with [69, 70], who designed electromagnetic plunger and magnetostrictive sensors, respectively.

Topology optimization of conductor tracks

Topology optimization has also been applied to the design of conductor tracks. The first example uses the density-based approach to investigate the ideal conductor maximizing the

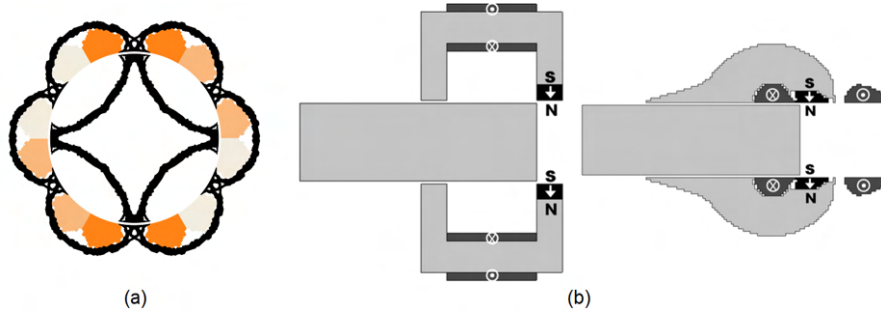


Figure 2.11: Multi-Material topology optimization: (a) Design of reluctance motor investigating the distribution of iron (black) inside the stator and rotor, as well as the coil cross-section distributions (oranges) [67]; (b) design of electromagnetic plunger investigating the ideal distribution of iron (light gray), permanent magnets (black), and coils cross-section (dark gray) [69].

Lorentz force [71]. As shown in Fig. 2.12, this force results from the interaction of the electric current flowing through the conductor and an external magnetic field imposed by permanent magnets. A simple electric conduction FEA with a voltage source (Dirichlet boundary conditions) is studied. There is no study on the magnetic field generated by the coil being designed, only the computation of the Lorentz force. Additionally, a single coil design is achieved by carefully limiting the design space and harvesting symmetry. Packing of multiple coils forming a winding is not treated. A similar work investigates novel gradient coil designs for a Magnetic Resonance Imaging (MRI) device. This application requires the computation of the magnetic field generated by the designed coil inside a ROI. The Biot-Savart formulation is used here. Such formulation is computationally attractive only if the magnetic flux magnitude is desired in a few points of the design problem and not everywhere. In such a case, Ampere's law should be solved instead, but it still needs to be done in the literature. Such a formulation is also restricted to problems with uniform magnetic properties. Here everything is performed in air, without any ferromagnetic materials. Regarding its boundary conditions, this work imposes a voltage drop on the design domain. However, it provides the magnitude of this voltage source

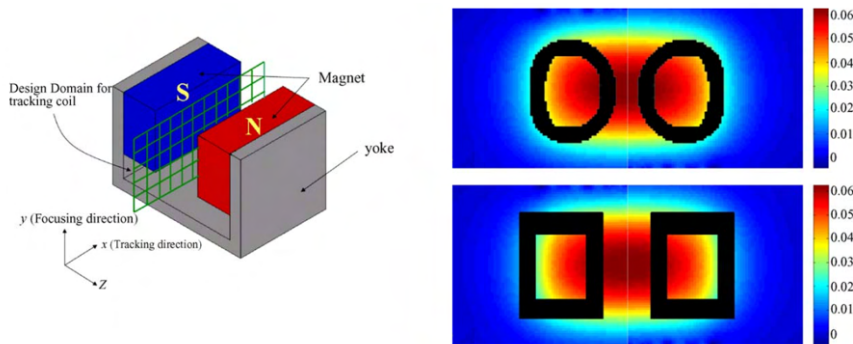


Figure 2.12: Conductor track design based on Lorentz force maximization [71]. (left) Design problem; (right) the resulting optimized coils against the magnetic density distribution (colormap) above the rectangular reference coils.

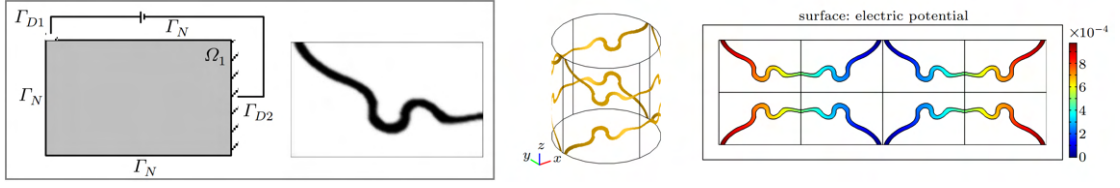


Figure 2.13: Gradient coils design with the density-based method and voltage source [72]. (Left) Design domain with a voltage source and topology resulting from optimization, (middle) reconstructed 3D coils, and (right) electric potential distribution.

as an additional control variable. This permits a partial decoupling between the material distribution and the magnitude of the current flowing through it. However, this degrades the computational time due to the additional control variable. It also degrades the optimization behavior because of the different natures and scales of the control variables.

A recent work published during the progress of this thesis uses the level-set method to investigate the ideal layout of conductor tracks for printed circuit boards [73]. They are not explicitly coils but fundamentally similar, as shown in Section 1.1. A simple physic (electric conduction) and a more advanced one (electromagnetic field propagation for antennas) are considered. A specific constraint has been formulated to prevent or enforce specific connections between electrical components. However, it requires *a-priori* knowledge of the number of loops/connections that will constitute the circuit. Fig. 2.14.a shows an example applied to an EMI filter with the topology resulting from the optimization for maximal power gain. The same team extended this formulation to the layout of conductors in order to cancel parasitic inductance in circuit boards (Fig. 2.14.b). This work is interesting but lacks some features for describing electromagnetic coils for actuators. For example, the packing of multiple conductor tracks to form windings must be addressed. The explicit description of the number of loops/tracks prevents possible additional splitting or merging of the tracks. Also, the possible geometries are limited due to the 2-D representation constraining the topologies to a single plane.

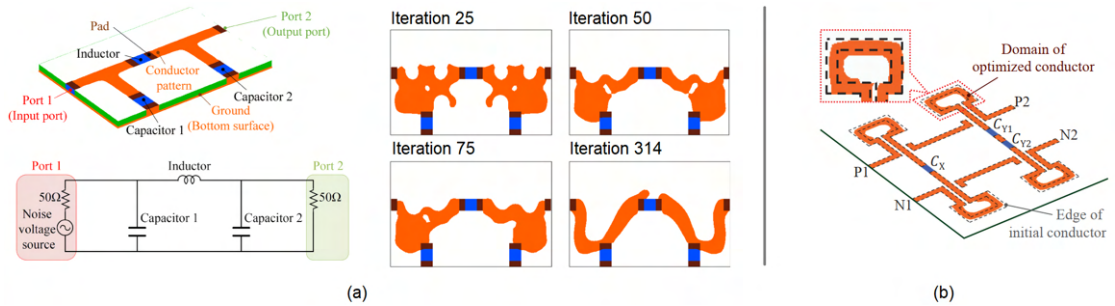


Figure 2.14: Conductor track design using the level-set method. (a) Formulation for connecting specific components in electrical circuits: Design problem and topology evolution [73]; and (b) Resulting topology for parasitic inductance cancellation in circuit board [74].

Uncategorized

Other computational methods exist but are less versatile and are restricted to specific design problems. An example worth mentioning is the use of stream functions [75, 76] to describe divergence-free surface currents instead of a physical coil. The isocontours of the stream function can be later used to represent the discretized turns. While dedicated to coil design and computationally efficient, such a formulation is based on the Biot-Savart equation and, thus, limited to applications in the air. It also requires a few evaluation points to stay computationally efficient. Furthermore, it can only design loops preventing the designed conductor from splitting into multiple ones, which could be an exciting feature depending on the application.

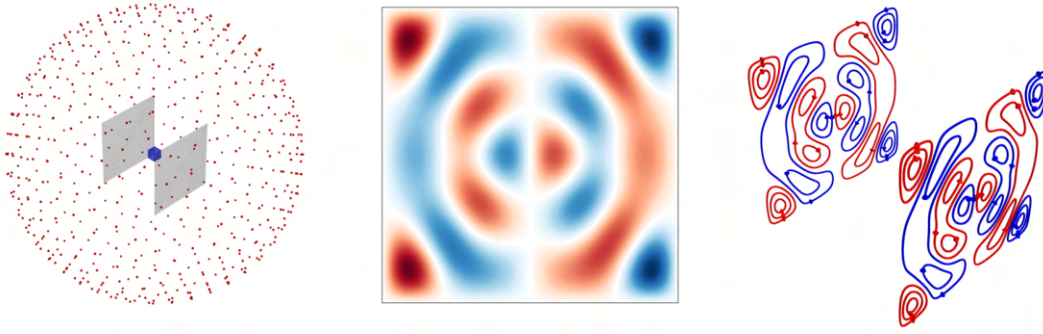


Figure 2.15: Example of stream function representation for coil design (taken from [76]): (left) Bi-planar coil surface meshes, target points in blue, and stray field points in red. (middle) Optimized stream function on one coil plane generates a homogeneous magnetic field along the X-axis. The colormap is linear and zero-centered. Red corresponds to negative and blue to positive values. (right) Discretized coil windings. The color and arrows indicate the current direction.

2.1.4 Room for improvement

The environment was limited to domains with similar magnetic properties (such as air and copper) in the few works designing conductor tracks with topology optimization. We propose to explore the design of conductor tracks in an environment also containing ferromagnetic domains, increasing the range of possible applications.

Furthermore, only 2-D formulations have been proposed, resulting in tracks or coils placed next to each other without overlapping. In this work, a 2.5-D formulation is proposed to tackle this limitation, enabling the design of coils spanning multiple layers. It provides more flexibility in the possible geometries because they are no longer restricted to a single plane.

When assembled, multiple coils form a group of coils or a so-called winding. In the state-of-the-art, the design of such a system has been achieved either by dividing the design domain into distinct fixed sub-spaces (for each individual coil) or by having coils fulfilling specific goals spatially far away from each other. However, nothing has been proposed to design closely packed coils that share the same design domain without *a-priori* knowledge of their geometry or position inside it. A *multi-coil* mapping is formulated in this work to achieve

such functionality. It permits the design of individual coils while accounting for packing with others.

Finally, explicit 3-D topology optimization of electric conductors has yet to be achieved. It is presented here for the first time and applied to the design of an electromagnet manipulator.

This thesis provides the foundations of a topology optimization framework to design electromagnetic coils for mechanical actuation. The implicit modeling of the turns in the design process is an interesting feature left to be implemented. Indeed, for now, only bulk material design is considered.

2.2 Advanced manufacturing of electromagnetic coils

THIS second part concerns unconventional manufacturing methods of electromagnetic coils for motor winding. The most common types of windings are first defined. Then, motor windings manufactured with the Printed Circuit Board (PCB) technology are introduced. Finally, the state-of-the-art of additively manufactured coils is presented and discussed. Many other alternatives exist but are beyond the scope of this work. Interested readers are invited to browse a review from 2022 on winding technologies, providing a broader scope on the subject [77].

2.2.1 Winding types

Two prominent winding families can be defined: *concentrated* and *overlapping* windings (as shown in Fig. 2.16). Concentrated winding consists of multiple coils (usually concentrating the flux at their center and wound around one tooth) that do not overlap. On the other hand, overlapping windings regroup all the other winding configurations with coils that somehow superimpose, having their individual coil-pitch overlay. Among them, the well-known *distributed* configuration is composed of distributed coils overlapping with each other outside the active length of the machine (i.e. at the end-winding, behind the slots, or outside the permanent magnet reach). Such winding can be composed of round wire or copper bars in the form of hairpins (among others) that help assemble the complete stator. When working with slotless machines, no more iron teeth obstruct the design space, allowing another type of overlapping winding: the *skewed types*. The overlap of the different coils can happen within the

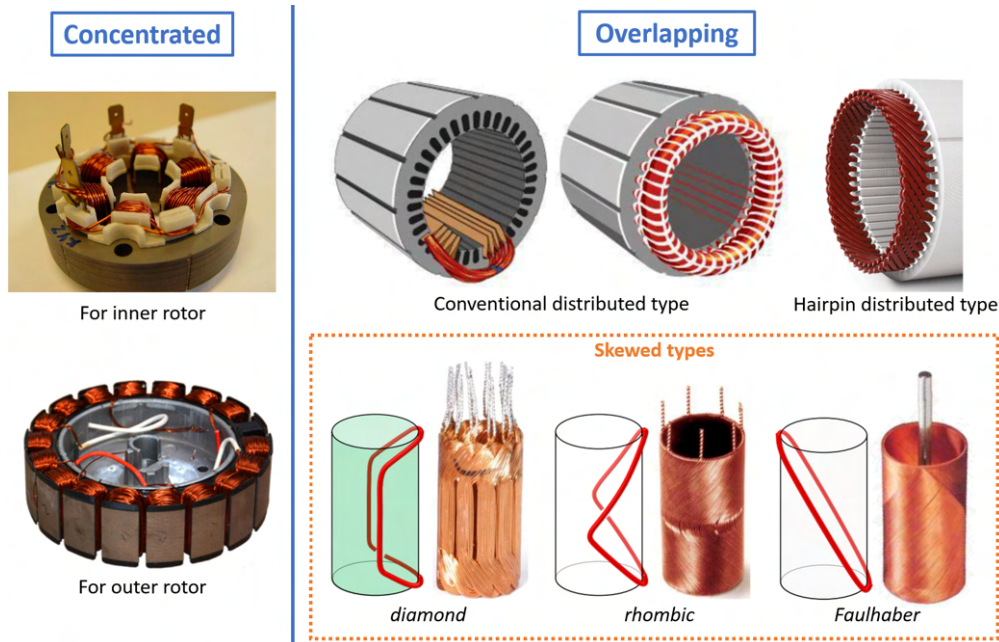


Figure 2.16: General winding families: Concentrated and Overlapping. Among the overlapping types, only stators for inner rotors are shown. There is the conventional distributed winding for slotted machines and skewed winding for slotless machines [78, 79, 80, 81].

active length of the machine, providing a better trade-off between electromagnetic coupling and conductor length (resistance). Various topologies have been explored for such machines [81, 18]. Three of them are presented in Fig. 2.16: the *diamond*, *rhombic* and *Faullhaber* (zigzag) types. In the literature, different terminologies describe these windings, such as *self-supported type* because no iron core maintains it, or *air-gap type*. After all, it is placed in the air region between the permanent magnets and the iron yoke.

2.2.2 Printed circuit board technology

Different winding manufacturing methods have been harvested in the past. Among them, the Printed Circuit Board (PCB) technology has recently gained popularity for slotless machines due to its maturity and ease of access in the electronics industry [83]. It can be directly used to form the whole stator of a linear machine [82], or for axial flux rotating ones [84] as these configurations contain the winding in a single plane. When different geometries are considered, like in a radial flux rotating machine, the *flex*-PCB technology can be used. The resulting flex winding has to be rolled in a cylinder to be inserted in the motor [19]. In addition to its advantage of industrialization and ease of integration, the PCB technology provides an additional degree of freedom in the winding design compared to the conventional rounded wire. Indeed, the conductive tracks still have a constant thickness but can have varying widths. This enables novel topologies with better motor constant achieved through a local reduction of the resistance of the tracks with larger widths [85]. Recently, it has been proposed to split the conductive tracks into multiple ones [86] to decrease the Eddy current losses. Despite all these advantages, the PCB technology remains a 2D fabrication technique limiting the possible geometry with its constant track thickness. Depending on its implementation, it is a subtractive manufacturing method, resulting in material waste. The commonly used substrate and insulating material for rigid PCB is fiberglass FR4 which has poor heat conductive properties [87]. This limits the cooling capabilities of the winding and, thus, the maximal operating current in the integrating motors.

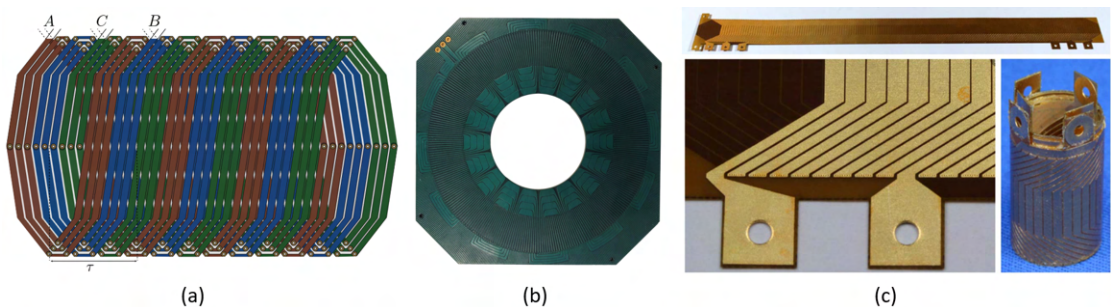


Figure 2.17: Printed Circuit Board (PCB) windings: (a) rigid PCB winding for linear machine [82]; (b) rigid PCB winding for rotating axial flux machine [83]; and (c) rolled Flex-PCB winding for rotating radial flux machine [62].

2.2.3 Additive manufacturing technology

The recent growth of metal additive manufacturing technologies [88] led to the fabrication of 3D-printed coils. Different technologies are available, but the most common is the Selective Laser Sintering (SLS) method, which focuses a laser onto a bed containing the metallic powder. It locally melts and sinters the different particles of the powder together, forming a solid. This process occurs in a 2-D plane, but repeating this operation for several layers can form a whole 3-D piece. More information on additive manufacturing technologies can be found in the following reviews dedicated to electrical machines and covering different components beyond the winding [89, 90, 91].

2.2.3.a Higher fill-factor and electrical conductivity

The first 3D-printed coils were fabricated in conventional topologies with specific cross-sections and turn profiles in order to improve the fill-factor of the winding. A larger fill-factor means more conductive material packed into a given space, which results in a more efficient device with lower resistance and less heat generation. It also enables a more compact design, which is advantageous in applications with limited space. Applications in the industry are already available, not only for concentrated coils [93] but also for hairpins-type [92]. As shown in Fig. 2.18, one can observe that the turns constituting the concentrated coils are distributed along the slot radial position only and not in the angular direction. This results in helical coils with wide conductors and a few turns.

In its early days, the SLS technique commonly resulted in *partially dense* pieces due to the porosity caused by poorly sintered powder. Nowadays, fully dense pieces can be obtained. However, fully dense printed pieces do not have the same bulk material properties [94]. The manufacturing process affects the metallurgy of the piece altering its mechanical, thermal, and electrical properties. It raises an important limitation for 3D-printed coils: the pieces regularly have lower electrical and thermal conductivity than bulk material. It depends on many parameters, such as the laser intensity, the powder quality, the sintering speed, the build orientation, and possible thermal treatments (post-processing). A study has been performed studying such effects for aluminum and copper alloys [95]. Nevertheless, some works have reported achieving conductivity $> 99\%$ IACS (International Annealed Copper Standard) for printed copper [96] and conductivity equal to the bulk for aluminum alloys after T6 heat treatment. The reduction of electrical conductivity provided by Additive Manufacturing (AM)



Figure 2.18: High fill-factor 3D-printed winding available in the industry: (left) concentrated coil, (right) hairpin-type [92].

could be harvested to improve the performance of some windings. Indeed, eddy current losses are reduced in conductors with lower electrical conductivity. Naturally, the corresponding Joule losses will increase. An inhomogeneous electrical conductivity between different turns or tracks constituting a coil has been proposed to harvest this trade-off in synchronous permanent magnet machines [97]. It has been experimentally achieved by splitting the coil into two different parts. They were printed separately with different build orientations in order to achieve different conductivities. A recent work proposed to control the conductivity of a sintered layer while printing a single piece by tuning the laser energy affecting the porosity of the sintered layer, and thus its electrical conductivity [98].

2.2.3.b Improved cooling properties

Proper thermal management in electromagnetic devices is important because the temperature affects their performance. Indeed, the electrical resistance increases with the temperature, resulting in more losses at a constant current which degrades the efficiency of the device. Additionally, the remanent magnetic flux density of permanent magnets decreases with a temperature increase, reducing the generated magnetic flux and so the power density. Finally, there is also a critical temperature above which the material insulating the turns would melt, resulting in potential damage of the device. Thus, it is attractive to keep an electromagnetic device at a low temperature or to be able to extract efficiently the heat generated by the different losses.

Hollow conductors constitute a possible solution for better thermal management as the hollow part serves as a channel for a cooling fluid to circulate or for the insertion of heat pipes. Such a method is suitable for machines with a predominant operating mode, where the skin depth coming from AC losses is fixed, leaving the possibility to remove the *useless* conductor in the center to form the cooling channels. This already exists for "wire"-technology with constant cross-section, but it has also been harvested using AM. Examples can be found in the literature for aluminum coils [99, 100] and copper alloy coils [95]. Straight channels or more complex shapes can be designed to extract better the heat generated inside the winding as shown in Fig. 2.19. This method is interesting but sacrifices space in the active region of the motor, where additional conductors or turns could be placed to contribute to power conversion. The turns also have a smaller effective cross-section (due to the space taken by the channel), degrading the DC resistance of the coil.

Another strategy explored to improve the thermal properties of electric motors is to use different insulating materials than conventional polymers that cover the conductors of the coil. Ceramics, for example, have a much better thermal rating with higher melting points and larger heat conductivity. However, due to their brittleness, ceramic insulated wires are expensive and delicate to wind. That is why a team from Germany developed a multi-material AM technique that simultaneously prints the conductive copper and the insulating ceramic forming a complete coil [101, 102] as shown in Fig. 2.20. The method is not SLS but is based on the inkjet technique, which binds metallic and ceramic powders with specific agents extruded from different nozzles. Impressive results were obtained with a maximal measured operating temperature up to 300°C. This team has also realized the first fully 3D-printed motor (except for the bearings) due to the possibility of printing the iron parts [100]. This method showed

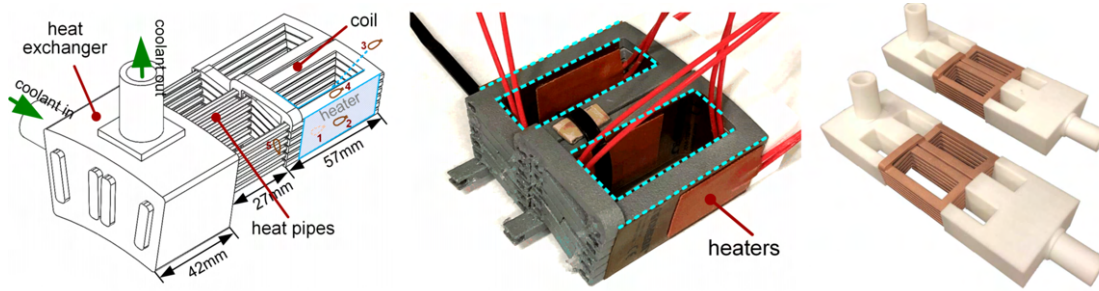


Figure 2.19: Coils 3D-printed with hollow conductors for heat pipes (left), or for fluid channels (right) to improve cooling properties [99, 95].



Figure 2.20: Multi-material additively manufactured coil with ceramic insulation [101, 102].

some limitations, such as an electrical conductivity decreased to 70% IACS, and a poor fill-factor due to the low resolution of the printing process that results in thick insulating layers of ceramic. Nevertheless, this technology is still in its early stage and is full of promises for the future.

2.2.3.c Novel geometries

Less conventional geometries have been recently 3D-printed. The first example revisits an old principle: Roebel bars to be used as winding for electric motors [103, 104, 105]. It is illustrated in Fig. 2.21. The 3D-printing process proposed by the company ADDITIVE DRIVES [92, 106] alleviates some of the manufacturing complexity and improves integration within the machine. This reduces the current displacement losses conventionally present in hairpin designs. Insulation is performed using vacuum pressure die-casting in a post-processing step.

Recently, more exotic shapes have been proposed to reduce AC losses in slotted synchronous permanent magnet machines. The proposed strategy is to *shape* the turns of the concentric coil so as to orient the flat section of the turn tangential to the magnetic fringes inside the slot. It enables reducing induced eddy currents in the coil due to the short effective cross-section normal to the varying magnetic flux. Its implementation harvests additive manufacturing of copper [107] as shown in Fig. 2.22. A later work based on the same concept proposed to change the profile of the turns to reduce the winding mass for applications with strong weight requirements [109]. Further design freedom was recently proposed in [108] by splitting the conductor into multiple strands at positions in the slot with higher varying magnetic flux that would lead to increased AC losses. The transposition of the turns is also proposed to

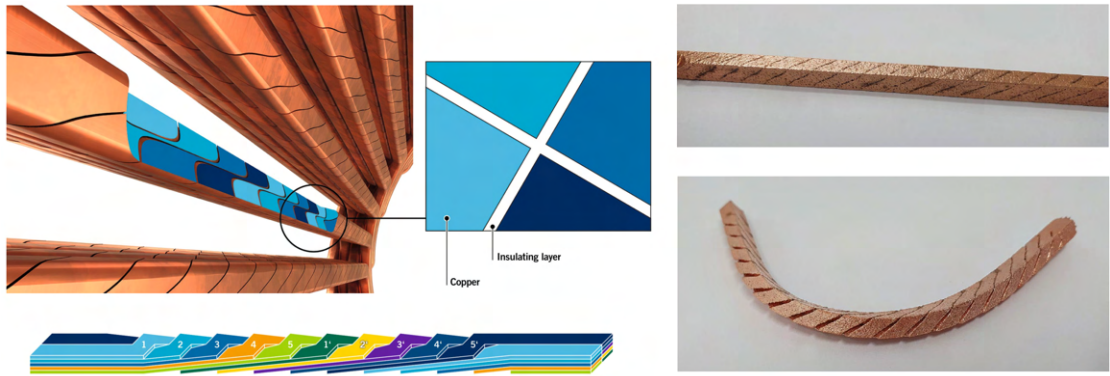


Figure 2.21: Roebel bars 3D-printed in copper [106].

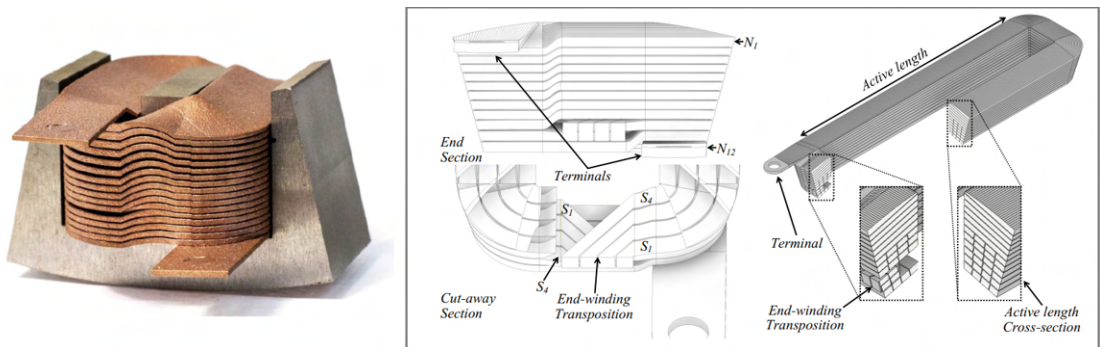


Figure 2.22: Shaped winding for reduced AC losses [107] (left), and conformal hybrid strand concept [108] (right).

reduce the circulating currents. It was defined as *conformal hybrid-strand* principle. The proposed methods are suitable for machines with a dominant operating mode because they can significantly reduce the associated AC losses. If no predominant operating mode could be identified, such an arrangement results in poorer use of the slot space with a lower fill-factor. However, this concept has not been manufactured yet. Only the distribution of the turns along the height of the coil has been successfully manufactured in the literature.

2.2.4 Room for improvement

The PCB technology has been shown as a great alternative to manufacturing winding due to its additional degree of freedom in the track design and its industrial maturity. However, the thickness of the tracks is still fixed, limiting possible improvement. The thermal properties of such winding also have to be studied and improved. Additive manufacturing technology is a candidate to alleviate such limitations.

One can observe that most of the additively manufactured windings were developed recently and even some during the progress of this thesis. This shows the great interest from the community and is encouraging for the field. Nevertheless, all the realized coils have their turns distributed along the coil height, in the manner of a helix. This arrangement forces the turn

width to be as large as the one of the coil, resulting in possible more significant AC losses due to their large cross-section. The first 3D-printed coil with turns distributed across its width, in the manner of a spiral, is realized in this work. Furthermore, no skewed-type 3D-printed winding has been proposed in the literature. They were all concentrated or distributed in slotted rotating machines. This manuscript describes the design, fabrication, and testing of a 3D-printed skewed winding integrated into a linear coreless (slotless) electrical machine. The freedom provided by AM is harvested to realize a novel concept of *completed* linear winding, improving the motor constant.

It has been shown that hollow conductors can improve the thermal properties of the winding. However, such an approach increases the DC losses of the winding and results in poor fill-factor and packing of the winding within the machine. A novel concept of multi-functional winding is proposed in this work. The electromagnetic and thermal functionalities are integrated into a single part, forming a coil with integrated heat sinks within its coil head. The proposed method does not degrade the coil's DC resistance, resulting in ideal packing. The machine's thermal properties are improved without relying on forced cooling methods.

3 COMPUTATIONAL DESIGN OF ELECTRIC CONDUCTORS

Content

3.1 Topology optimization of conductor tracks in 2-D	30
3.1.1 Physics	30
3.1.2 Density-based topology optimization formulation	35
3.1.3 Study-cases and results	38
3.1.4 Discussion and conclusion	47
3.2 Winding design and 2.5-D topology optimization	49
3.2.1 Winding design: a multi-coil interpolation scheme	49
3.2.2 2.5-D topology optimization for overlapping winding design	53
3.2.3 Discussion on the novel topology	57
3.2.4 Conclusion	59
3.3 Asymmetric winding design in 3-D topology optimization	60
3.3.1 Formulation	60
3.3.2 Design problem: a 3-D electromagnet manipulator	62
3.3.3 Conclusion	69
3.4 Fabricated topology-optimized coils	70
3.5 Conclusion	72

This part describes the topology optimization framework developed to design additively manufactured coils. The formulation achieving single coil design in 2-D is first presented. It is followed by the formulation achieving symmetric and then asymmetric winding design. Finally, the fabrication of such topology-optimized coils is discussed.

3.1 Topology optimization of conductor tracks in 2-D



THE first step for achieving a general computational design framework for coils is to establish the foundation for automated conductor design in 2-D. The implemented physics are presented based on [110, 38]. Then, different metrics evaluating the performance of a conductor layout are formulated. They can be used as the objective function or constraints to the optimization problem. It is followed by the general formulation of the topology optimization method applied to the design of conductors. Finally, the presented framework is applied to various design problems highlighting its strengths and limitations.

3.1.1 Physics

Several physics can govern the design of electromagnetic coils. In the scope of this work, the focus is put on static phenomena, discarding effects from oscillating electric currents and magnetic fields. This results in the absence of non-linear effects coupling the electric current and the associated magnetic field. The analysis is thus limited to solving an electric conduction problem, followed (or not, depending on the problem) by evaluating the magnetic flux density generated by the flowing current. Saturation effects are also discarded, assuming linear magnetic properties of the ferromagnetic parts. Solving these physics corresponds to the FEA of the problem. Single conductor design is considered here without implicit turn modeling. Only one "turn" is associated with a conducting track. The resolution of the mesh will thus directly impact the minimal size a track/turn can take. Implicit modeling of the turns could be addressed in future work to enable the design of coils containing many filaments/turns (a mesh cannot model that with a reasonable size). The symbols indicated in *bold* correspond to vectors in the physical space with components along the associated coordinate system.

3.1.1.a Electric conduction

The standard electric conduction problem inside a 2-D domain Ω (corresponding to the design domain) investigates the electric potential distribution $U = U_{(x,y)}$ inside the domain. The electrical conductivity distribution $\sigma = \sigma_{(x,y)}$ is defined according to the different materials present inside the design domain. It is, for example, equal to σ_{Cu} where copper is present and to $\sigma = \sigma_{\text{Air}}$ where air is present. In this work, a small conductivity is attributed to the air for numerical stability. The current density distribution $\mathbf{J} = \mathbf{J}_{(x,y)} = [J_x(x,y), J_y(x,y), 0]$ is thus defined everywhere inside the domain:

$$\mathbf{J}_{(x,y)} = -\sigma_{(x,y)} \nabla U_{(x,y)}. \quad (3.1)$$

The conservation of the electrical current is defined as follows:

$$\nabla \cdot \mathbf{J}_{(x,y)} = 0. \quad (3.2)$$

3.1 Topology optimization of conductor tracks in 2-D

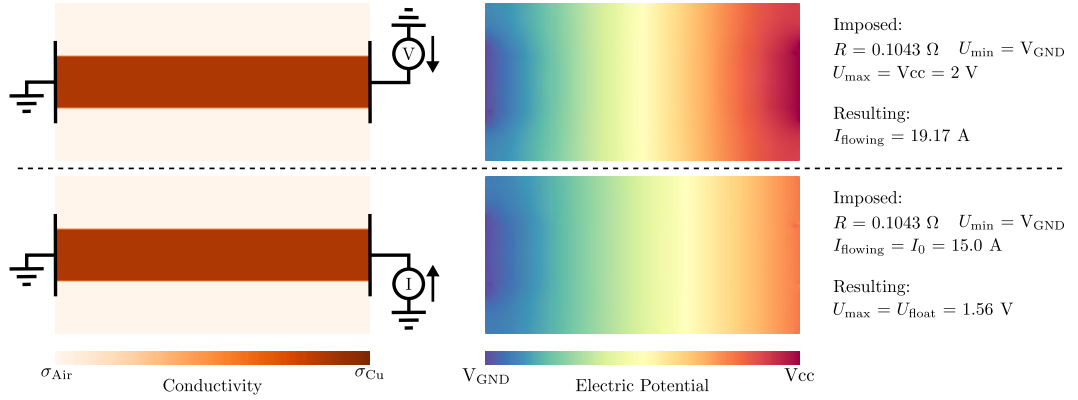


Figure 3.1: Example of a 2-D design domain with different electric boundary conditions: (top) voltage source; and (bottom) current source.

It leads to the Laplace equation governing the electric conduction phenomenon inside the domain:

$$-\nabla \cdot \sigma(x,y) \nabla U(x,y) = 0. \quad (3.3)$$

However, for a current to flow, one or multiple voltage drop(s) should be applied on some boundaries of the design domain. This can be achieved in two ways. In electrical engineering, there are known as a *voltage-source* or a *current-source* as shown in Fig. 3.1. From a physical and more general point of view, this corresponds to imposing the electric potential (voltage) directly for the first one and imposing a floating potential that assures a constant current on a specific boundary for the second. Naturally, these configurations can be used independently or combined. In the scope of automated coil design where the electrical conductivity distribution is varying and not *a-priori* known, the associated resistance R varies too. If a voltage source (fixed voltage drop ΔU) is used, the flowing current I will vary accordingly to keep the product with the resistance constant (according to Ohm's law). On the other hand, if a current source is used, the flowing current will not vary with the changing electrical resistance. However, the floating potential will adapt accordingly on the associated boundary to keep the current constant. This floating potential might take large unrealistic values if the topology creates an open circuit (corresponding to a topology with huge effective resistance). The choice of the source type depends on the problem to solve. The first problems presented in Section 3.1.3 and Section 3.2 implement a voltage source, and the problem presented in Section 3.3 implement multiple current sources. The source type is determined through the BCs applied to our problem. A simple example is shown in Fig. 3.1 to highlight the difference between a voltage and current source.

An FEA consists in solving numerically the mathematical model describing the physics of our problem. It relies on *finite-elements* defined on the discretized design space forming a mesh. The studied problems are mathematically described by a PDE, which brings challenges to assure differentiability when relying on numerical methods. That is why the *weak form* of the problem is used because it reformulates the initial differential equation into an integral equation which is more straightforward to solve. More information on these formulations and methods can be found in [38, 111]. This work does not aim to provide all the theories behind the finite element method and its implementation. Nevertheless, as the topology

optimization relies heavily on FEA, the weak form describing the problem is still required and is thus presented in this section. Only the form for voltage sources (Dirichlet BCs) is shown here for clarity, but the one for current sources is still derived in Appendix A.

There are multiple ways of enforcing Dirichlet boundary conditions to such a problem. A *strong* imposition corresponds to direct modification of the matrix system describing the discrete formulation of the problem. A *weak* imposition of these conditions to the variational problem is often preferred (resulting in a Nitsche-type formulation). Indeed, this does not require complex matrix manipulation but simple additional terms to the variational form, which do not degrade the computational cost when adding more conditions. This method is implemented in this work. Interested readers are invited to investigate [111] for more information. In the case of a single voltage source, the boundary of the design domain Ω is defined as follows: $\delta\Omega = \Gamma_D^{\text{Vcc}} \cap \Gamma_D^{\text{GND}} \cap \Gamma_{\text{N0}}$, with Γ_D^{Vcc} , Γ_D^{GND} the boundary onto which the electric potential is imposed to Vcc and 0 (ground GND) respectively. Γ_{N0} represents the remaining boundaries onto which homogeneous Neumann BCs are assured. They can be formulated as follows:

$$U_{(x,y)} = \text{Vcc} \text{ on } \Gamma_D^{\text{Vcc}}, \quad U_{(x,y)} = 0 \text{ on } \Gamma_D^{\text{GND}}, \quad \frac{\partial U_{(x,y)}}{\partial \mathbf{n}} = 0 \text{ on } \Gamma_{\text{N0}}, \quad (3.4)$$

with \mathbf{n} the vector normal to the boundary. The variational problem associated with the weak form is thus derived as follows:

$$\begin{aligned} \text{Find: } & u \in \mathcal{U}, \quad \forall v \in \mathcal{V} \\ \text{such that:} & \\ & \iint_{\Omega} \sigma_{(x,y)} \nabla u \cdot \nabla v \, dS = 0, \end{aligned} \quad (3.5)$$

with $u = u_{(x,y)}$ the trial function, and $v = v_{(x,y)}$ the test function. Considering $H^1(\Omega)$ the Sobolev space containing functions with squared value and squared first derivatives with finite integral over the design domain¹, $\mathcal{U} \subset H^1(\Omega)$ is the trial space satisfying the Dirichlet BCs specific to this problem, and $\mathcal{V} \subset H^1(\Omega)$ is the corresponding test space. The resolution of (3.5) leads to the definition of the electric potential distribution $U_{(x,y)} = u_{(x,y)}$. The current density distribution is then derived using (3.1).

3.1.1.b Magnetic fields

Two independent types of magnetic fields are considered in this thesis: the one coming from an external source (indicated by the index "ext") such as permanent magnets; and the one generated by the current flowing through the coil being designed (indicated by the index "coil"). They could be considered simultaneously but will be studied individually in this work. Fig. 3.2 shows an example considering the external magnetic flux density imposed in the design domain $\mathbf{B}^{\text{ext}}_{(x,y)}$. The analysis is in 2-D, and the magnetic flux density will be assumed normal to the design plane: $\mathbf{B}^{\text{ext}}_{(x,y)} = [0, 0, B_z^{\text{ext}}_{(x,y)}]$. In this case, the FEA is limited to the electric conduction problem. The mechanical properties can be derived from the Lorentz

¹ $H^1(\Omega) = \left\{ u \in L^2(\Omega); \frac{\partial u}{\partial x}, \frac{\partial u}{\partial y} \in L^2(\Omega) \right\}$ with $L^2(\Omega) = \left\{ f : \Omega \rightarrow \mathbb{R} : \iint_{\Omega} \|f\|^2 \, dS < \infty \right\}$

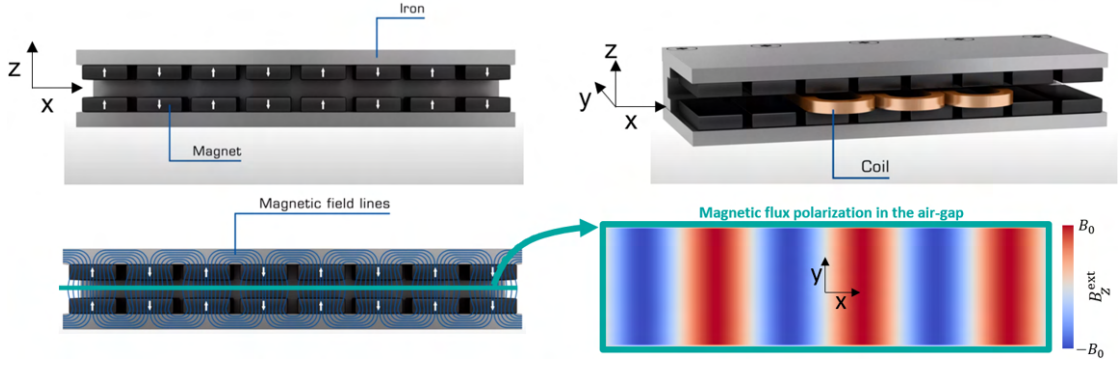


Figure 3.2: Example of a study case relying on the Lorentz force principle, restraining the analysis to a simple electric conduction problem. (Figure modified from [112].)

force resulting from the interaction of the electric current flow and the externally imposed magnetic flux density.

Conversely, when the magnetic flux density distribution generated by the coil $\mathbf{B}^{\text{coil}}(x,y)$ is needed, additional computation is necessary. As the current flows inside the 2-D plane, two more individual FEAs are necessary to derive the magnetic field assumed normal to the plane: $\mathbf{H}^{\text{coil}}(x,y) = [0, 0, H_z^{\text{coil}}(x,y)]$. Ampere's law for magnetostatics states:

$$\nabla \times \mathbf{H}^{\text{coil}}(x,y) = \mathbf{J}(x,y). \quad (3.6)$$

The corresponding magnetic flux density is derived as:

$$\mathbf{B}^{\text{coil}}(x,y) = \mu(x,y) \mathbf{H}^{\text{coil}}(x,y), \quad (3.7)$$

with $\mu(x,y)$ the magnetic permeability distribution inside the domain. It is equal to μ_{Fe} in the regions containing iron and μ_{Air} in the regions that are non-ferromagnetic. In this manuscript, these material properties are assumed constant, discarding non-linear and anisotropic effects. The 2-D analysis restrains this equation to $B_z^{\text{coil}}(x,y) = \mu(x,y) H_z^{\text{coil}}(x,y)$. Eq. (3.6) can not be solved directly and requires additional steps. As the magnetic flux density is conserved ($\nabla \cdot \mathbf{B}^{\text{coil}} = 0$), we define the magnetic vector potential $\mathbf{A}(x,y) = [A_x(x,y), A_y(x,y), 0]$ such that:

$$\nabla \times \mathbf{A}(x,y) = \mathbf{B}(x,y). \quad (3.8)$$

This definition results in the absence of uniqueness of the magnetic vector potential. A *Coulomb gauge* is proposed to fix its values:

$$\nabla \cdot \mathbf{A}(x,y) = 0. \quad (3.9)$$

When combining (3.6), (3.7), and (3.8) one can obtain:

$$\nabla \times \left(\frac{1}{\mu(x,y)} \nabla \times \mathbf{A}(x,y) \right) = \mathbf{J}(x,y), \quad (3.10)$$

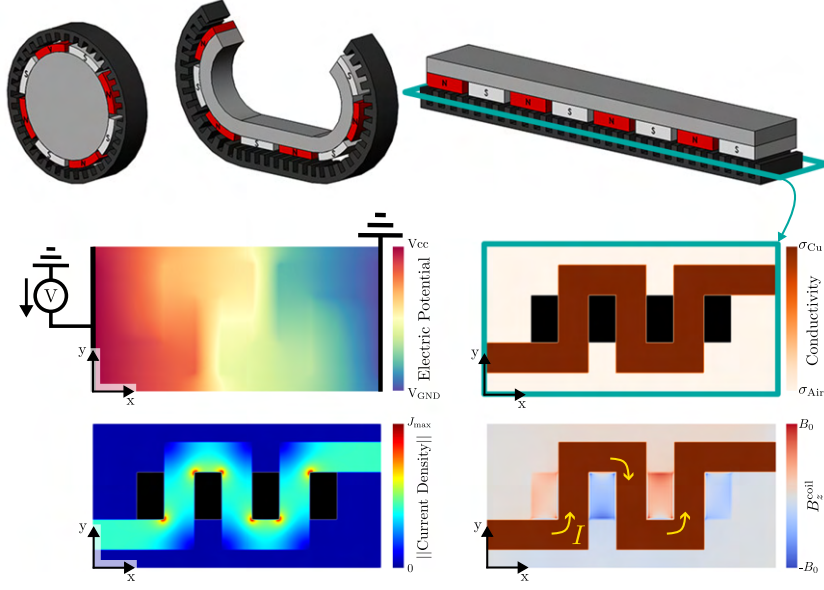


Figure 3.3: Example of a study case relying on the explicit computation of the magnetic field generated by the coil. The black rectangles represent the cut iron teeth. (The figures at the top were taken from [113].)

which leads to the following two following equations (using the Coulomb gauge):

$$\begin{aligned} -\nabla \cdot \frac{1}{\mu(x,y)} \nabla A_x(x,y) &= J_x(x,y), \\ -\nabla \cdot \frac{1}{\mu(x,y)} \nabla A_y(x,y) &= J_y(x,y). \end{aligned} \quad (3.11)$$

One can observe that these two equations are Poisson's equations. The Laplace equation in (3.3) being a specific case of the Poisson equation, the same function and derivation can be used to determine the weak form and corresponding variational problem. Homogeneous Dirichlet BCs are applied to the contour of the domain. Once solved, the magnetic flux density distribution can be derived: $B_z^{\text{coil}}(x,y) = \frac{\partial A_y(x,y)}{\partial x} - \frac{\partial A_x(x,y)}{\partial y}$.

3.1.1.c Metrics

Once the physical distributions are known, such as the electric current density $\mathbf{J}(x,y)$ or the generated magnetic flux density $B_z^{\text{coil}}(x,y)$, different metrics can be computed to evaluate the performance of the design. These metrics are all scalar values and could be used as the objective function or constraints to the topology optimization problem. The first general metric that can be computed is Q the Joule loss:

$$Q = t \iint_{\Omega} \sigma(x,y) |\nabla U(x,y)|^2 dS, \quad (3.12)$$

with t the thickness of the track (length along the z -axis) assumed constant over the domain.

3.1 Topology optimization of conductor tracks in 2-D

The electrical resistance can also be derived:

$$R = (\Delta V)^2 / Q. \quad (3.13)$$

This definition is associated with a dipole subject to a voltage drop ΔV . In the case described in (3.4), it is $\Delta V = V_{cc} - 0 = V_{cc}$.

When considering the magnetic field generated by the coil being designed, the magnetic flux $\Phi = [0, 0, \Phi_z]$ generated through a surface of interest S_{ROI} can be derived as an additional metric:

$$\Phi_z^{S_{ROI}} = \iint_{S_{ROI}} B_z^{coil}(x, y) dS. \quad (3.14)$$

The Lorentz force can be derived when considering the magnetic field imposed by an external source. It is defined as follows $\mathbf{F} = [F_x, F_y, 0] = \iiint_V \mathbf{J}(x, y) \times \mathbf{B}^{ext}(x, y) dV$ assuming no external electric field. Its two components are defined as:

$$\begin{aligned} F_x &= t \iint_{\Omega} J_y(x, y) \cdot B_z^{ext}(x, y) dS, \\ F_y &= t \iint_{\Omega} -J_x(x, y) \cdot B_z^{ext}(x, y) dS. \end{aligned} \quad (3.15)$$

Another interesting factor when considering coil design is the so-called *motor constant* k_m developed to compare electric machines. It corresponds to a trade-off between the force and the generated losses. This specific measure is independent of the supplied current and is thus independent of the type of electrical source considered. k_F is the force constant ($k_F = F_x / I$). In this work, interest is put on the motor constant associated with the Lorentz force generated along the x -axis only, but the others can be derived accordingly:

$$k_m = \frac{F_x}{\sqrt{Q}} = \frac{k_F}{\sqrt{R}}, \quad (3.16)$$

3.1.2 Density-based topology optimization formulation

3.1.2.a General formulation

This section describes the general density-based topology optimization formulation developed to design conductor tracks in 2-D. The optimization problem (2.1) and the flowchart depicted in Fig. 2.2 stay valid. The physics presented above correspond to the FEA block, while the metrics can be used as the objective function or the constraints. Before determining the *control variables*, let us first define the topology of the structure being designed. It is described by a distribution of *artificial densities*:

$$\rho = \rho(x, y) \in]0, 1]. \quad (3.17)$$

They vary continuously between a small value close to 0 ($\sim 1 \times 10^{-3}$ to prevent numerical instabilities) and 1, representing air and copper, respectively. These two bounds are referred to *full-materials*, while the values between these two are referred to *intermediate-materials*. This

distribution is discretized at the nodes (or elements depending on the chosen finite element function space) and can be reconstructed everywhere using proper interpolating functions. In this work, the corresponding nodal values serve as *control variables* for the optimization problem. They need to be linked to the material properties used in the FEA to provide control to these variables over the chosen metrics (objective function and/or constraints). However, some intermediate steps are commonly used in topology optimization to encode some implicit behavior. A *filtering* step is first required to enforce a minimal length scale within the designed structure. The *Helmholtz-type* PDE [51, eq. 11] is implemented in this work:

$$\tilde{\rho} = \tilde{\rho}(x,y) = h_{\text{filt}}(\rho(x,y), \tilde{\rho}(x,y)) = \rho(x,y) + r_{\text{filt}} \nabla^2 \tilde{\rho}(x,y), \quad (3.18)$$

with $\tilde{\rho}(x,y)$ the distribution of filtered variables, and r_{filt} the filter radius controlling the minimal feature size. An undesired feature resulting from this filtering is the *blurring* of the topology boundaries creating intermediates materials as shown in Fig. 3.5. A *projection* step is thus proposed to obtain a crisper topology. The hyperbolic tangent projection scheme [53, eq. 9] is used in this work to assure differentiability:

$$\hat{\rho} = \hat{\rho}(x,y) = h_{\text{proj}}(\tilde{\rho}(x,y)) = \frac{\tanh(\beta(\tilde{\rho}(x,y) - 0.5)) + \tanh(0.5\beta)}{2 \cdot \tanh(0.5\beta)}, \quad (3.19)$$

with $\hat{\rho}(x,y)$ the distribution of projected variables, and β the projection parameter representing the strength of projection. The maximal value of $\beta = \frac{r_{\text{filt}}}{l_e}$, is set in this work. l_e is the average length of an element of the mesh. The resulting distribution can then be mapped to material properties. In this work, it corresponds to the electrical conductivity distribution $\sigma = \sigma(x,y)$ presented in Section 3.1.1.a. It is performed through the MIS step. Here, the RAMP scheme [26, eq. 5] is used:

$$\sigma = \sigma(x,y) = h_{\text{RAMP}}(\hat{\rho}(x,y)) = \sigma_{\text{Air}} + (\sigma_{\text{Cu}} - \sigma_{\text{Air}}) \frac{\hat{\rho}(x,y)}{1 + q(1 - \hat{\rho}(x,y))}, \quad (3.20)$$

with q the penalty factor of the RAMP scheme further discussed in Section 3.1.2.b. The various steps linking the control variables to the material properties used for the FEA in the 2-D topology optimization of conductor tracks are summarized below:

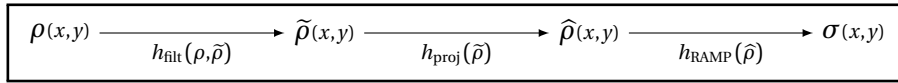


Figure 3.4: Flowchart of the 2-D topology optimization of conductor tracks.

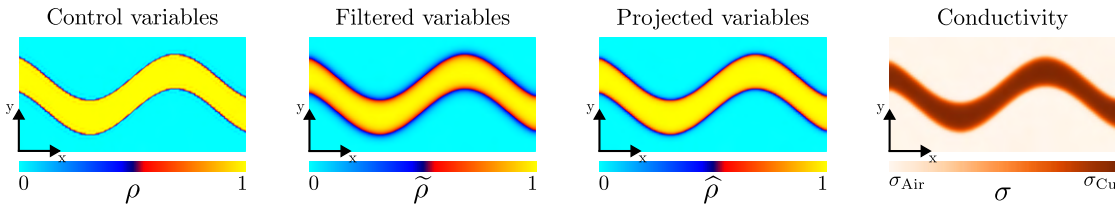


Figure 3.5: Example of the different distributions resulting from the flowchart of the 2-D topology optimization.

The dependency of the control variables on the material properties propagates its effect on the physical properties of the design and, thus, on the different evaluated metrics. These dependencies are then back-propagated to determine their respective sensitivity using the chain rule and the adjoint variable method as described in [114]. The chosen objective function or constraints will depend on the solved design problem. Nevertheless, a general constraint commonly used in topology optimization is the *volume limitation*. It provides an upper bound to the total of material distributed over the design domain, reducing the search space and providing control on the amount of material composing the design:

$$g_{\text{vol}}(\rho) = \frac{\iint_{\Omega} \rho(x,y) d\Omega}{\iint_{\Omega} 1 d\Omega} \leq \text{Vol}^*, \quad (3.21)$$

with Vol^* the maximal volume fraction of material desired.

3.1.2.b More on the Material Interpolation Scheme

As shown in Fig. 2.5, the goal of the MIS is to penalize the intermediate densities by giving them a lower effective conductivity. Indeed, when combined with a volume limitation, this function makes the intermediate materials "less attractive" to the optimizer which will then remove them. Naturally, this "attractiveness" is valid only if the objective function improves with larger electric conductivity. The MIS is an essential part of topology optimization. It permits the implicit encoding of desired features in the resulting topology, removing the need for additional constraints explicitly given to the optimization problem. Indeed, the intermediate densities could be explicitly forbidden or penalized in the optimization problem (resulting in a tremendous number of constraints or other global measures), degrading the computational cost. Meanwhile, they are penalized through the MIS, implicitly removing them without increasing the computation time. This is mainly done for the problem of intermediate densities, but other features could be accounted for with the MIS. This mechanism is largely harvested in this work and further discussed in Section 3.2, and Section 3.3.

Furthermore, the MIS is characterized by a penalty factor, providing more or less strength on the penalization mechanism (the larger it is, the more penalized the intermediate densities are). One could use a large penalty value to remove the intermediate materials effectively. However, the chosen method relies on gradient-based optimizers, which are subject to local optima. Thus, it is advised to continuously increase the penalty factor throughout the optimization to prevent a too fast convergence to local optimum [115, 116]. It is called a *continuation scheme*, and in practice, it updates the penalty factor every N -iterations, with N a pre-selected number of iterations. Ideally, N should be large enough to prevent being stuck in a local optimum but should be kept low enough not to degrade too much the computational time.

3.1.2.c Units and order of magnitude in topology optimization

Using smaller values for the material properties prevents numerical instabilities from rising when considering materials with several orders of magnitude differences. It is common when dealing with topology optimization. The optimization behaves smoothly as long as the different considered materials are *different-enough*. The physical laws stay valid; only

the considered materials are modified². Attention is drawn to the importance of the relative change of the different metrics between the different topologies, not their absolute value. The performance could be scaled back properly in a post-processing step. The following are used in this work: $\sigma_{\text{Air}} = 5.0 \times 10^{-3}$ S/m, $\sigma_{\text{Cu}} = 3.5$ S/m, and $\mu_{\text{Air}} = 4\pi \times 10^{-3}$ N·A⁻², $\mu_{\text{Fe}} = 1000\mu_0$. Furthermore, in 2-D FEA, the depth of the domain is considered "large enough" with respect to the other dimensions not to affect the results. In the selected framework, this assumes considering a normalized thickness/depth of $t = 1$ m. This large value (with respect to the dimensions of the selected problem) affects the numerical values of the different metrics, which could be several orders of magnitudes different from realistic values. Thus, using smaller material properties also permits us to compensate numerically for this difference without explicitly considering the thickness of the problem.

3.1.3 Study-cases and results

This section aims to demonstrate the feasibility, strengths, and limitations of the topology optimization method applied to the design of 2-D conductor tracks. The method is applied to different design problems split between two groups: the first one studies problems where the considered magnetic field is generated directly by the coil being designed, and the second considers external magnetic fields imposed over the design domain by an external source. The framework is built upon the FEniCS library [117]. It is a popular open-source computing platform for solving PDEs based on variational problems. It allows straightforwardly to create finite element functions associated with any mesh. Such a formulation strongly assists the definition of the different distributions necessary for the FEA and the density-based topology optimization. The sensitivity of the problem is derived using the adjoint variable method and automatic differentiation tools already implemented within the FEniCS framework in the *pyadjoint* library [118, 43]. This significantly simplifies the implementation of our computational design method, as the gradient computation is usually the most time-consuming to derive. The optimizer selected in this work is the IPOPT [35] compiled with the MA57 [119] linear solver. The optimizations are performed on a Linux workstation with an Intel i7 8-core processor and 16G memory.

The considered 2-D domains have a size of $l_x \times l_y = 100 \text{ mm} \times 50 \text{ mm}$. The different finite element functions are characterized by *Lagrange* interpolation functions [111, chap. 2.4.2] of the first order (to assure differentiability). This results in distributions defined explicitly on the mesh's vertices and interpolated elsewhere.

Some of the presented examples rely on multi-objective optimization. The weighted sum of the different sub-objectives is implemented. The corresponding weights are determined "manually" by running multiple simulations with different sets of weights. The goal here is to demonstrate the proposed method's potential to solve various design problems automatically. There is no thorough study of the best trade-off between the different sub-objectives. This corresponds to the study of *Pareto fronts* and other multi-objective optimization strategies [120, 121], which is beyond the scope of this thesis.

²Any metal is a good conductor with respect to air.

3.1.3.a Magnetic field generated by the conductor being designed

This subsection describes the automated design process of conductor tracks in 2-D, targeting the largest magnetic flux possible in different ferromagnetic regions of interest. The presented formulation enables the control of the flux direction inside different Regions Of Interest (ROI) and the relative magnitude between them. The iron regions are considered to be electrically insulated from the conductor being designed, with a corresponding effective conductivity equal to σ_{Air} . Their magnetic permeability $\mu_{(x,y)}$ is equal to μ_{Fe} , while the non-magnetic regions (such as air or copper) have a permeability equal to μ_{Air} .

Control of the flux direction

The first design problem aims to generate the largest magnetic fluxes in four iron ROIs with alternating directions for a limited volume of copper. The ROIs have a size of $l_x^{Fe} \times l_y^{Fe} = 10 \text{ mm} \times 16.667 \text{ mm}$. A voltage drop ΔV is applied across the design domain, corresponding to a positive fixed electric potential on the left boundary $V_{cc} = 10 \text{ V}$, and a grounded right boundary (similarly to Fig. 3.3). The domain is meshed uniformly into 10'000 triangular elements defined by 5'151 vertices (i.e., DOFs because the different distributions are defined by *Lagrange* interpolating functions of first order). After removing the ones present in the iron regions, the total number of DOFs of the artificial density distribution is 4'539. This corresponds to the number of control variables. The objective function to minimize is set to:

$$f = - \sum_{i=1}^4 s_i \cdot \Phi_z^{S_{ROI:i}}, \quad (3.22)$$

with $s_i = \{+, -\}$ the sign indicating the desired flux direction in the ROI i . The minus sign in front of the sum assures maximization of the fluxes while minimizing the objective function.

The following hyperparameters are used during the optimization: $r_{\text{filt}} = 0.4 \times 10^{-3}$, $\text{Vol}^* = 0.13$. The RAMP scheme is used with a penalty factor q continuously increased every 25 iterations using the following values: $\{0, 4, 8\}$. A reference topology (an engineer could have designed) is used to initialize the topology optimization. It is shown in the top part of Fig. 3.6, while the one resulting from the topology optimization is shown at its bottom. The corresponding metrics evaluated for the two different topologies are summarized in Table 3.1.

For the same amount of material and a fixed voltage drop, one can observe that the topology-optimized tracks generate larger magnetic flux in the regions of interest with the correct direction. A total increase of 14.7% is achieved. Two factors are responsible for this increase. Firstly, the designed tracks provide a better coupling with the different iron ROIs by splitting the conductor in two, better distributing the electric current closer to two neighboring regions whenever possible. Secondly, the electrical resistance of the tracks is lower, resulting in a larger flowing electric current and, thus, a larger electromagnetic potential. It is achieved by reducing the effective length of the tracks being designed. Indeed, as shown in Fig. 3.6, the tracks of the reference topology are straight, forming right angles, while the optimized one exhibit a curvier shape approaching the diagonals, and thus a smaller effective length. The exotic nature of the optimized topology would have been difficult to find for a human designer. The associated improvement in performance is significant, which confirms the strength of the automated design method.

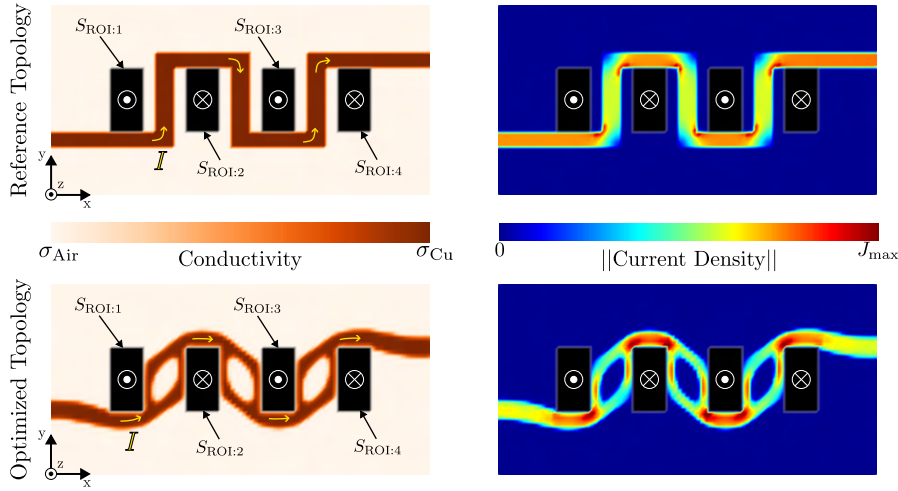


Figure 3.6: Design problem n°1: four iron teeth with alternating flux direction, and a voltage drop across the left and right boundaries. Comparison of a reference topology to the optimized one. Optimization time: 39 sec.

Table 3.1: Metrics evaluated for the reference topology and the optimized one for the design problem n°1.

	Vol*	ΔV (V)	R (Ω)	I (A)	$\Phi_z^{S_{ROI:1}}$ (μWb)	$\Phi_z^{S_{ROI:2}}$ (μWb)	$\Phi_z^{S_{ROI:3}}$ (μWb)	$\Phi_z^{S_{ROI:4}}$ (μWb)
Reference	0.13	10	10.6	0.95	2.49	3.72	3.76	2.56
Optimized	0.13	10	9.3	1.08	2.76	4.36	4.42	2.83
<i>Improvement</i>	-	-	-12.3%	+13.9%	+10.8%	+17.2%	+17.5%	+10.4%

Control of the flux magnitude

The previous example confirms the possibility of controlling the flux direction. However, this still needs to provide control over the relative distribution of the total flux between the different regions. A measure is needed to compare the fluxes passing in the different ROIs. The squared error between the squared flux in a first region i and a second region j is defined as:

$$\varepsilon_{i:j} = \left(\left(\Phi_z^{S_{ROI:i}} \right)^2 - \left(\Phi_z^{S_{ROI:j}} \right)^2 \right)^2. \quad (3.23)$$

Minimization of this term converges towards equal fluxes in the region i and in the region j . The fluxes are squared to be independent of the flowing direction. A weighted version of this error is proposed to provide control on the relative difference of fluxes between two regions:

$$\varepsilon_{i:j}(\gamma_i, \gamma_j) = \left(\left(\frac{\Phi_z^{S_{ROI:i}}}{\gamma_i} \right)^2 - \left(\frac{\Phi_z^{S_{ROI:j}}}{\gamma_j} \right)^2 \right)^2, \quad (3.24)$$

with γ_i, γ_j the weights controlling the relative fluxes between region i and j . If $\gamma_i = 4 \cdot \gamma_j$, the term above converges towards a flux in the region i four times larger than in region j .

A second design problem is studied to highlight this new functionality. Only two regions of interest are considered here for simplicity, but the proposed method could be extended to more regions. The same voltage drop as in the first design problem (over the left and right boundaries) is considered as BC. The iron regions still have the same size too. The domain is now meshed uniformly into 40'000 triangular elements defined by 20'301 vertices. After removing the ones present in the iron regions, the total number of DOFs of the artificial density distribution is 18'981. This corresponds to the number of control variables. The filter radius is set to $r_{\text{filt}} = 1.6 \times 10^{-3}$, while the penalty factor from the RAMP scheme is continuously increased every 25 iterations using the following values: {0, 4, 8}. The control variables are uniformly initialized to the volume fraction $\text{Vol}^* = 0.2$ in order to show that the automated design method does not need *a-priori* knowledge on the resulting topology.

Different objective functions are compared to show the strengths and limitations of the proposed formulation. The first objective function only contains the sum of the signed fluxes in the different ROIs:

$$f_1 = - \sum_{i=1}^2 s_i \cdot \Phi_z^{S_{\text{ROI}:i}}. \quad (3.25)$$

The second objective function integrates the weighted flux error as an additional sub-objective:

$$\begin{aligned} f_2 &= - \sum_{i=1}^2 s_i \cdot \Phi_z^{S_{\text{ROI}:i}} + \alpha^\varepsilon \cdot \varepsilon_{0:1}(\gamma_0, \gamma_1) \\ &= - \sum_{i=1}^2 s_i \cdot \Phi_z^{S_{\text{ROI}:i}} + \alpha^\varepsilon \cdot \left(\left(\frac{\Phi_z^{S_{\text{ROI}:0}}}{\gamma_0} \right)^2 - \left(\frac{\Phi_z^{S_{\text{ROI}:1}}}{\gamma_1} \right)^2 \right), \end{aligned} \quad (3.26)$$

with α^ε the weight associated with the error sub-objective. Different flux directions and distributions are tested using the following weights:

- $s_1 = +, s_2 = +, \gamma_1 = 1, \gamma_2 = 1: \quad \alpha^\varepsilon = 1.0$
- $s_1 = +, s_2 = +, \gamma_1 = 1, \gamma_2 = 2: \quad \alpha^\varepsilon = 5.0$
- $s_1 = +, s_2 = -, \gamma_1 = 1, \gamma_2 = 1: \quad \alpha^\varepsilon = 1.0$
- $s_1 = +, s_2 = -, \gamma_1 = 1, \gamma_2 = 2: \quad \alpha^\varepsilon = 1.5$

The topologies resulting from the optimizations are shown in Fig. 3.7, and the corresponding metrics in Table 3.2. The first observation (and limitation) of the proposed formulation is that the sole use of the *flux*-subobjective ($f = f_1$) is sometimes not enough to obtain a realistic topology. Indeed, for the cases $\{s_1 = +, s_2 = -\}$, the optimization struggles to converge to discrete solutions and contains mostly intermediate materials. However, when additional sub-objectives are added ($f = f_2$), the search space is restricted, resulting in more realistic solutions made of full-materials. This problem is recurrent in gradient-based topology optimization. Indeed, as local search is performed, the global optimum can not be assumed to be reached, and the solver is subject to getting trapped in a local solution that may lack significance for the designer. Nevertheless, the proposed method can achieve interesting results when more information is provided to the optimizer, such as an additional metric to consider. Table 3.2 confirms that the desired design requirements are met when the two sub-objectives are used

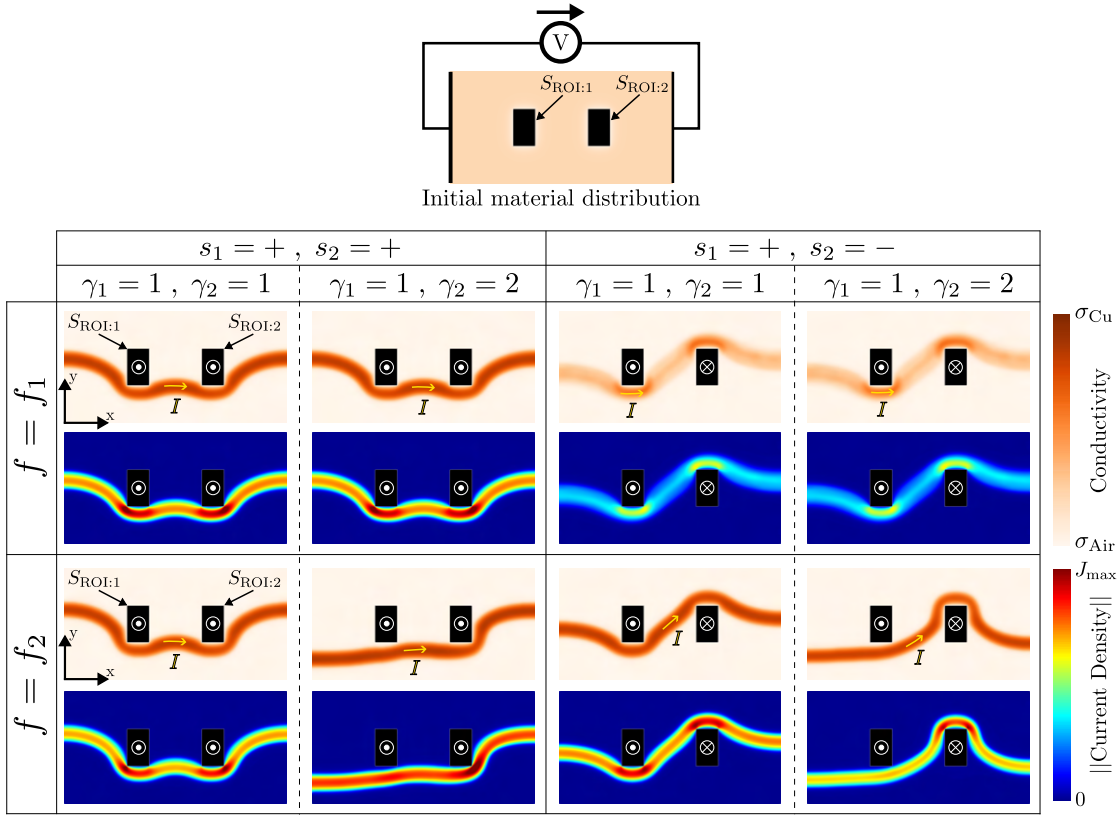


Figure 3.7: Design problem n°2: two iron teeth with a voltage drop across the left and right boundaries. Comparison of the topology optimization results for different flux directions, relative magnitudes, and objective functions. The shown J_{max} is equal to 0.31 A/mm^2 . The average optimization time is 156 sec per optimization.

Table 3.2: Metrics evaluated for the different topologies resulting from the design problem n°2.

s_1	s_2	γ_1	γ_2	f	$R \text{ (}\Omega\text{)}$	$I \text{ (A)}$	$\Phi_z^{S_{ROI:1}} \text{ (}\mu\text{Wb)}$	$\Phi_z^{S_{ROI:2}} \text{ (}\mu\text{Wb)}$	Ratio
+	+	1	1	f_1	6.53	1.53	2.374	2.402	1.012
				f_2	7.13	1.40	2.396	2.400	1.002
		1	2	f_1	6.53	1.53	2.374	2.402	1.012
				f_2	5.98	1.67	1.402	2.703	1.928
+	-	1	1	f_1	11.23	0.89	1.747	1.774	1.015
				f_2	6.70	1.49	3.025	3.023	0.999
		1	2	f_1	11.23	0.89	1.747	1.774	1.015
				f_2	8.22	1.22	1.754	3.451	1.967

together. The flux direction and distribution between different ROIs are controlled without needing *a-priori* knowledge on the resulting topology. The strength of the proposed method is to be able to combine several aspects into a single procedure. While an experienced designer could determine a conductor layout that correctly balances the flux between the two teeth, it would become quite challenging to still ensure maximization of the flux for the given amount of material. Indeed, the electrical current, which directly affects the magnetic flux magnitude, is inversely proportional to electrical resistance, which also depends on the conductor layout. The developed automated design approach can quickly generate solutions that consider several design requirements at the same time. Furthermore, this approach is flexible and can be applied to different problems without considering big changes in the formulation or design procedure.

Naturally, the proposed method still has limitations. Some design problems are more challenging to be solved than others. It is illustrated by studying a third design problem (left side of Fig. 3.8): the maximization of the flux in two iron teeth with a voltage drop across the same boundary (top and bottom side of the left boundary). When running the optimization as before, the topology converges to undesired solutions composed of only intermediate materials (not shown here). Thus, another objective function is proposed. It combines the previous one with an additional sub-objective corresponding to the weighted electrical resistance of the track being designed :

$$\begin{aligned} f_3 &= - \sum_{i=1}^2 s_i \cdot \Phi_z^{S_{ROI:i}} + \alpha^\varepsilon \cdot \varepsilon_{0:1}(\gamma_0, \gamma_1) + \alpha^R \cdot R \\ &= - \sum_{i=1}^2 s_i \cdot \Phi_z^{S_{ROI:i}} + \alpha^\varepsilon \cdot \left(\left(\frac{\Phi_z^{S_{ROI:0}}}{\gamma_0} \right)^2 - \left(\frac{\Phi_z^{S_{ROI:1}}}{\gamma_1} \right)^2 \right) + \alpha^R \cdot R, \end{aligned} \quad (3.27)$$

with α^R the weight associated with the electrical resistance. The minimization of this function advantages solutions with low electrical resistance, favoring full materials defining highly conductive tracks. Three different optimizations are performed for different relative flux magnitudes. The weights associated with the sub-objectives are fixed to $\alpha^\varepsilon = 7.0$ and $\alpha^R = 0.002$ in the three optimizations. The simulations are performed using the following set of weighted sub-objectives: $\gamma_1 = 1$, $\gamma_2 = 2$: $\alpha^\varepsilon = 7.0$ and $\alpha^R = 0.002$. The filter radius is set to $r_{\text{filt}} = 1.6 \times 10^{-3}$, while the penalty factor from the RAMP scheme is continuously increased every 25 iterations using the following values: $\{0, 4, 8\}$. The densities are initialized uniformly to the volume fraction value $\text{Vol}^* = 0.3$. While the design requirements are met as shown in Table 3.3, one can observe that the different topologies do not converge to complete *full*-materials. More specifically, the shorter track turning around $S_{ROI:1}$ is more or less defined depending on the desired flux balance between the two teeth. While adding the weighted electrical resistance helped converge to more realistic topologies, some design problems must be more balanced to find a convenient solution. This could be alleviated by changing the definition of the design problem with different BC or providing a different initial guess. This limitation is common to gradient-based optimization methods. Nevertheless, the proposed method shows excellent flexibility to accommodate different design problems and find interesting solutions.

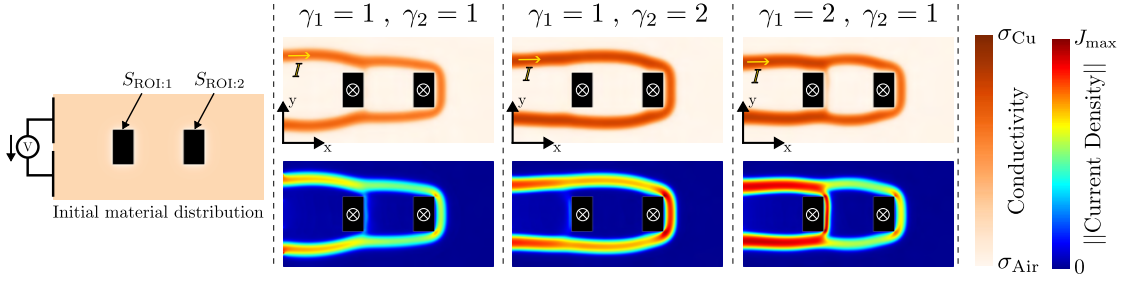


Figure 3.8: Design problem n°3: two iron teeth with voltage drop applied to the top and bottom side on the left boundary. Comparison of the topology optimization results for different relative flux magnitudes. f_3 is used as objective function with $\alpha^\varepsilon = 7.0$ and $\alpha^R = 0.002$. The shown J_{\max} is equal to 0.21 A/mm^2 . The average optimization time is 163 sec per optimization.

Table 3.3: Metrics evaluated for the different topologies resulting from the design problem n°3.

	$R \text{ } (\Omega)$	$I \text{ (A)}$	$\Phi_z^{S_{\text{ROI}:1}} \text{ } (\mu\text{Wb})$	$\Phi_z^{S_{\text{ROI}:2}} \text{ } (\mu\text{Wb})$	Ratio
$\gamma_1 = 1, \gamma_2 = 1$	10.69	0.94	1.392	1.392	1.000
$\gamma_1 = 1, \gamma_2 = 2$	8.63	1.16	1.446	2.882	1.984
$\gamma_1 = 2, \gamma_2 = 1$	7.44	1.34	2.772	1.397	0.504

3.1.3.b Magnetic field imposed by an external source

In this section, design problems considering only fixed magnetic flux density distributions generated by an external source $B_z^{\text{ext}}(x, y)$ are studied. This restricts the FEA to a single electric conduction. Several examples are shown to discuss additional features of the topology optimization method and validate the design methodology for *voice-coil*-type actuators, which will be specifically investigated in the rest of this thesis. Indeed, these problems do not contain ferromagnetic regions obstructing the design space, leaving more design freedom for the conductor to be designed.

A fourth design problem is formulated. It considers a magnetic flux distribution containing four magnetic pole pairs imposed inside the design domain by external permanent magnets. A sinusoidal distribution of amplitude B_0 and centered in the design domain is assumed here:

$$B_z(x, y) = \begin{cases} B_0 \cdot \sin\left(\frac{2\pi}{L_x^{\text{PP}}} \cdot x\right) & \text{for } \left|y - \frac{l_y}{2}\right| < \frac{L_y^{\text{PP}}}{2}, \\ 0 & \text{otherwise,} \end{cases} \quad (3.28)$$

with $L_x^{\text{PP}} = l_x/4$, $L_y^{\text{PP}} = l_y/2$ the span of a magnetic pole-pair along the x - and y -axis respectively. B_0 is fixed to 0.8 T . A voltage drop of 10 V is applied to the top boundary as shown in Fig. 3.9. The filter radius is fixed to $r_{\text{filt}} = 1.6 \times 10^{-3}$ and the penalty factor of the RAMP scheme is continuously increased every 25 iterations using the following values $\{0, 4, 8\}$. The topology is uniformly initialized to the volume fraction value $\text{Vol}^* = 0.4$. The first optimization minimizes the electrical resistance (3.13). The resulting topology shown in Fig. 3.9 is described by the accumulation of material around the localized voltage drop, creating a *short-circuit*,

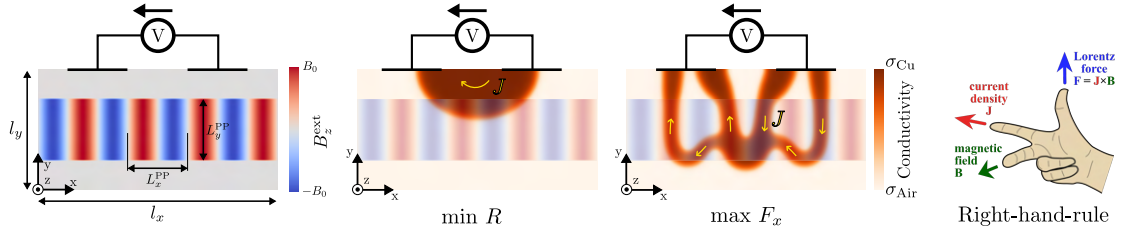


Figure 3.9: Design problem n°4: Four alternating pole pairs imposed by an external magnetic field source. Example for the minimization of electrical resistance and maximization of the Lorentz force along the x -axis. The right-hand rule confirms the direction of the flux [122].

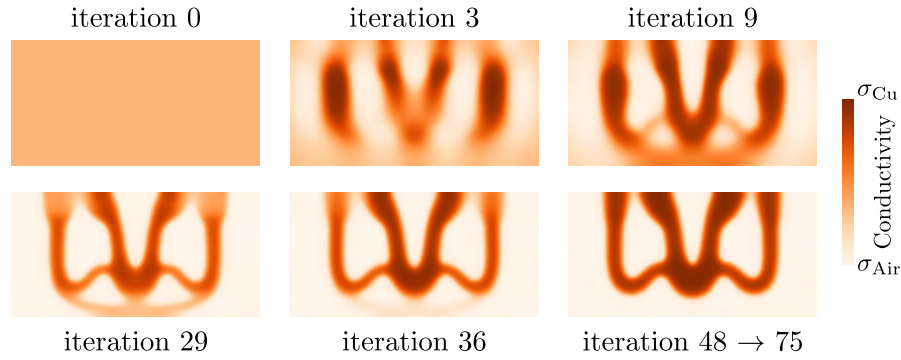


Figure 3.10: Design problem n°4: Evolution of the topology throughout the optimization for maximal Lorentz force along the x -axis.

ignoring the flux density distribution. It is coherent with the fact that the selected objective function is independent of the flux density distribution. On the other hand, if another optimization is performed maximizing the Lorentz force along the positive x -axis (3.15), the optimizer better distributes the material over the design space. Indeed, the different current paths are shaped correctly for force generation along the desired direction. One can quickly verify it by using the *right-hand-rule*. It is observed that the topology does not span over the whole active length (i.e., y -length with non-null magnetic flux density) because this results in a shorter path (i.e., smaller resistance), permitting a large magnitude of current to flow, thus resulting in a larger force. The designed conductor layout splits into multiple tracks to better distribute the electric current through different *active* regions of the imposed magnetic field distribution. This would not have been possible using parametric, shape optimization, or intuitive design without *a-priori* knowledge, which highlights a good strength of the TO method. The evolution of this topology is shown in Fig. 3.10. The optimizer quickly identifies the domain regions where the Lorentz force is maximized along the x -axis when they are filled with conductive material. Then the continuous penalization scheme removes the intermediate materials, which results in the removal of the conductor from some regions but assures fully defined tracks.

Another set of optimizations, maximizing the Lorentz force along the x -axis, is performed to highlight the effect of the volume limitation on the resulting topology. Fig. 3.11 shows that if Vol^* is decreased from $\text{Vol}^* = 0.4$ to $\text{Vol}^* = 0.2$, the external tracks of the original coil are

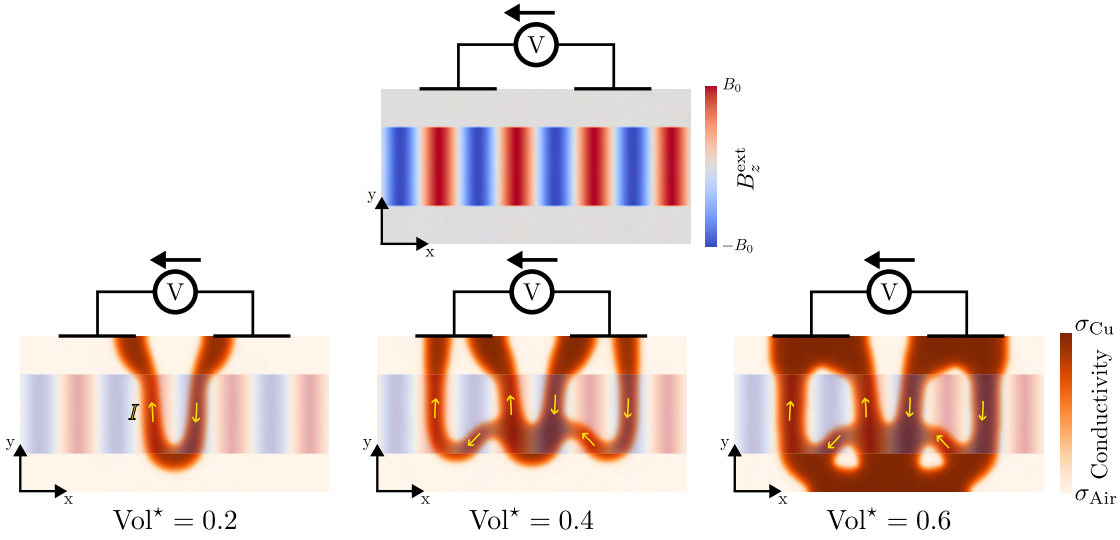


Figure 3.11: Problem n°4: Effect of the volume limitation Vol^* on the topology optimized for maximal Lorentz force along the x -axis.

Table 3.4: Metrics evaluated for the topologies resulting from maximization of the Lorentz force along the x -axis for different volume fractions in the design problem n°4.

Vol^*	ΔV (V)	R (Ω)	I (A)	F_x (mN)	F_y (mN)
0.2	10	3.60	2.77	69.11	-0.08
0.4	10	1.82	5.49	129.57	-0.09
0.6	10	1.27	7.90	168.80	-0.11

removed due to the lower amount of material available. The inner tracks are kept because their shorter lengths (i.e., shorter effective resistance) let flow a larger electric current than in the external ones, resulting thus in a larger relative force. On the other hand, if the volume fraction is increased from $\text{Vol}^* = 0.4$ to $\text{Vol}^* = 0.6$, the tracks stay mostly the same because there is no other region in the flux density distribution that could contribute additionally to the Lorentz force generation. However, the tracks are widened to provide a larger effective cross-section and, thus, a smaller resistance. This results in a larger electric current flow leading to a maximized Lorentz force. It is confirmed by the associated metrics summarized in Table 3.4. As nothing is specified in the optimization regarding the Lorentz force along the y -axis, it is free to vary and take any sign or value. Nevertheless, in this case, maximization of the force along the x -axis results in topology with low contributions to the other axis. It is not a general rule, and explicit minimization of the associated Lorentz force may need to be explicitly added depending on the design problem.

As with any automated design method, the generated topology is highly dependent on the BCs governing the FEA to be solved. Indeed, for the same optimization parameters but different positions of the imposed voltage drop, the generated topologies are very different from

3.1 Topology optimization of conductor tracks in 2-D

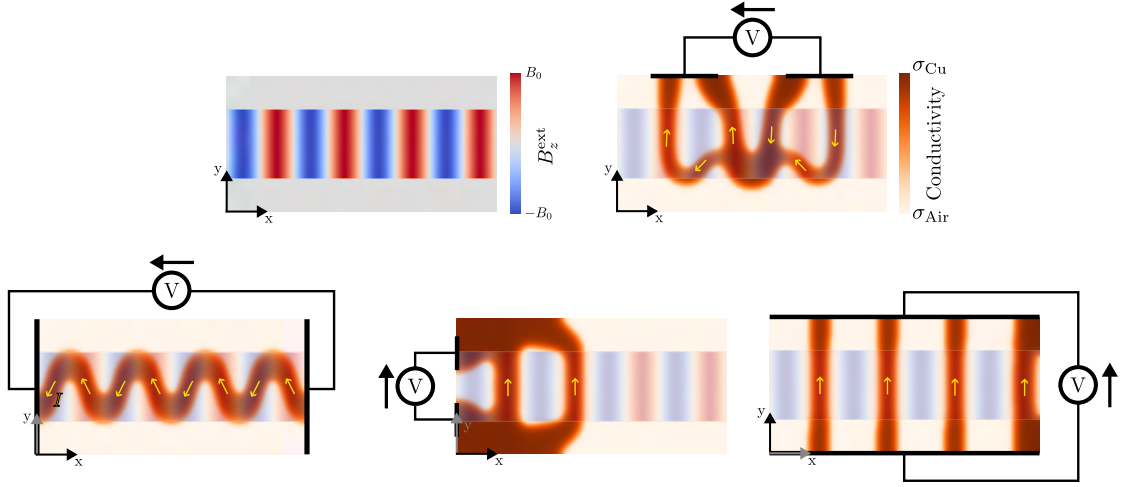


Figure 3.12: Problem n°4: Effect of the boundary conditions positions on the topology optimized for maximal Lorentz force along the x -axis. The volume fraction is fixed to $\text{Vol}^* = 0.4$. The average optimization time is 54 sec per optimization.

Table 3.5: Metrics evaluated for the topologies resulting from maximization of the Lorentz force along the x -axis for different positions for the same boundary condition in the design problem n°4.

Position BC	Vol^*	ΔV (V)	R (Ω)	I (A)	F_x (mN)	F_y (mN)
Top boundary	0.4	10	1.82	5.49	129.57	-0.09
Left-right boundaries	0.4	10	4.38	2.29	94.92	0.20
Left boundary	0.4	10	1.18	8.46	112.08	-0.03
Top-bottom boundaries	0.4	10	0.54	18.44	304.46	-1.30

each other despite having the same other optimization conditions (parameters, objectives, constraints, external field), as shown in Fig. 3.12. These differences in the resulting topologies naturally affect the associated metrics as shown in Table 3.5.

3.1.4 Discussion and conclusion

The problems presented in this chapter only considered voltage sources (Dirichlet BC). This creates a coupling of the flowing electric current with the electrical resistance of the conductor being designed (to keep their product constant following Ohm's law). It means that the generated magnetic flux or the Lorentz force, for example, also depends on the electrical resistance. Such a dependency is not necessarily expected from an electromagnetic standpoint. It is thus essential to always consider and pay attention to the BC constraining and defining the design problem being solved. It is not a problem in the next chapter because only the motor constant is considered as an objective function, removing any coupling with the electric

current. Nevertheless, for other types of problems where control over the absolute magnitude of some metrics is desired, *current sources* should be considered. It is the case for the design problem solved in Section 3.3 where multiple current sources are considered in a 3-D topology optimization problem.

To conclude, this chapter describes the general physics for 2-D electric conduction problems and the generated magnetic field. Different metrics are formulated to evaluate and compare the studied topologies. The general 2-D topology optimization of electric conductors is formulated and applied to multiple study cases, confirming the proposed approach's versatility. Improvements from reference designs and discoveries of solutions to non-trivial design problems are achieved. The developed topology optimization method shows great flexibility in generating better designs.

Publication related to this section:

A. Thabuis, X. Ren, G. Burnand and Y. Perriard, "Density-Based Topology Optimization of Conductor Paths for Windings in Slotted Electrical Machines," 22nd International Conference on Electrical Machines and Systems (ICEMS), 2019, pp. 1-6, doi: 10.1109/ICEMS.2019.8921728, [123].

A. Thabuis, X. Ren, and Y. Perriard, "Automated Design of Conductor Tracks for Electromagnetics," 24th International Conference on the Computation of Electromagnetic Fields (COM-PUMAG), 2023.

(accepted)

3.2 Winding design and 2.5-D topology optimization



INDING design is of interest for advanced electromagnetic devices. The previous section covering the 2-D design of coils is extended to the winding design for electrical machines. A *multi-coil* interpolation scheme is developed for this purpose and demonstrated on 2-D design problems. It is then widened to a so-called *2.5-D formulation* in order to enable the designed coils to overlap in space, resulting in skewed winding types (see Fig. 2.16 [81]). The studied physics are restricted to electric conduction, assuming fixed magnetic flux distributions $B_z^{\text{ext}}(x, y)$ imposed by external sources such as permanent magnets.

3.2.1 Winding design: a multi-coil interpolation scheme

3.2.1.a Formulation

A winding is composed of multiple coils powered by different electrical sources. They can be completely independent or arranged as a multi-phase system, such as the common three-phased network, which is considered here. In a completely symmetric system, the different phases or groups of coils should be electrically and magnetically balanced. The most straightforward enforcement of such equilibrium is to have the coils constituting the phases with an identical topology. It allows the restriction of the winding design to the design of a single coil. However, as the topology is unknown beforehand, the design space can not be split accordingly. This requires accounting for the packing with the other coils while designing the main one.

We propose to create *virtual* copies of the topology being designed, corresponding to the other coils constituting the winding. The way these copies are spatially distributed inside the design space depends on the application. Here, the analysis is restrained to a case with three phases and a single pole-pair. The resulting winding could be extended periodically to account for more pole pairs. The total number of coils N_c is either equal to one or two times the number of phases (i.e., 3 or 6). Assuming a magnetic pole-pair covering a length L_x^{PP} along the x -axis, the coils are spaced by $\Delta_{\text{coil}} = \frac{L_x^{\text{PP}}}{N_c}$. In the rest of this chapter, the magnetic pole-pair span over the x -axis (L_x^{PP}) is considered equal to the design domain length over the x -axis (l_x), but this is not a requirement. The principle previously described is illustrated in Fig. 3.13 for $N_c = 3$ and $L_x^{\text{PP}} = l_x$ the length of the design space along the x -axis. The topology representing the main coil being designed is shown inside the design domain in Fig. 3.13.a. Then the first virtual copy is created, resulting in a periodic distribution shifted by Δ_{coil} from the main coil as shown in Fig. 3.13.b. The same operation is repeated for the second virtual copy. When restraining the distributed coils (main one and copies) to the design domain, one obtains Fig. 3.13.d. However, depending on the shape of the main coil, the distribution of the shifted copies may result in regions where they mix. It is an undesired behavior that should be prevented to ensure proper winding operation. Indeed, this would result in short-circuited phases, affecting the current path and possibly damaging the machine. Thus, these regions should be removed from the winding as shown in Fig. 3.13.f defining a *winding-field*. The conductivity distribution representing the coil being designed should then combine the initial distribution (Fig. 3.13.a) and the winding field (Fig. 3.13.f) to account for proper packing of the

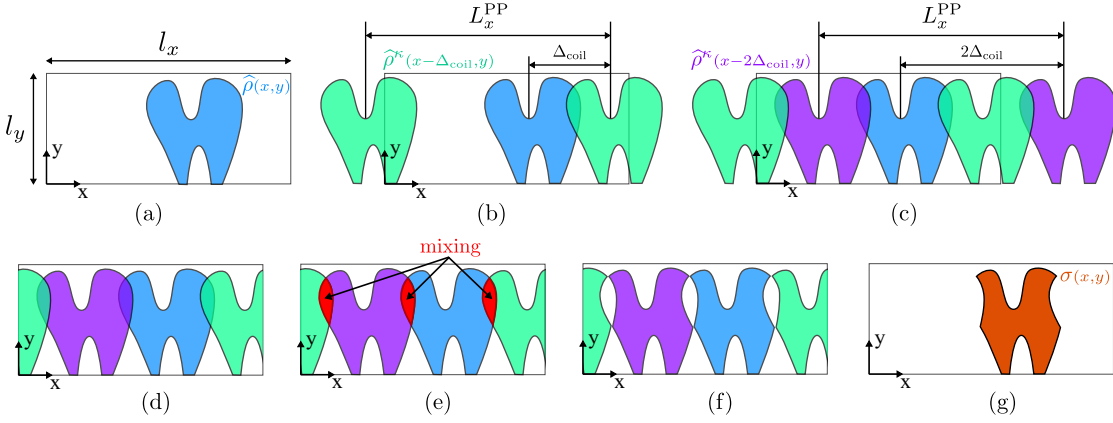


Figure 3.13: Winding design principle: (a) Random topology for example, (b) first virtual periodic copy, (c) second virtual periodic copy, (d) all coils restrained to the design domain, (e) highlighting of the regions with mixing coils, (f) winding field composed of coils without mixing, and (g) resulting conductivity distribution restrained to the initial topology with penalized mixing regions within the winding-field.

multiple coils constituting the winding as shown in Fig. 3.13.g. The mathematical description of the proposed idea is described below. First, periodicity over the magnetic pole-pair span is formulated for the projected topology:

$$\hat{\rho}^\kappa = \hat{\rho}^\kappa(x, y) = \hat{\rho}(x - \kappa \cdot L_x^{PP}, y) \quad \text{with } \kappa \in \mathbb{Z}. \quad (3.29)$$

Then, the virtual copies (with periodicity) are written as:

$$\hat{\rho}^\kappa(x - j \cdot \Delta_{coil}, y) \quad \text{with } j \in \{1, \dots, N_c - 1\}. \quad (3.30)$$

They can be arranged with the original distribution inside a list of coils :

$$\hat{\rho}^{\text{v-copies}} = [\hat{\rho}^\kappa(x, y), \hat{\rho}^\kappa(x - \Delta_{coil}, y), \dots, \hat{\rho}^\kappa(x - (N_c - 1)\Delta_{coil}, y)]. \quad (3.31)$$

Mixing between the designed topology and its virtual copies should be prevented everywhere inside the design space. This can be formulated as a constraint at each (x_i, y_i) position of the i -vertex in the mesh:

$$\hat{\rho}^\kappa(x_i, y_i) + \hat{\rho}^\kappa(x_i - \Delta_{coil}, y_i) + \dots + \hat{\rho}^\kappa(x_i - (N_c - 1)\Delta_{coil}, y_i) \leq 1. \quad (3.32)$$

Thus, for a design domain discretized into N vertices, N associated constraints should be formulated. Such a method would increase the computational time tremendously. Global measures like the p -norm or the Kresselmeier–Steinhauser function [124] could include all the local constraints into a single one. However, the strict prohibition still greatly restricts the optimization problem, which should be avoided with local-search optimizers. That is why we propose to lighten this restriction by enforcing such a constraint implicitly in a penalization scheme³. This is achieved by first creating a *winding-field* χ containing the topology being

³Similarly to the penalization of the intermediate materials commonly done by the SIMP or RAMP schemes in topology optimization.

designed and its virtual copies but penalized whenever one distribution is mixing with another (similar to Fig. 3.13.f). We propose a *multi-coil* interpolation scheme⁴ $h_{\text{Multi-Coil}}$ to describe it:

$$\chi = \chi(x, y) = h_{\text{Multi-Coil}}(\hat{\rho}) = \sum_{j=0}^{N_c-1} \hat{\rho}^K(x - j \cdot \Delta_{\text{coil}}, y) \prod_{\substack{k=0 \\ k \neq j}}^{N_c-1} (1 - \hat{\rho}^K(x - k \cdot \Delta_{\text{coil}}, y)). \quad (3.33)$$

One can observe that this field will be equal to 0 wherever two copies are mixing (equal to one at the same position) or where no copies are present; and to 1 wherever only one copy is present. The material properties are then obtained using the RAMP interpolation scheme from (3.20) weighted by this *winding*-field, resulting in the function $h_{\alpha\text{-RAMP}}$:

$$\sigma = \sigma(x, y) = h_{\alpha\text{-RAMP}}(\hat{\rho}, \chi) = \sigma_{\text{Air}} + (\sigma_{\text{Cu}} - \sigma_{\text{Air}}) \left(\frac{\hat{\rho}}{1 + q(1 - \hat{\rho})} \chi \right), \quad (3.34)$$

To summarize the method for winding design in 2-D, the original formulation (Fig. 3.4) describing the steps linking the control variables to the material properties used for the FEA is thus modified as follows:

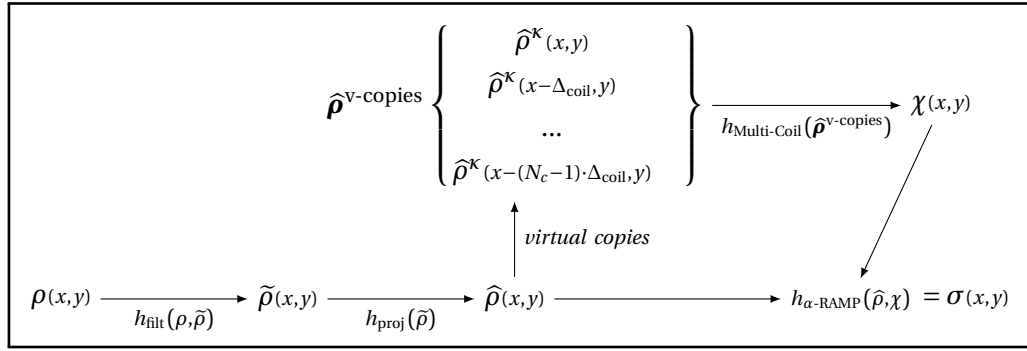


Figure 3.14: Flowchart of the 2-D topology optimization of conductors for winding design.

3.2.1.b Results with 2-D topology optimization

A fifth design problem is formulated to study the proposed winding design method. It considers the following magnetic flux density distribution, corresponding to a slice of an air-gap placed between two permanent magnet arrays (similar to Fig. 3.2):

$$B_z(x, y) = B_0 \cdot \sin\left(\frac{2\pi}{L_x^{\text{PP}}} \cdot x\right) \cdot \left(\frac{B_0}{2} - \frac{1}{\pi} \cdot \arctan\left(5 \cdot \sin\left(\frac{2\pi(y - L_y^{\text{PP}}/2)}{2L_y^{\text{PP}}}\right)\right)\right). \quad (3.35)$$

The considered design domain Ω has a size of $l_x \times l_y = 64\text{mm} \times 29\text{mm}$, representing the upper half of the total space. It is discretized uniformly by 40'000 triangular elements, resulting in 20'301 DOFs of the control variables distribution. The magnetic pole pair span is $L_x^{\text{PP}} = 64$ mm, with a height of $L_y^{\text{PP}} = 40$ mm. The voltage source of $\Delta V = 10V$ is applied over the bottom boundary of the design domain, corresponding to the symmetry axis. This allows having a final

⁴The sensitivity associated with the step creating the virtual copies is simply the original sensitivity with its DOFs mapped according to the spatial shift performed.

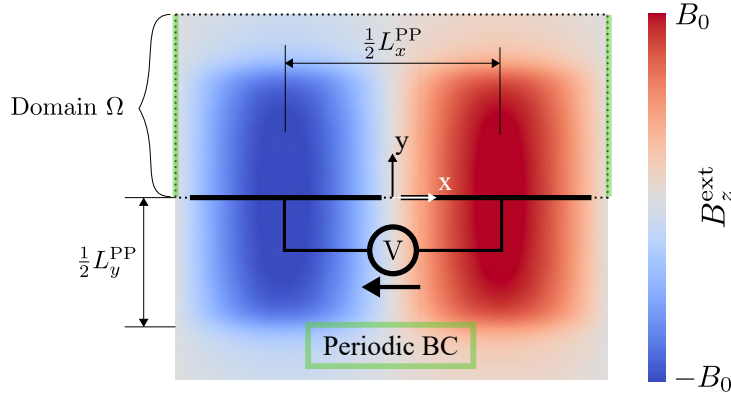


Figure 3.15: Design problem n°5: single magnetic pole-pair considering symmetry. Description of the considered magnetic flux distribution and the boundary conditions of the electric conduction problem. The top rectangle marked by the dotted line corresponds to the design domain Ω .

topology relatively independent from the position of the BC (as discussed in Section 3.1.3.b) and to harvest symmetry reducing the computational cost. Periodicity across the x -axis is considered in the electric conduction problem by mapping the DOFs of the electric potential distribution from the right boundary to the left one. Fig. 3.15 presents the design problem with the corresponding boundary conditions and the considered flux density distribution described in (3.35).

The optimization is run considering a winding made of $N_c = 3$ coils, maximizing the motor constant along the positive x -axis. The filter radius is set to $r_{\text{filt}} = 1.6 \times 10^{-3}$, and the penalty factor from the RAMP scheme is continuously increased every 25 iterations with the following values $\{0, 4, 8\}$. The mirrored conductivity distribution of the resulting topology is shown in Fig. 3.16. Considering the BC and magnetic flux distribution shown in Fig. 3.15, it is observed that the force is generated along the desired direction using the right-hand rule. The associated *winding-field* χ shown in Fig. 3.16 exhibit no mixing of the coil with its virtual copies, validating the effectiveness of the proposed *multi-coil* interpolation scheme. Furthermore,

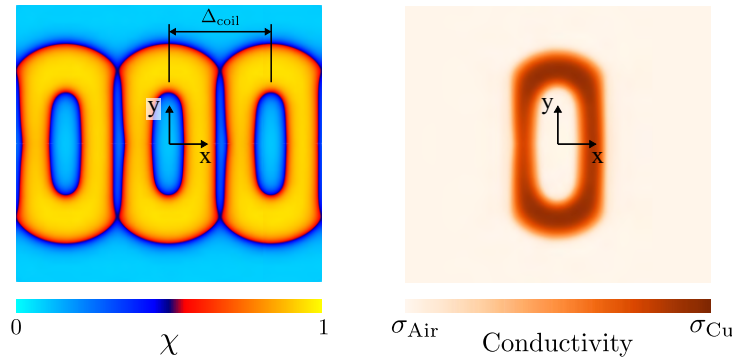


Figure 3.16: Results of the design problem n°5 with the 2-D formulation: winding field χ with the conductivity distribution. Optimization time: 117 sec.

the optimization took only 117 sec to finish, which would not have been possible with explicit constraints instead of the proposed scheme. However, one can observe that the resulting topology corresponds to a simple concentric coil that lacks novelty and could have been determined manually. It is because the design space is limited to a 2-D plane, preventing the different coils constituting the winding from overlapping outside the plane. The design space congested by the virtual copies prevents novel performing geometries and results in a simple concentric shape.

3.2.2 2.5-D topology optimization for overlapping winding design

There is a need for more design freedom in the developed framework to allow the different coils constituting the winding to overlap outside the plane. This aims at designing *overlapping* (or *skewed* [81, 62]) winding types. A 3-D topology optimization could permit such behavior but would significantly increase computational time, which is not desired here. Thus, a so-called *2.5-D formulation* is proposed here to tackle this limitation and find novel winding geometries while keeping a reasonable computational time.

3.2.2.a Formulation

The main idea behind the proposed 2.5-D formulation is to use two different 2-D distributions of artificial densities $\rho_{l0} = \rho_{l0}(x, y)$, and $\rho_{l1} = \rho_{l1}(x, y)$. They represent two different layers 0 and 1, respectively, one on top of the other. The FEA is still performed in 2-D by projecting the two distributions onto a single plane to form the electrical conductivity distribution. The z -component of the flowing current is considered small enough compared to the x - and y -components. Nevertheless, the regions where the two layers overlap still require special

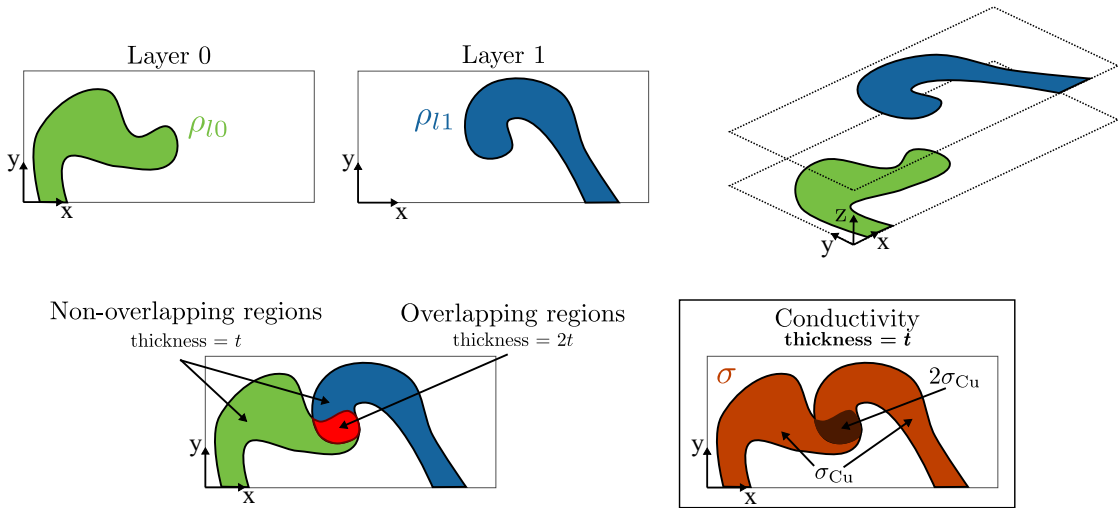


Figure 3.17: Principle of the 2.5-D formulation with dummy topologies in layers 0 and 1. The overlapping regions have an effective thickness two times larger than the non-overlapping ones. This is interpreted as a single conductivity distribution with constant thickness but two times the conductivity of non-overlapping regions inside the overlapping ones.

attention. Indeed, in a physical coil, each layer has a constant thickness t , but the overlapping regions should have two times the same thickness $2t$. However, a 2-D FEA considers a constant thickness for the whole design domain. We propose to artificially compensate for the difference in thickness by considering these overlapping regions with an electrical conductivity two times the one of non-overlapping regions (σ_{Cu}). It is illustrated in Fig. 3.17. A strength of the proposed formulation is that it keeps the same computational cost associated with the FEA as in the 2-D topology optimization. The design of overlapping winding is achieved while only doubling the number of control variables, removing the need for 3-D topology optimization that would have required much more design variables and increased the cost of the FEA significantly.

The mathematical formulation of the proposed method is described next. The artificial density distributions of each layer are filtered and projected similarly to the 2-D formulation, resulting in $\hat{\rho}_{l0} = \hat{\rho}_{l0}(x, y)$, and $\hat{\rho}_{l1} = \hat{\rho}_{l1}(x, y)$. The material properties are obtained by extending the RAMP scheme from (3.20) to account for the two layers⁵ resulting in the function $h_{\text{RAMP-2}}$:

$$\sigma = \sigma(x, y) = h_{\text{RAMP-2}}(\hat{\rho}_{l0}, \hat{\rho}_{l1}) = \sigma_{\text{Air}} + (\sigma_{\text{Cu}} - \sigma_{\text{Air}}) \left(\frac{\hat{\rho}_{l0}}{1 + q(1 - \hat{\rho}_{l0})} + \frac{\hat{\rho}_{l1}}{1 + q(1 - \hat{\rho}_{l1})} \right). \quad (3.36)$$

However, such a description does not account for a proper winding design made of multiple coils. The approach defined in the previous section (Section 3.2.1) can thus be extended to the 2.5-D formulation enforcing the desired behavior. First, the periodic projected distributions are defined similarly to (3.29):

$$\begin{aligned} \hat{\rho}_{l0}^{\kappa} &= \hat{\rho}_{l0}(x - \kappa \cdot L_x^{\text{PP}}, y) \quad \text{with } \kappa \in \mathbb{Z}, \\ \hat{\rho}_{l1}^{\kappa} &= \hat{\rho}_{l1}(x - \kappa \cdot L_x^{\text{PP}}, y) \quad \text{with } \kappa \in \mathbb{Z}, \end{aligned} \quad (3.37)$$

leading to the two lists of coils and virtual copies in each layer:

$$\begin{aligned} \hat{\rho}_{l0}^{\text{v-copies}} &= [\hat{\rho}_{l0}^{\kappa}(x, y), \hat{\rho}_{l0}^{\kappa}(x - \Delta_{\text{coil}}, y), \dots, \hat{\rho}_{l0}^{\kappa}(x - (N_c - 1)\Delta_{\text{coil}}, y)], \\ \hat{\rho}_{l1}^{\text{v-copies}} &= [\hat{\rho}_{l1}^{\kappa}(x, y), \hat{\rho}_{l1}^{\kappa}(x - \Delta_{\text{coil}}, y), \dots, \hat{\rho}_{l1}^{\kappa}(x - (N_c - 1)\Delta_{\text{coil}}, y)]. \end{aligned} \quad (3.38)$$

Then, the *winding*-fields in each layer are derived using the *multi-coil* interpolation scheme from (3.33):

$$\begin{aligned} \chi_{l0} &= \chi_{l0}(x, y) = h_{\text{Multi-Coil}}(\hat{\rho}_{l0}) = \sum_{j=0}^{N_c-1} \hat{\rho}_{l0}^{\kappa}(x - j \cdot \Delta_{\text{coil}}, y) \prod_{\substack{k=0 \\ k \neq j}}^{N_c-1} (1 - \hat{\rho}_{l0}^{\kappa}(x - k \cdot \Delta_{\text{coil}}, y)), \\ \chi_{l1} &= \chi_{l1}(x, y) = h_{\text{Multi-Coil}}(\hat{\rho}_{l1}) = \sum_{j=0}^{N_c-1} \hat{\rho}_{l1}^{\kappa}(x - j \cdot \Delta_{\text{coil}}, y) \prod_{\substack{k=0 \\ k \neq j}}^{N_c-1} (1 - \hat{\rho}_{l1}^{\kappa}(x - k \cdot \Delta_{\text{coil}}, y)). \end{aligned} \quad (3.39)$$

By combining (3.34) with (3.36) and the *winding*-fields in each layer (3.39), a new MIS

⁵Mixing between the layers is permitted here over the entire design space. Nevertheless, control over the regions where the "doubled" thickness (i.e., mixing of layers) is permitted could be achieved with a modified MIS.

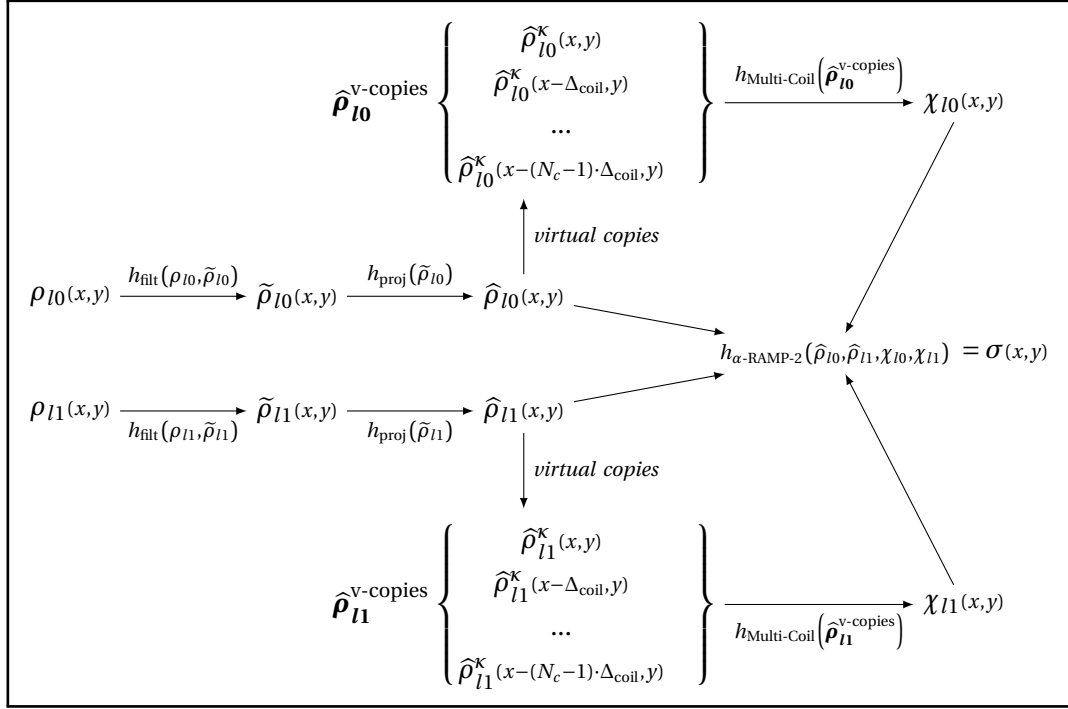


Figure 3.18: Flowchart of the 2.5-D topology optimization of conductors for overlapping winding design.

($h_{\alpha\text{-RAMP-2}}$) is proposed to project the two different layers into a single plane:

$$\begin{aligned} \sigma = \sigma(x,y) &= h_{\alpha\text{-RAMP-2}}(\hat{\rho}_{l0}, \hat{\rho}_{l1}, \chi_{l0}, \chi_{l1}) \\ &= \sigma_{\text{Air}} + (\sigma_{\text{Cu}} - \sigma_{\text{Air}}) \left(\frac{\hat{\rho}_{l0}}{1 + q(1 - \hat{\rho}_{l0})} \chi_{l0} + \frac{\hat{\rho}_{l1}}{1 + q(1 - \hat{\rho}_{l1})} \chi_{l1} \right). \end{aligned} \quad (3.40)$$

The flowchart from Fig. 3.14 describing the steps linking the control variables to the material properties used for the FEA is extended to 2.5-D and shown in Fig. 3.18.

3.2.2.b Results with 2.5-D topology optimization

The same design problem as in the previous section with a single magnetic pole-pair and symmetric BC is considered (problem n°5 shown in Fig. 3.15). As more freedom is provided with the 2.5-D formulation, the number of coils constituting the winding increases to $N_c = 6$, resulting in 2 coils per phase inside the three-phase electric motor. The shift between virtual copies is thus $\Delta_{\text{coil}} = L_x^{\text{PP}}/6$. The design domain is still discretized into 40'000 uniform triangles, resulting in 40'602 DOFs of control variables (due to the two layers). The two distributions of artificial density are uniformly initialized to $1/N_c = 0.1\bar{6}$. The volume fraction limitation is still put on the average control variable value (containing the two layers):

$$g_{\text{vol}}(\rho_{l0}, \rho_{l1}) = \frac{\iint_{\Omega} \frac{\rho_{l0}(x,y) + \rho_{l1}(x,y)}{2} d\Omega}{\iint_{\Omega} 1 d\Omega} \leq \text{Vol}^* = \frac{2}{N_c}. \quad (3.41)$$

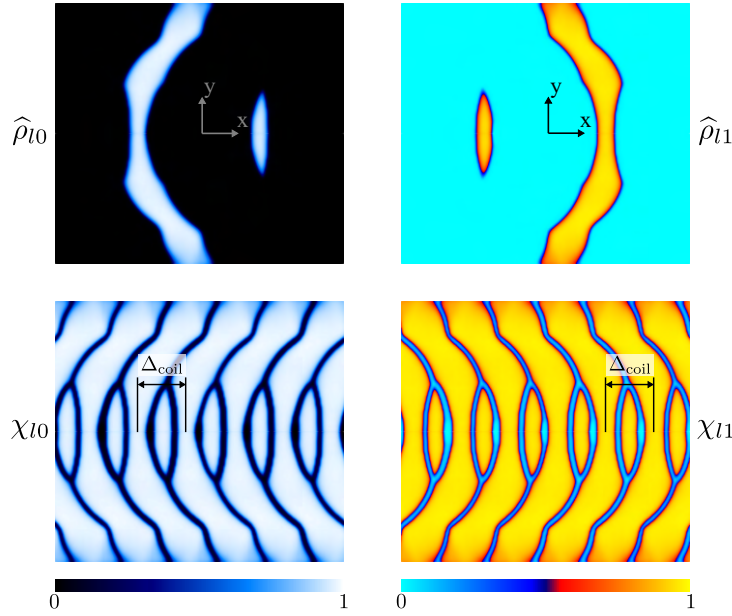


Figure 3.19: Results of the design problem n°5 with the 2.5-D formulation: projected material distribution (top) in layer 0: $\hat{\rho}_{l0}$ (left) and in layer 1: $\hat{\rho}_{l1}$ (right), with the corresponding *winding-fields* χ_{l0} and χ_{l1} (bottom) made of the shifted virtual copies. Optimization time: 210 sec.

Two different inequality constraints could have been formulated to explicitly limit the volume fraction within each layer instead of the average value. However, due to the *multi-coil* interpolation scheme, the design space is already indirectly restrained to the limited volume fraction caused by the presence of the virtual copies, removing the need for additional constraints. The optimization is run maximizing the motor constant⁶ (3.16). The filter radius set to $r_{\text{filt}} = 0.45 \times 10^{-3}$, and the penalty factor continuously increased every 25 iterations with the values $\{0, 4, 8\}$. The resulting projected distribution in each layer is shown at the top part of Fig. 3.19. The corresponding *winding-fields* are shown at the bottom. One can observe the great packing of the different coils constituting the winding. The projection of the two layers onto a single plane is illustrated in the left part of Fig. 3.20 with the overlapping regions highlighted in red. The corresponding electrical conductivity is shown next to it. One can observe that the non-overlapping regions have a conductivity equal to σ_{Cu} , while the overlapping ones have it doubled $2\sigma_{\text{Cu}}$ compensating for the doubled thickness of these regions. The total optimization time took only 210 sec, confirming the proposed method's great efficiency. A 3-D topology optimization would have been much longer (several orders of magnitude as shown in Section 3.3). The generated topology has been modeled in 3-D to form the physical coil (without turn modeling). The linear and rotating machine versions are shown in Fig. 3.21.

⁶The computed motor constant is associated with the properties of a single coil and not the whole winding as provided in electric motors datasheet.

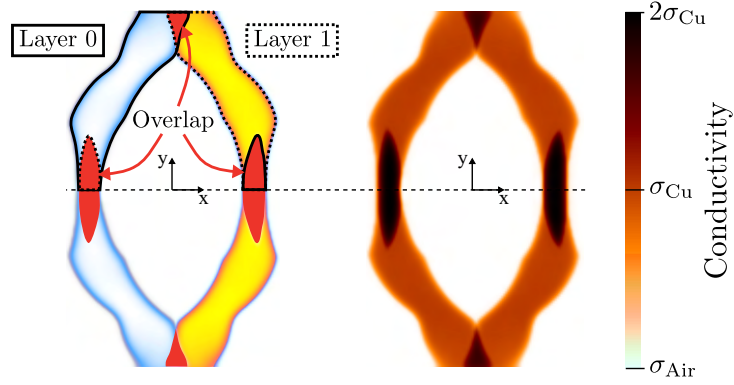


Figure 3.20: Results of the design problem n°5 with the 2.5-D formulation: material distribution resulting from the topology optimization. The distributions have been mirrored to obtain the full geometry. The doubled copper conductivity $2\sigma_{Cu}$ represents the regions where the two layers overlap.

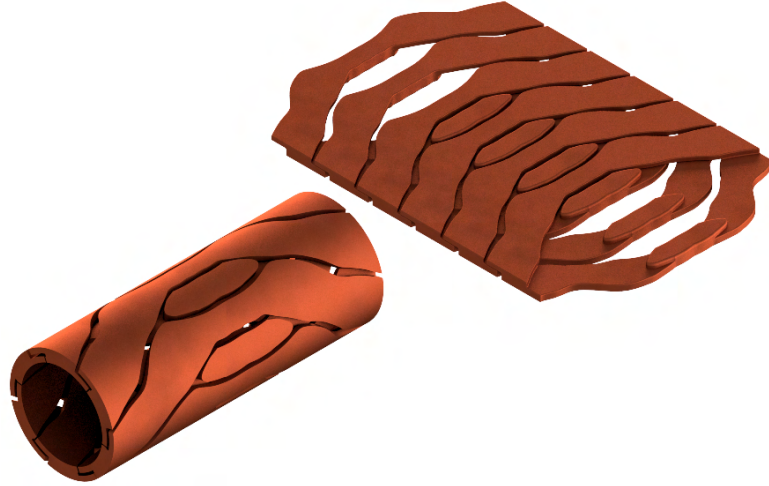


Figure 3.21: Reconstructed windings for linear and rotating motors.

3.2.3 Discussion on the novel topology

A *rhombus* and *diamond* geometries with constant cross-sections commonly used in overlapping windings are used as references to evaluate the performance of the generated new topology. They both have been designed with $N_c = 6$ coils so as to fit the design space while maximizing the motor constant. They are shown in Fig. 3.22 with the associated metrics in Table 3.6. By nature, the *rhombus* geometry has a small resistance due to its short effective conductor length and wide cross-section. However, this impacts the contribution to the force generation as only a portion of the current contributes to it (y -component). On the other hand, the *diamond* geometry offers a better force constant due to its straight vertical segments that better contribute to it. The motor constant is directly proportional to the force constant while being inversely proportional to the squared root of the resistance. Thus, despite having a larger electric resistance, the *diamond* coil still achieves a motor constant similar to the one of the *rhombus*. The coil generated by the developed computational design framework exhibits

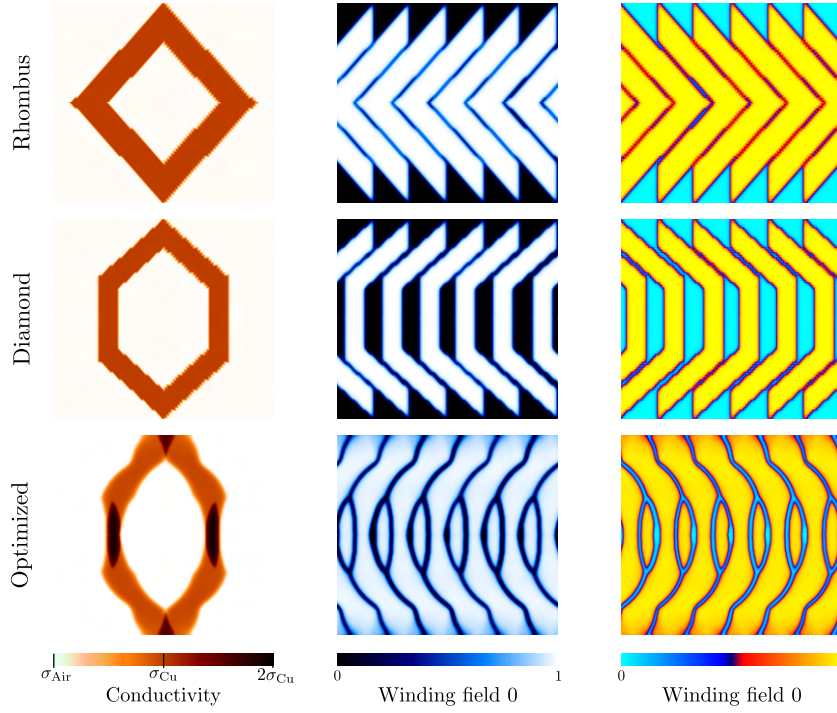


Figure 3.22: Problem n°5: Comparison of the 2.5-D topology optimized winding with two different reference ones.

Table 3.6: Metrics evaluated for the 2.5-D topology optimized winding for problem n°5, and the reference topologies.

	ΔV (V)	R (Ω)	F_x (mN)	k_F (mN/A)	k_m (mN/ \sqrt{W})
Rhombus	10.0	1.48	122.5	18.1	14.9
Diamond	10.0	2.46	95.5	23.5	15.0
Optimized	10.0	2.17	117.5	25.5	17.5

large force generation due to the significant contribution from its straight segments similar to the *diamond* coil. It also shows smaller resistance due to its non-constant cross-section resulting in better packing with the other coils and the doubled thickness in the overlapping regions. Spatially, the doubled thickness on the straight segments of the coil is permitted by having a coil pitch smaller than the magnetic pole-pair pitch. The design space is thus not congested with the second coil of the same phase. In this fashion, the optimized coil can achieve a motor constant +17.5% larger than the *rhombus* coil and +16.7% larger than the *diamond* coil.

These results and improvements assume single conductor representation without any turn modeled and without the usage of homogenization methods. This means that, in practice, the current density distribution is slightly different. Integrating such modeling could provide a

more advanced way to generate novel winding with improved performance. It is proposed as future work for this thesis. Nonetheless, the generated topology also corresponds to a local optimum due to the nature of the used optimizer. Thus, further improvement is expected if the topology is parametrized by a few geometric parameters and then further optimized with global-search methods.

3.2.4 Conclusion

The developed framework shows great promise for the automated design of high-performance electrical machines. The proposed topology optimization formulation can achieve a winding design with overlapping coils made of conductors with a non-constant cross-section. The varying width and thickness of the designed tracks permit novel coil geometries that conventional design methods could not determine.

Publication related to this section:

A. Thabuis, X. Ren and Y. Perriard, "Topology Optimization of Motor Windings for Coreless Electrical Machines," 2023 (*submitted to IEEE Access and available on TechRxiv. doi: 10.36227/techrxiv.22666105* [125])

3.3 Asymmetric winding design in 3-D topology optimization



ASYMMETRIC cases have been considered for now, with a winding design restricted to the design of a single coil. It works for windings made of coils achieving a common task and where geometric transformations are sufficient to reconstruct the winding. The automated design method needs to be modified when there is an *asymmetric* operation between the different coils. This section presents this and demonstrates it through a 3-D topology optimization problem.

3.3.1 Formulation

3.3.1.a Physics

The study case presented in Section 3.3.2 requires three types of coils, one associated with each axis of the Cartesian coordinate system. They are defined as the \mathcal{X} -coils, the \mathcal{Y} -coils, and the \mathcal{Z} -coils. They are described by their electrical conductivity distributions in the 3-D design space: $\sigma^i = \sigma^i(x, y, z)$ with $i = \mathcal{X}, \mathcal{Y}$, or \mathcal{Z} depending on the considered coils. Each set of coils is considered powered by a different current and is thus individually studied to compute the physics. Similarly to Section 3.1.1, static and linear electromagnetic analyses are performed. The following equations describe the different electric conduction problems associated with each coil:

$$\begin{aligned} -\nabla \cdot \left(\sigma^{\mathcal{X}}(x, y, z) \nabla U^{\mathcal{X}}(x, y, z) \right) &= 0, \\ -\nabla \cdot \left(\sigma^{\mathcal{Y}}(x, y, z) \nabla U^{\mathcal{Y}}(x, y, z) \right) &= 0, \\ -\nabla \cdot \left(\sigma^{\mathcal{Z}}(x, y, z) \nabla U^{\mathcal{Z}}(x, y, z) \right) &= 0. \end{aligned} \quad (3.42)$$

They are solved individually considering different current sources enforced through multiple BCs. This is referred to as different LCs for the design problem. As shown later, the developed framework is implemented in the commercial FEA software COMSOL[®] [126], which automatically implements the weak form. Nevertheless, the derivation of the variational problem associated with one current source is provided in the appendix A for interested readers. The associated electric current densities are computed as $\mathbf{J}^i(x, y, z) = -\sigma^i(x, y, z) \nabla U^i(x, y, z)$ with $i = \mathcal{X}, \mathcal{Y}$, or \mathcal{Z} . These flowing currents generate independent magnetic fields described by Ampere's law (similarly to (3.6)):

$$\begin{aligned} \nabla \times \mathbf{H}^{\mathcal{X}}(x, y, z) &= \mathbf{J}^{\mathcal{X}}(x, y, z), \\ \nabla \times \mathbf{H}^{\mathcal{Y}}(x, y, z) &= \mathbf{J}^{\mathcal{Y}}(x, y, z), \\ \nabla \times \mathbf{H}^{\mathcal{Z}}(x, y, z) &= \mathbf{J}^{\mathcal{Z}}(x, y, z), \end{aligned} \quad (3.43)$$

with $\mathbf{H}^i(x, y, z)$ the magnetic field distribution generated by the i -coils. The associated magnetic flux density distributions are derived such that $\mathbf{B}^i(x, y, z) = (B_x^i(x, y, z), B_y^i(x, y, z), B_z^i(x, y, z)) = \mu_0 \mathbf{H}^i(x, y, z)$. In this example, no ferromagnetic materials are considered. The magnetic permeability of the different materials (air and copper) is assumed equal to the vacuum magnetic permeability μ_0 .

3.3.1.b Topology description

This chapter permits different geometries for the different coils to explore a larger solution space. Similarly to (3.17), their topologies are described by *artificial* density distributions: $\rho^{\mathcal{X}}$, $\rho^{\mathcal{Y}}$, and $\rho^{\mathcal{Z}}$ for the \mathcal{X} -, \mathcal{Y} -, and \mathcal{Z} -coil respectively:

$$\rho^{\mathcal{X}} = \rho^{\mathcal{X}}(x, y, z) \quad ; \quad \rho^{\mathcal{Y}} = \rho^{\mathcal{Y}}(x, y, z) \quad ; \quad \rho^{\mathcal{Z}} = \rho^{\mathcal{Z}}(x, y, z) \quad \in]0, 1]. \quad (3.44)$$

These distributions defined in the 3-D space correspond to the control variables of the optimization problem. They are filtered and projected using the functions described by (3.18) and (3.19), resulting in the following projected distributions: $\hat{\rho}^{\mathcal{X}} = \hat{\rho}^{\mathcal{X}}(x, y, z)$, $\hat{\rho}^{\mathcal{Y}} = \hat{\rho}^{\mathcal{Y}}(x, y, z)$, and $\hat{\rho}^{\mathcal{Z}} = \hat{\rho}^{\mathcal{Z}}(x, y, z)$. A *multi-coil* interpolation scheme is formulated to prevent the mixing of the different coils like in Section 3.2.1. The same idea to penalize the regions with mixing coils resulting in lower electrical conductivity is harvested here. Due to some limitations in the implementation of the topology optimization within the COMSOL[®] software, it is applied to the penalized projected variables and not to the projected variables directly. In practice, this does not change the fundamental principle but performs the penalization in another order. One could, in future work, study the effect of such order for different penalization schemes (intermediate material penalization versus coil mixing penalization). The implemented scheme combines another popular MIS: the SIMP [26, eq. 4] approach (with q the penalty factor), with the *winding*-field from (3.33). It is formulated with the following functions:

$$\begin{aligned} \sigma^{\mathcal{X}} &= \sigma^{\mathcal{X}}(x, y, z) = h_{\text{SIMP:Multi-Coil:}\mathcal{X}}(\hat{\rho}^{\mathcal{X}}, \hat{\rho}^{\mathcal{Y}}, \hat{\rho}^{\mathcal{Z}}) \\ &= \sigma_{\text{Air}} + (\sigma_{\text{Cu}} - \sigma_{\text{Air}}) \left[\left(\hat{\rho}^{\mathcal{X}} \right)^q \cdot \left(1 - \left(\hat{\rho}^{\mathcal{Y}} \right)^q \right) \cdot \left(1 - \left(\hat{\rho}^{\mathcal{Z}} \right)^q \right) \right], \\ \sigma^{\mathcal{Y}} &= \sigma^{\mathcal{Y}}(x, y, z) = h_{\text{SIMP:Multi-Coil:}\mathcal{Y}}(\hat{\rho}^{\mathcal{X}}, \hat{\rho}^{\mathcal{Y}}, \hat{\rho}^{\mathcal{Z}}) \\ &= \sigma_{\text{Air}} + (\sigma_{\text{Cu}} - \sigma_{\text{Air}}) \left[\left(\hat{\rho}^{\mathcal{Y}} \right)^q \cdot \left(1 - \left(\hat{\rho}^{\mathcal{X}} \right)^q \right) \cdot \left(1 - \left(\hat{\rho}^{\mathcal{Z}} \right)^q \right) \right], \\ \sigma^{\mathcal{Z}} &= \sigma^{\mathcal{Z}}(x, y, z) = h_{\text{SIMP:Multi-Coil:}\mathcal{Z}}(\hat{\rho}^{\mathcal{X}}, \hat{\rho}^{\mathcal{Y}}, \hat{\rho}^{\mathcal{Z}}) \\ &= \sigma_{\text{Air}} + (\sigma_{\text{Cu}} - \sigma_{\text{Air}}) \left[\left(\hat{\rho}^{\mathcal{Z}} \right)^q \cdot \left(1 - \left(\hat{\rho}^{\mathcal{X}} \right)^q \right) \cdot \left(1 - \left(\hat{\rho}^{\mathcal{Y}} \right)^q \right) \right]. \end{aligned} \quad (3.45)$$

One can observe that the resulting conductivity σ^i is equal to σ_{Air} wherever two (or more) coil types are mixing ($\hat{\rho}^i = \hat{\rho}^j = 1$) or where no coil is present; and to σ_{Cu} wherever only one coil type is present.

The flowchart describing the steps linking the control variables to the material properties used for the different FEAs is shown in Fig. 3.23.

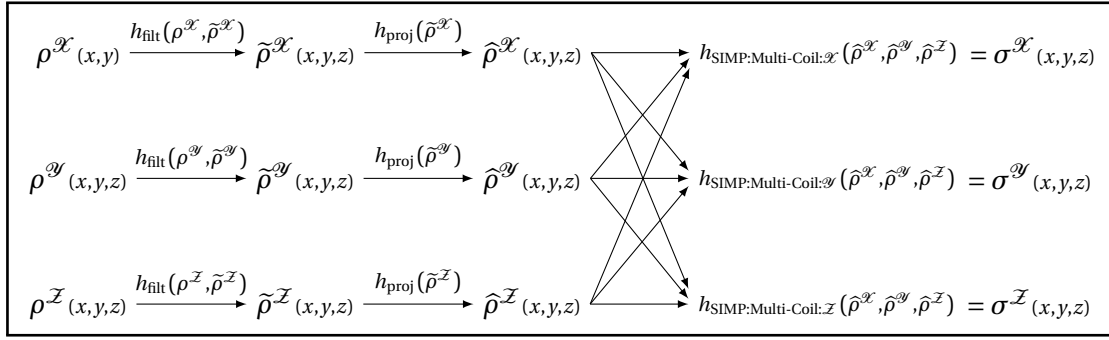


Figure 3.23: Flowchart of the 3-D topology optimization of coils for asymmetric winding.

3.3.2 Design problem: a 3-D electromagnet manipulator

3.3.2.a Description

Magnetic manipulation is used to manipulate objects in a contactless manner. It is a well-spread method in biomedical applications to operate within the body for drug delivery using micro-robots, for example, [127, 128]. The most common device used for magnetic manipulation is the pair of Helmholtz coils. It consists of two identical circular coils aligned with their main axis and placed at a distance equal to their common radius from each other. This specific sizing assures the production of a nearly uniform magnetic field between the two coils when traveling by the same electric current. The region in the center, where the uniform field is desired, is defined as the Region Of Interest (ROI). Topology optimization for better uniform magnetic flux generation for a single pair of Helmholtz coils has been performed during this thesis. Its implementation is not further discussed here because it is similar to state-of-the-art methods from different applications [65, 67]. However, interested readers are invited to browse the corresponding publication [129].

When control over the three axes is desired, an assembly of three nested Helmholtz pairs is required [130]. Each pair is aligned with a different axis of the Cartesian coordinate system. The additional pairs are usually scaled up with a larger radius and thus a larger distance between their two coils to prevent collisions with the other pairs (as shown in Fig. 3.24a). The number of turns of the associated coils needs to be increased in order to achieve a magnetic field magnitude similar to the one generated by the smaller coils (because the current magnitude is kept the same for each set of coils). This scaling in size and number of turns has several consequences. First, the resistance and, thus, the losses between the pairs change, creating uneven heat distribution, which restricts the maximal input current value (and thus the achievable magnetic field magnitude) to the pair that will heat the most. In addition to the resistance, the inductance of each coil also changes. This affects the control of each axis as the time response changes accordingly. Finally, the space congestion of the whole device is imposed by the pair with the largest radius (contained in a sphere of radius $R_{\text{footprint}}$ as shown in Fig. 3.24b). In contrast, the ROI with a uniform field (working area) is restricted by the pair with the smallest radius. This results in a device poorly using the available space, strongly limiting its integration.

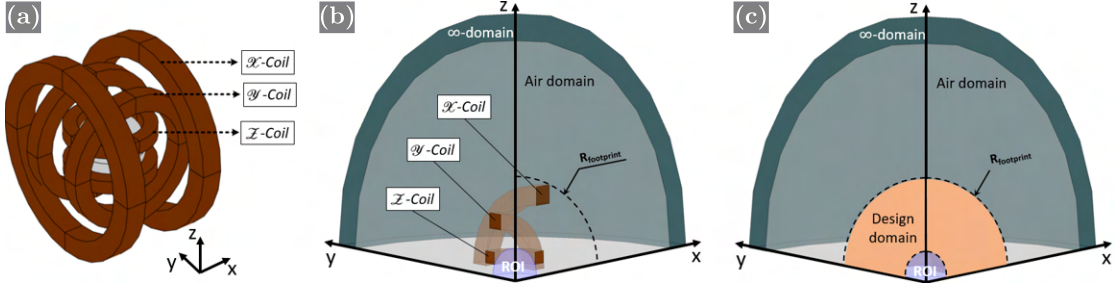


Figure 3.24: Reference system and design problem: (a) Arrangement of 3 nested pairs of Helmholtz coils; (b) corresponding cut view resulting in an eighth of the total space; and (c) related design problem for topology optimization. Figure reused from [131]. ©2023 IEEE.

In order to tackle such limitations, the developed computational design method is an excellent candidate for exploring novel arrangements of the coils in space. The goal is to improve field homogeneity for a fixed footprint while enforcing equilibrium between the different axes.

3.3.2.b Metrics

Additional metrics than the one derived in Section 3.1.1.c are presented here to express the uniformity of the generated magnetic flux densities with respect to the one at the origin of the coordinate system. For each set of i -coil, we define $\delta_{x:i}^{\text{uni}}$, $\delta_{y:i}^{\text{uni}}$, and $\delta_{z:i}^{\text{uni}}$ the uniform spans along the x -, y -, and z -axis respectively. They correspond to the normalized lengths with a uniformity error of the i -directional magnetic field inferior to 1%. The normalization is performed using the diameter of the spherical Region Of Interest (ROI) with radius R_{ROI} . The sets where the error is inferior to 1% are considered convex.

$$\begin{aligned}\delta_{x:i}^{\text{uni}} &= \frac{1}{2R_{\text{ROI}}} \int_{\Gamma_x} dx', \quad \forall x' \in \left\{ \left| \frac{B_x^i(x', y'=0, z'=0)}{B_x^i(x'=0, y'=0, z'=0)} - 1 \right| < 0.01 \right\}, \\ \delta_{y:i}^{\text{uni}} &= \frac{1}{2R_{\text{ROI}}} \int_{\Gamma_y} dy', \quad \forall y' \in \left\{ \left| \frac{B_y^i(x'=0, y', z'=0)}{B_y^i(x'=0, y'=0, z'=0)} - 1 \right| < 0.01 \right\}, \\ \delta_{z:i}^{\text{uni}} &= \frac{1}{2R_{\text{ROI}}} \int_{\Gamma_z} dz', \quad \forall z' \in \left\{ \left| \frac{B_z^i(x'=0, y'=0, z')}{B_z^i(x'=0, y'=0, z'=0)} - 1 \right| < 0.01 \right\},\end{aligned}\tag{3.46}$$

with Γ_x , Γ_y , Γ_z the x -, y -, and z -axis respectively. Similarly, a measure of the normalized volume with a uniform i -directional magnetic field is formulated:

$$\begin{aligned}v_{\mathcal{X}}^{\text{uni}} &= \frac{1}{\frac{4\pi}{3}R_{\text{ROI}}^3} \iiint_{V_{\text{ROI}}} dx' dy' dz', \quad \forall \{x', y', z'\} \in \left\{ \left| \frac{B_x^{\mathcal{X}}(x', y', z')}{B_x^{\mathcal{X}}(x'=0, y'=0, z'=0)} - 1 \right| < 0.01 \right\}, \\ v_{\mathcal{Y}}^{\text{uni}} &= \frac{1}{\frac{4\pi}{3}R_{\text{ROI}}^3} \iiint_{V_{\text{ROI}}} dx' dy' dz', \quad \forall \{x', y', z'\} \in \left\{ \left| \frac{B_y^{\mathcal{Y}}(x', y', z')}{B_y^{\mathcal{Y}}(x'=0, y'=0, z'=0)} - 1 \right| < 0.01 \right\}, \\ v_{\mathcal{Z}}^{\text{uni}} &= \frac{1}{\frac{4\pi}{3}R_{\text{ROI}}^3} \iiint_{V_{\text{ROI}}} dx' dy' dz', \quad \forall \{x', y', z'\} \in \left\{ \left| \frac{B_z^{\mathcal{Z}}(x', y', z')}{B_z^{\mathcal{Z}}(x'=0, y'=0, z'=0)} - 1 \right| < 0.01 \right\}.\end{aligned}\tag{3.47}$$

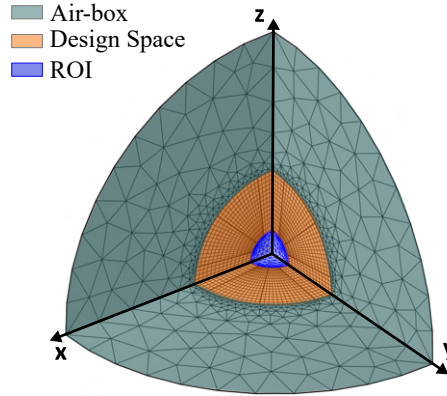


Figure 3.25: Design problem n°6: Mesh and domains. Figure reused from [131]. ©2023 IEEE.

3.3.2.c Reference and loading-cases

A reference nested tri-coils Helmholtz system is taken from [130, Table.1]. It is scaled to a desired target flux density of $B_0 = 6$ mT. The system fits into a sphere of radius $R_{\text{footprint}}$ and is shown in Fig. 3.24b. An "air-box" is needed in electromagnetic applications to allow magnetic flux to propagate freely. It is achieved by the combination of a large spherical air-domain centered around the device and having its external shell set to an "infinite element domain"⁷. The design domain into which the layout of the different coils is investigated is fixed to the region between the sphere delimiting the footprint and the smaller sphere delimiting the ROI at its center. This is shown in Fig. 3.24c, with the corresponding meshed domains in Fig. 3.25. Only one-eighth of the geometry is considered due to symmetry. This enables a substantial reduction of the search space, which is essential to reduce the number of design variables and, thus, the computational burden. Furthermore, the chosen numerical method relies on FEA, which is incredibly demanding in 3-D.

As single conductor coils are considered in this work (no modeling of the turns), the electromagnetic potential $\theta^i = N^i \cdot I$ (amperes-turns product, with N^i the number of turns of the i -coil) is extracted from the reference system for comparison instead of the number of turns. The coils are thus simulated as single conductors powered by a current source of a magnitude equal to the electromagnetic potential $I^i \equiv \theta^i$. The reference Helmholtz system, having initially coils with a different number of turns, are here powered by different electromagnetic potentials (i.e. currents). Meanwhile, the targeted system should have coils with balanced electromagnetic potentials and are thus powered by the same current $I (= \theta)$. The boundary conditions of the corresponding electric conduction problems are formulated as a current source I and an electric potential fixed to the ground (GND) on different boundaries. Some empty domains separate these boundaries, enabling proper current circulation and providing empty spaces to access the ROI. Their position depends on the considered loading-case associated with the \mathcal{X} -, \mathcal{Y} -, and \mathcal{Z} -coils. It is shown in the top part of Fig. 3.26. Regarding the boundary conditions of the magnetic field computation, perfect magnetic conductor condi-

⁷The infinite element domain is a feature provided by COMSOL[®]. The boundary conditions on the outside of the infinite element layer are effectively applied at a vast distance from any region of interest. This is permitted when the dependent variables vary slowly with the radial distance from the center of the physical domain (which is the case in this configuration).

3.3 Asymmetric winding design in 3-D topology optimization

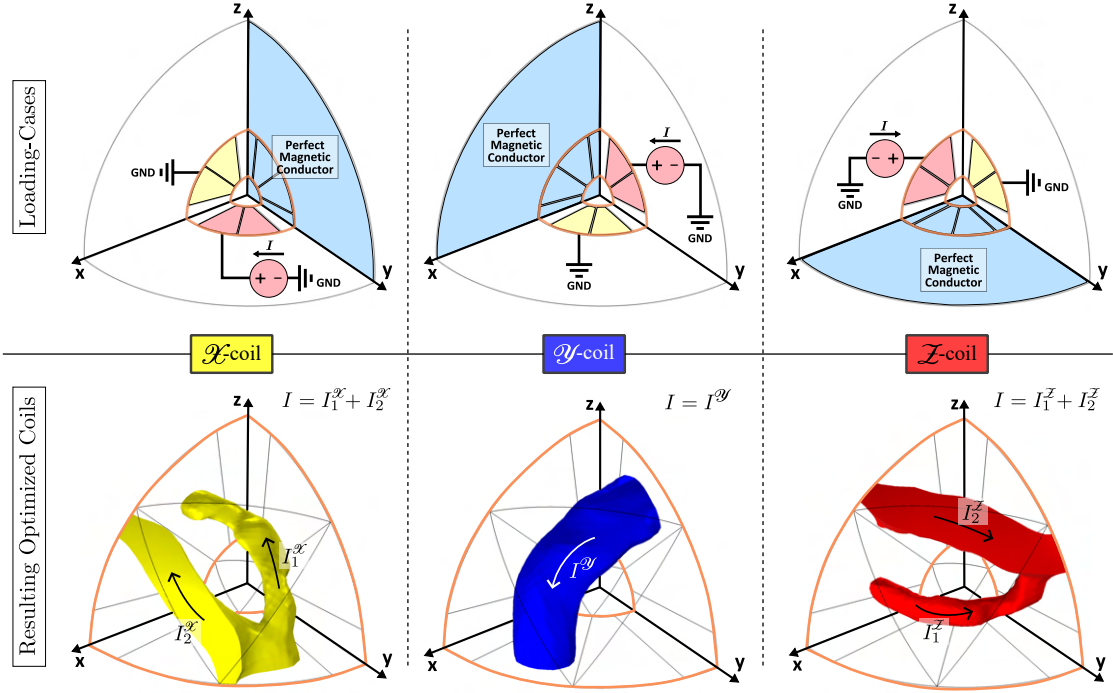


Figure 3.26: Design problem n°6: $1/8^{\text{th}}$ of the complete geometry is considered due to symmetry. *At the top:* loading-cases with corresponding boundary conditions, and *at the bottom:* resulting optimized topology inside the design space (orange outline) for the \mathcal{X} -, \mathcal{Y} -, \mathcal{Z} -coil respectively. Figure reused from [131]. ©2023 IEEE.

tions enforce $\mathbf{n} \times \mathbf{H}^i = \mathbf{0}$ on the corresponding boundary (with \mathbf{n} its normal vector) to assure a magnetic field perpendicular to the boundary. Meanwhile, the other boundaries insulate the magnetic field by enforcing a tangential magnetic field ($\mathbf{n} \cdot \mathbf{H}^i = 0$) to the corresponding boundary.

3.3.2.d Optimization formulation

The variables describing the topologies of the coils defined in Section 3.3.1.b are used as control variables to the optimization problem. The optimization targets a better arrangement of the coils to achieve better field uniformity and balance between the different axes. These behaviors can be enforced as objective functions or constraints⁸ to the optimization problem. A global magnetic field uniformity error inside the volume of the ROI is formulated for each

⁸There is a duality between these two as many gradient-based optimizers reformulate the initial optimization problem to an unconstrained one by integrating the constraints as sub-objectives[29]. Here, a choice has been made between objective functions and constraints, but another formulation is possible.

axis and each coil in order to evaluate the magnetic performance of the designed coils:

$$\begin{aligned} f_B^{\mathcal{X}} &= \iiint_{V_{\text{ROI}}} \left(\frac{B_x^{\mathcal{X}}(x, y, z)}{B_x^{\mathcal{X}}(x=0, y=0, z=0)} - 1 \right)^2 dx dy dz, \\ f_B^{\mathcal{Y}} &= \iiint_{V_{\text{ROI}}} \left(\frac{B_y^{\mathcal{Y}}(x, y, z)}{B_y^{\mathcal{Y}}(x=0, y=0, z=0)} - 1 \right)^2 dx dy dz, \\ f_B^{\mathcal{Z}} &= \iiint_{V_{\text{ROI}}} \left(\frac{B_z^{\mathcal{Z}}(x, y, z)}{B_z^{\mathcal{Z}}(x=0, y=0, z=0)} - 1 \right)^2 dx dy dz. \end{aligned} \quad (3.48)$$

The objective function of the optimization problem is the sum of the three different uniformity errors normalized by the volume of the ROI:

$$f = \frac{f_B^{\mathcal{X}} + f_B^{\mathcal{Y}} + f_B^{\mathcal{Z}}}{4\pi R_{\text{ROI}}^3/3}. \quad (3.49)$$

Three sets (one per coil type) of three constraints are proposed. The first three are the conventional volume limitations restraining each artificial density distribution's average density (below Vol^* as in (3.21)). The next three constraints are targets for the magnetic flux density B_0 at the center of the ROI for each loading case:

$$\begin{aligned} 0.9 B_0 &\leq B_x^{\mathcal{X}}(x=0, y=0, z=0) \leq 1.1 B_0, \\ 0.9 B_0 &\leq B_y^{\mathcal{Y}}(x=0, y=0, z=0) \leq 1.1 B_0, \\ 0.9 B_0 &\leq B_z^{\mathcal{Z}}(x=0, y=0, z=0) \leq 1.1 B_0. \end{aligned} \quad (3.50)$$

An error of $\pm 10\%$ is permitted to provide more freedom in the optimization. Finally, the last three are limits on the Joule losses generated within each coil:

$$R^{\mathcal{X}} \cdot I^2 \leq Q_0 \quad ; \quad R^{\mathcal{Y}} \cdot I^2 \leq Q_0 \quad ; \quad R^{\mathcal{Z}} \cdot I^2 \leq Q_0 \quad (3.51)$$

with R^i the electrical resistance of the i -coil and Q_0 the fixed limit. This provides control over the coils' heating and assures proper connections to the boundaries where the current source and the ground are imposed. Indeed, as air is given a small electrical conductivity (for numerical stability), the current source assures a constant current flowing in the design space, whatever the material distribution. Thus, if the losses (varying with the resistance of the coils) were not limited, nothing would require the coil distributions to properly connect the boundaries mentioned above, possibly resulting in an *open-circuit*.

3.3.2.e Results

The proposed methodology is no longer implemented in the framework described in Section 3.1 and Section 3.2 but in COMSOL® 6.0. It couples the MAGNETIC AND ELECTRIC FIELD physic of the AC/DC module with the OPTIMIZATION module. The chosen optimizer is the Method of Moving Asymptotes (MMA) [34], another popular gradient-based optimizer used

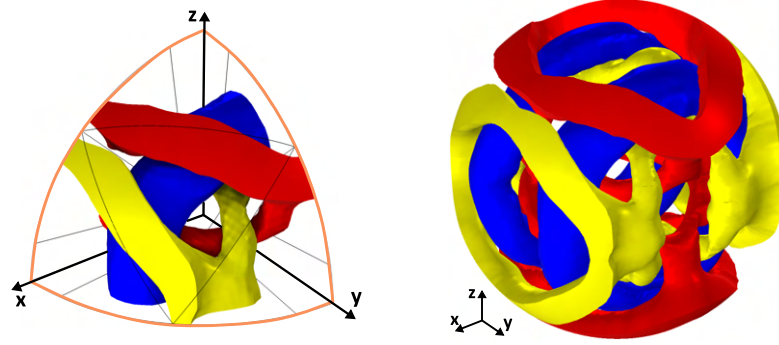


Figure 3.27: Full 3-D system with topology optimized coils. Figure reused from [131]. ©2023 IEEE.

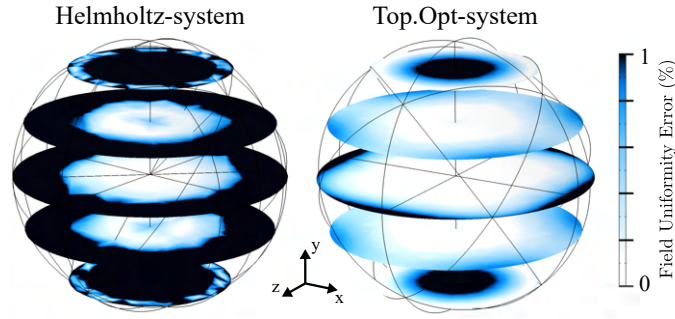


Figure 3.28: Comparison of the magnetic field uniformity error inside the ROI $|B_y^{\mathcal{Y}}(x, y, z)/B_y^{\mathcal{Y}}(x=0, y=0, z=0) - 1|$ for the \mathcal{Y} -coil. Figure reused from [131]. ©2023 IEEE.

by the topology optimization community. The sensitivity is also automatically derived with the adjoint variable method. The volume fraction is set to $\text{Vol}^* = 0.15$ and the penalty factor of the SIMP scheme to $q = 4$. The target flux density is fixed to $B_0 = 6$ mT, while the losses upper limit to $Q_0 = 0.8$ W. The design problem solved is the design problem n°6 studied in this manuscript. The domains are meshed irregularly with different element types. It contains 34'411 elements, among which 9'523 tetrahedra compose the ROI, and 6'468 hexahedra defined by 8'145 vertices compose the design domain. Each artificial density distribution is defined onto these vertices, resulting in a total number of control variables of 24'435. The different meshed domains are shown in Fig. 3.25. The complete optimization took 56 hours to finish using a Windows workstation with an Intel Xeon 20-core processor and 128G memory. The computational cost has significantly increased despite relying on fewer control variables than in Section 3.1 or Section 3.2. It is explained by the fact that 3-D FEA is substantially computationally more demanding than 2-D FEA. The number of DOFs to determine is much larger in 3-D FEA, and the numerical tools solving the equations are much more onerous in terms of memory usage and processor power. Furthermore, in this design problem, three different FEAs are solved, one per-loading case, which also increases the computational cost accordingly. These loading cases could be solved in parallel to reduce the processing time but would be more computationally demanding [60].

The eighths of coils resulting from the optimization are shown in the bottom part of Fig. 3.26

Table 3.7: Comparison of the Helmholtz and Topology Optimized (Top.Opt.) 3-D electromagnetic manipulator. The values are scaled to a full system with mirrored coils.

i -coil	Helmholtz			3-D Top.Opt.		
	\mathcal{X}	\mathcal{Y}	\mathcal{Z}	\mathcal{X}	\mathcal{Y}	\mathcal{Z}
θ^i (A)	405	279	177	177	177	177
Q^i (W)	11.8	5.6	2.3	6.38	6.26	6.38
$\delta_{x:i}^{\text{uni}}$	0.34	0.34	0.26	1.41	1.77	1.41
$\delta_{y:i}^{\text{uni}}$	0.53	0.34	0.23	1.41	1.77	1.41
$\delta_{z:i}^{\text{uni}}$	0.5	0.34	0.08	1.40	1.77	1.41
v_i^{uni}	0.12	0.06	0.02	0.90	0.95	0.89

below their associated LC. Despite having two coils with similar topologies⁹, the third one has a different shape. The fully reconstructed topology forming a topology-optimized 3-D electromagnet manipulator is shown in Fig. 3.27. While intertwined, one can see that the different coils do not mix with each other as desired. Fig. 3.28 shows the difference in field homogeneity between the Helmholtz system and the optimized one for the \mathcal{Y} -coil as an example. The latter exhibits an improved uniformity inside the ROI compared to the reference while keeping the same footprint. This is confirmed in Table 3.7, which evaluates the metrics for each coil of the reference and topology-optimized magnetic manipulator. The generated system displays a better electrical and magnetic balance between the different coils and axes than the Helmholtz electromagnet manipulator. Furthermore, the magnetic uniformity inside the ROI is significantly improved with the novel topology¹⁰. Indeed, it achieves a uniform magnetic field inside around 90% of the volume of the ROI, while only 12% is achieved by the best set of coils along their respective axis for the Helmholtz system.

The generated topologies assume single conductor modeling, while a realistic one requires multiple turns to prevent relying on very large input currents. A possible future methodology to reconstruct the distribution of the different turns is discussed here. A *turn density* could be formulated based on the norm of the flowing current. This would identify the distribution of turns that better corresponds to the simulated current flow. Such a discretization technique is expected to degrade the performance partially, but a dedicated framework could keep this loss minimal. The exotic nature of the generated coils is naturally complicated to achieve with conventional manufacturing methods, but this is not the case with additive manufacturing technologies. Several examples are encouraging regarding the feasibility of such designs [107, 132].

⁹The \mathcal{X} -coil is the same as the \mathcal{Z} -coil but rotated and mirrored in space to align with its axis of interest properly

¹⁰The metrics $\delta_{x:i}^{\text{uni}}$, $\delta_{y:i}^{\text{uni}}$, and $\delta_{z:i}^{\text{uni}}$ are larger than 1 in the case of the 3-D topology-optimized system because the corresponding axes with uniform field extend beyond the reference region of interest.

3.3.3 Conclusion

The developed framework for winding design is modified to simultaneously design multiple coils with different purposes (and shapes) inside a shared design space. This is achieved by combining multi-loading cases FEA with the previously introduced multi-coil interpolation scheme. The approach's effectiveness is demonstrated in the design of a balanced 3-D electromagnet manipulator achieving superior performance than a reference system.

Publication related to this section:

A. Thabuis, X. Ren, T. Duong and Y. Perriard, "Exploring Beyond the Helmholtz Coils for Uniform Magnetic Field Generation With Topology Optimization," in IEEE Transactions on Magnetics, vol. 58, no. 9, pp. 1-4, Sept. 2022, Art no. 7001404, doi: 10.1109/TMAG.2022.3183362, [129].

A. Thabuis, M. C. Rivera, X. Ren, and Y. Perriard, "Topology Optimization of an Electromagnet Manipulator for 3D Uniform Magnetic Field," in IEEE Transactions on Magnetics, Feb. 2023, doi: 10.1109/TMAG.2023.3247867, [131].

3.4 Fabricated topology-optimized coils



MULTIPLE topologies generated by the presented automated design framework could have been studied in the next chapter related to "Additive Manufacturing of Electromagnetic Coils". However, due to the project's timeline associated with an industrial partner, a state-of-the-art topology has been selected, not a topology-optimized one. Nevertheless, we desire to support the feasibility of manufacturing the obtained exotic shapes in this short section. That is why it has been decided to print some of the topology-optimized coils with more affordable and available materials (polymers) and machines for the showcase. The resulting coils are non-conductive, but as most additive manufacturing technologies rely on the same principle of fabricating the parts layer by layer, the nature of the material (generally) does not disprove the manufacturing feasibility.

Examples of coils without turns are shown in Fig. 3.29. A standard desktop printer using the FFF technique is used. The pencil shown for scale is 17.5 cm long. The first example is the topology-optimized 3-D electromagnet from Fig. 3.27. The eighths of each coil are printed independently and then glued together for assembly. This approach was chosen for simplicity, but the whole system could have been printed at once with careful support design or by relying on the recent development of conical slicing for a *support-free* printing process [133]. The other example shows the coils constituting the overlapping windings for rotating and linear electric motors from Fig. 3.21. The coils are printed individually and then assembled.

The possible ways to distribute the turns have not been covered yet but are further discussed in Section 4.1.2. When considering the results from the winding design with 2.5-D topology optimization presented in Fig. 3.21, there are only three ways of distributing the turns. It can be done outside the design plane, inside the design plane, or a combination of both. The former is presented here. The topology is repeated multiple times in the direction normal to the plane, resulting in a *helix-like* geometry. This is shown in Fig. 3.30 with coils made of 10 turns manufactured in PA with the SLS. The different turns have a thickness of 300 μm and 600 μm in single and doubled-thickness regions, respectively. Due to the thin nature of the turns, the regions two times thicker are contoured with a dotted green line for better illustration inside the figure. A full winding is assembled with the different phases marked by different colors with markers.

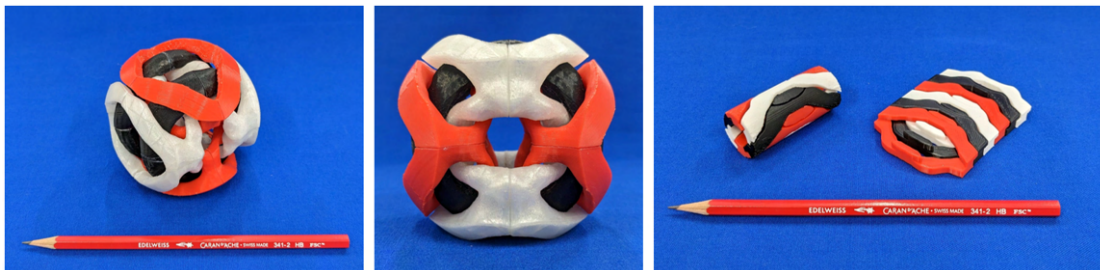


Figure 3.29: Topology-optimized coils without turns additively manufactured in PLA using the fused filament fabrication technique: (left and middle) 3-D electromagnet, and (right) overlapping winding for rotating and linear electric motor.

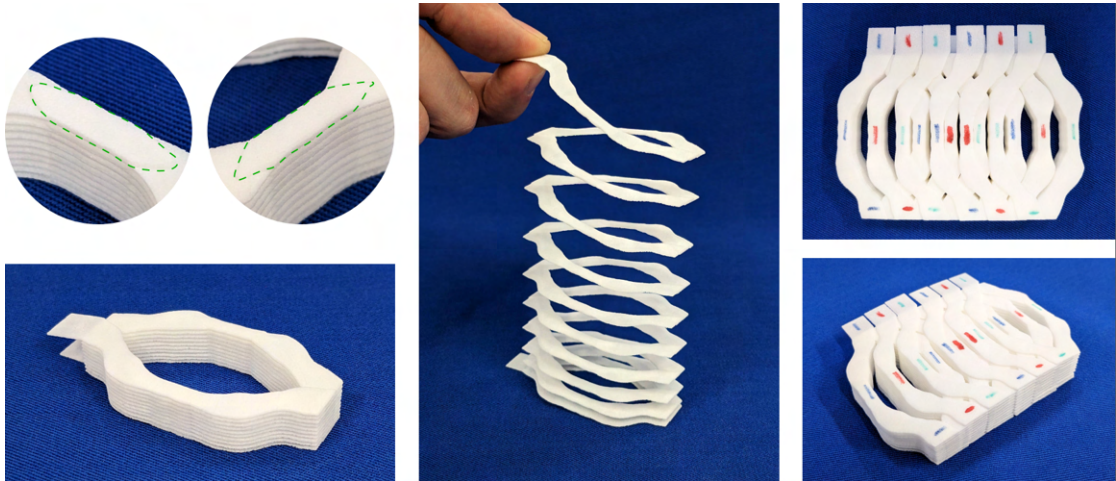


Figure 3.30: Topology-optimized coil with turns distributed out-of-the-plane resulting in a "spring-like" geometry, printed in PA by SLS.

Another topology-optimized coil developed for the project with the industrial partner has been manufactured in copper for the showcase. It relied on the powder bed fusion technology and was manufactured by the German company Protiq [134]. This is shown in Fig. 3.31.

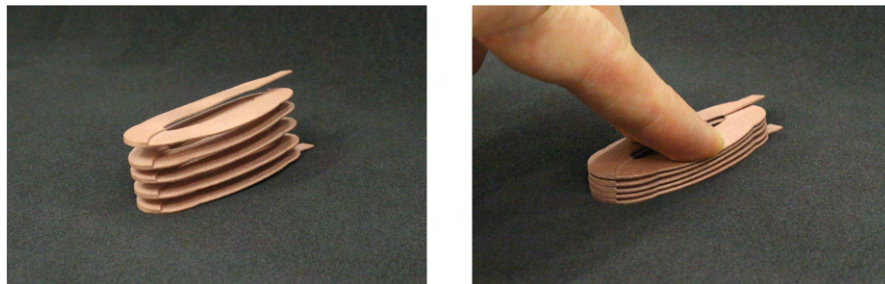


Figure 3.31: Topology-optimized coils additively manufactured in copper.

These examples validate the feasibility of additively manufacturing the topology-optimized coils developed by our automated design tool. The next chapters further support this claim with a reference topology printed in metal.

3.5 Conclusion



THIS chapter presents the developed computational design tool aiming for improved electromagnetic devices. It implements the topology optimization method to design electromagnetic coils and winding. The fundamentals are introduced through 2-D problems, investigating the ideal conductor layout inside the plane. Various metrics are studied and discussed. In addition to study cases containing a magnetic field imposed by external sources, study cases considering the magnetic field generated by the conductor path being designed in the presence of ferromagnetic materials are presented for the first time. This establishes the possibility of designing conductor layouts in 2-D, which can be interpreted as an electromagnetic *coil* even though the new designs do not necessarily have the circled shape.

The following section builds upon the previous groundwork for achieving a winding design made of multiple coils sharing the same design space. It extends the initial formulation to more advanced problems, covering more complex electromagnetic systems. A *multi-coil* interpolation scheme is proposed and integrated into the topology optimization framework. Winding design is achieved without *a-priori* knowledge of the position and packing of its constituting coils, which was not possible before. The 2-D analysis is also extended to 2.5-D in order to achieve the design of overlapping winding while keeping a reasonable computational time. A new topology-optimized coil is obtained and compared to two references: the rhombus and diamond topologies. The generated winding has a motor constant 17.5% and 16.7% larger than the references, respectively, which confirms the great potential of the developed computational design framework.

The third section extends the previous formulation to the design of asymmetric windings composed of multiple coils with different purposes, requiring multiple FEAs. It is demonstrated through the 3-D topology optimization of an electromagnet manipulator. The obtained design better harvests the available space, balancing the effect of the different coils as desired. The resulting system performs significantly better than the reference one. It has a region with uniform magnetic field 7.5 times larger while assuring balanced Joule losses.

Finally, the fabrication of the topology-optimized coils is discussed. Despite not being printed in metal, the feasibility of additively manufacturing the obtained topologies is demonstrated using non-conductive materials. It is confirmed by the next chapter, which studies coils with similar features as the topology-optimized ones but printed in metal.

4 ADDITIVELY MANUFACTURED COILS

Content

4.1 Case study and first designs	74
4.1.1 Machine of interest: Coreless linear motor with permanent magnets . .	74
4.1.2 Coil topology and turn distributions	75
4.2 Harvesting the design freedom provided by additive manufacturing	77
4.2.1 Adaptation of conventional shapes to 3D-printing	77
4.2.2 Completed linear winding	78
4.2.3 Multi-functional winding	81
4.2.4 Conclusion	86
4.3 Experiments	88
4.3.1 Printing process	88
4.3.2 Post-processing of the coils	93
4.3.3 Electromagnetic properties	99
4.3.4 Thermal properties	103
4.3.5 Conclusion	105
4.4 Conclusion	106

This chapter covers the feasibility of additively manufacturing a winding to integrate into a specific electric motor. The machine and winding of interest are first introduced. Then, various design principles harvesting the design freedom provided by AM technologies are presented. The experimental works are then presented, starting with the fabrication and post-processing of the coils. It is followed by different tests characterizing the electromagnetic and thermal properties of the printed coils.

4.1 Case study and first designs



WO main principles are studied in this thesis: the computational design framework and the feasibility of 3D printing winding. They have been researched in parallel due to the timeline requirements of the project with an industrial partner. Thus, it has been decided to select a state-of-the-art topology as a reference for the winding to be additively fabricated. Despite not being topology-optimized, the chosen coil design is further investigated to harvest better the freedom provided by AM technologies. It still permits validating the feasibility of such a method to manufacture coils with peculiar characteristics. Thus, we can confidently affirm that the topology presented in Fig. 3.21 could also be successfully manufactured with this technique.

4.1.1 Machine of interest: Coreless linear motor with permanent magnets

A linear coreless permanent magnet machine is selected here. Nevertheless, the presented concepts could be extended to other machine types, such as a rotating one with a slotted stator. The machine of interest is shown in Fig. 4.1. It consists of two magnet arrays separated by an air-gap forming a U-shape. The machine is configured such that the winding glides between the fixed PMs. The electric current flowing through the winding is coupled with the magnetic field imposed by the PMs, resulting in a Lorentz force driving the motor. It is a 3-phase machine with 4 coils connected in series in each phase. The magnetic pole span is 32 mm long (length along the x -axis) in this rail for a magnet height of 40 mm (length along the y -axis). The available space provided by the lack of iron slots leaves the winding shape to be skewed, enabling overlap of the different coils for better integration and improved motor constant. The different coils are not concentrated but distributed across the air gap. The presented machine is an excellent support of the proposed concepts. Despite having many advantages such as high efficiency, no force ripple, and a large motor constant, these machines with skewed (a.k.a. self-supported) winding have strong thermal limitations. Indeed, the reduced exchange surface due to the absence of an iron core limits the cooling of the device. That is why the chosen system engineering approach considering the heat dissipation capabilities while designing the winding, is especially significant for these motors.

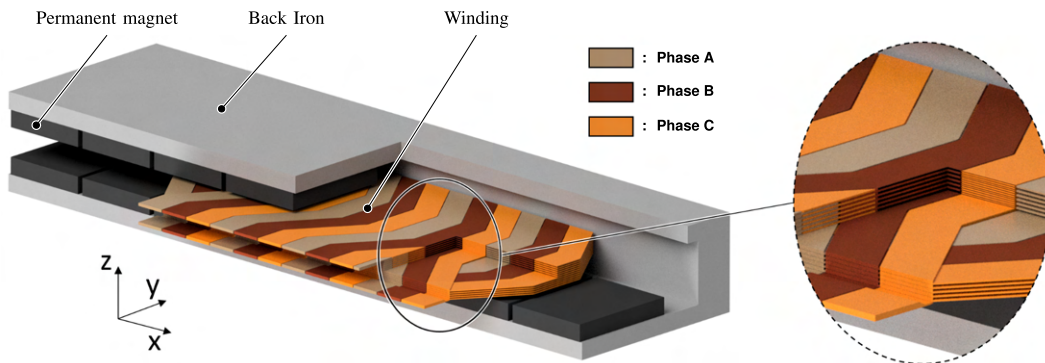


Figure 4.1: Machine of interest: a coreless linear motor with permanent magnets. The winding topology corresponds to a modified diamond skewed/self-supported type. Figure reused from [135]. ©2022 IEEE.

4.1.2 Coil topology and turn distributions

Different skewed winding topologies have been developed for such machines: *rhombic*, *diamond*, *zigzag* (Faulhaber) types [81], or ones fabricated with PCB technology exhibiting tracks with varying width [82]. In this work, a modified version of the *diamond*-type with varying width is chosen [18]. The additional degree of freedom along the third dimension provided by AM is exploited to push even further the performance. Indeed, the thickness of the tracks at the end-winding is also increased to reduce the resistance locally. The coil-span length equals the magnetic pole span length imposed by the PM. The phases of the full winding mechanically cover 2 pole-pairs of the magnet arrays. The winding footprint without the connections is $160 \text{ mm} \times 68 \text{ mm} \times 7.5 \text{ mm}$ along x , y , and z respectively.

Two types of coils with different turn distributions are explored: the one with *in-plane* (IP) distributed turns, in the manner of a spiral, and the one with *out-of-plane* (OP) distributed turns, in the manner of a helix. The Fig. 4.2 shows the two types of coils. The referenced plane is defined by the *diamond* shape, corresponding to the xy -plane. One can observe that the *in-plane* type spans over two levels along the z -direction. This results in thicker turns than in the other type. Manufacturing limitations required the inner turn to be wider than the others to prevent breaking at sharp angles. Meanwhile, the *out-of-plane* type is composed of thinner (but wider) turns that are spread over the z -direction to overlap with the neighboring coils. The turns of the different coils are intertwined with each other. It is better illustrated in the zoomed view of Fig. 4.1.

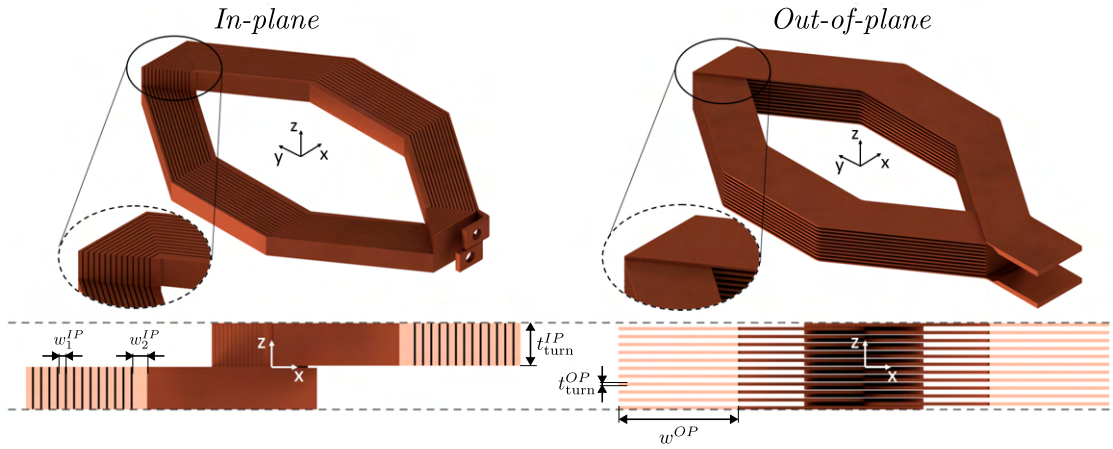


Figure 4.2: 3D and side view of the reference topology with two different types of turn distribution: (left) *in-plane*, and (right) *out-of-plane*. They both have the same footprint along the three dimensions.

The coils mentioned above have been designed in two steps. First, the size limitations imposed by the manufacturing method have been considered to determine the size and number of different turns. The *diamond* shape has then been parametrized by a few geometric parameters and optimized based on the FEA simulations presented in Appendix B. Some scaling laws are also provided to adapt the design to different machine sizes. The critical dimensions are summarized here. The *in-plane* coil is constituted of 15 turns, with a thickness

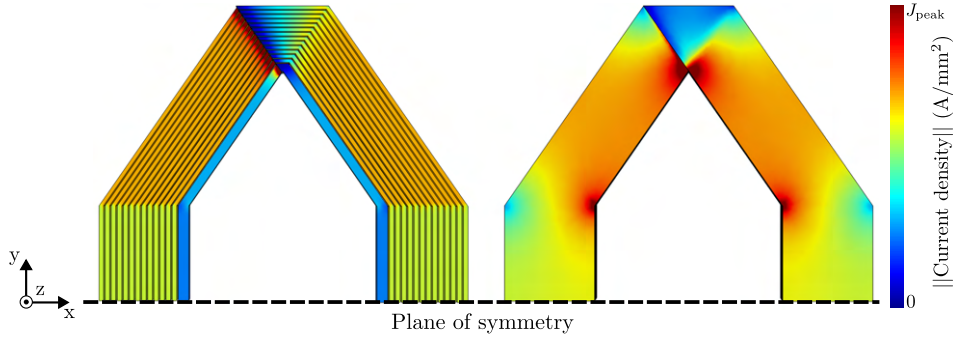


Figure 4.3: Norm of the current density in two types of turn distribution: (left) *in-plane*, and (right) *out-of-plane*. $J_{\text{peak}} = 2.5 \text{ A/mm}^2$ for a flowing current of $I = 6 \text{ A}$.

(length along the z -axis) of $t_{\text{turn}}^{IP} = 3.7 \text{ mm}$. The width (length along the y -axis) of the diamond straight segment is $w_2^{IP} = 1.2 \text{ mm}$ for the inner turn, and $w_1^{IP} = 0.5 \text{ mm}$ for the others. Meanwhile, the *out-of-plane* coil is composed of 11 turns with a thickness of $t_{\text{turn}}^{OP} = 0.3 \text{ mm}$. The width of the diamond straight segment is $w^{OP} = 10.3 \text{ mm}$.

The number of turns is relatively small compared to the traditional rounded wire winding due to limitations on the achievable size by the additive manufacturing process. As the technology rapidly improves, the number of turns is expected to be larger in future iterations. This improvement could also combine the two types of turn distributions, having them simultaneously distributed inside and out of the plane. Despite having the same general shape, the two types of coils will not perform in the same manner. Indeed, the size and distribution of the turns already affect the flowing current density as shown in Fig. 4.3. The wide nature of the turns *out-of-plane* distributed results in the accumulation of the current at the inner corners of the diamond shape, and thus a more prominent peak current density J_{peak} . Meanwhile, the *in-plane* distributed turns have a more uniform current density distribution (except the inner turn due to its doubled width). This difference will affect the electromagnetic properties. Furthermore, the AC losses will be larger in the *out-of-plane* coil because the width of the conductor normal to the varying flux (coming from the motion across the air-gap with respect to the PMs) is much larger than for the *in-plane*. This leaves a smaller effective resistance and thus a larger induced current magnitude¹. Nevertheless, considering the current state of metal additive manufacturing technologies, the *out-of-plane* coil type is more straightforward to manufacture than the *in-plane* coil. It is further discussed in Section 4.3.

¹A possibility to mitigate the AC losses would be to perform some slits inside the turns, increasing the effective resistance as already demonstrated for PCB winding [86].

4.2 Harvesting the design freedom provided by additive manufacturing



ARIOUS strategies are proposed in this section to address Joule losses and heat dissipation by harnessing the design freedom offered by AM. Naturally, they could be combined with computational design methods for further improvement. The first strategy is dedicated to adapting conventional coils, normally composed of round wire to 3D printing. The next one focuses on design freedom specific to winding for linear motors. Finally, the last strategy proposes combining the electric motor's electromagnetic and cooling functions into a single component: a multi-functional 3D-printed coil with integrated heat sinks.

4.2.1 Adaptation of conventional shapes to 3D-printing

The first limitation of conventional winding (that is lifted when considering additive manufacturing) is the rounded cross-section of the turns constituting the coil. The circled shape results in poor packing of the different turns within the available space. A solution is to fabricate the turns with a rectangular (or other types of polygons) cross-section to ideally achieve a perfect packing of the different turns. For the same footprint and turns with the same surface area, a coil having its turns with a rectangular cross-section could potentially be composed of a larger number of turns, increasing its electromagnetic potential. When considering AM winding, the second degree of freedom to harvest is the possibility of having turns with a varying cross-section. Indeed, they could vary along each turn to better fill empty gaps, which are inevitable for specific coil geometries with turns of a fixed cross-section. It permits improving the fill-factor of the winding inside the machine. This is illustrated in Fig. 4.4a for specific parts of the selected *diamond*-shaped coil. Such a feature has been massively investigated in PCB windings having tracks with varying widths [19]. Nevertheless, AM offers the advantage

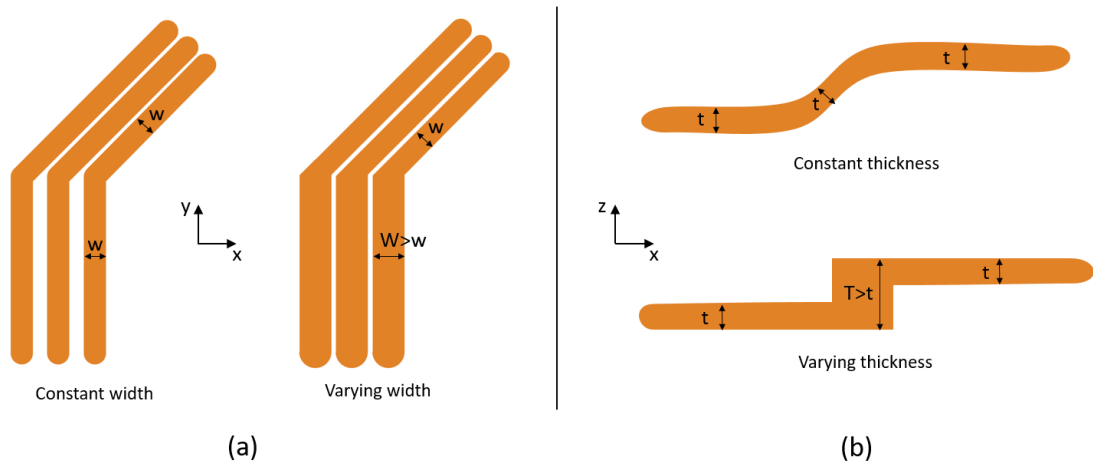


Figure 4.4: Possibility of varying the cross-section of the conductor tracks due to additive manufacturing technologies: (a) Increased width depending on the coil geometry, (b) increased thickness when changing layers in overlapping coils.

of changing the track's thickness in addition to its width. It allows further improvement of the fill-factor of the coils when considering overlapping windings spanning two different layers, and where a varying thickness is meaningful. It is illustrated in Fig. 4.4b, where the transition region between two layers (often localized at the coil head, i.e. end-winding) has a thickness increased compared to standard turns with constant cross-section. In this context, the improved fill-factor results in a local reduction of the electrical resistance where the cross-section is increased. A motor winding with lower electrical resistance results in lower Joule losses for a fixed input current and, thus, a better efficiency when the AC losses are not considered. Overall, the resistance can be reduced by around 25% with respect to a rounded wire configuration with constant cross-section [18].

4.2.2 Completed linear winding

Fig. 4.5 shows that the linear configuration of a motor can be seen as the *unrolled* version of the rotating one (with radial flux). When considering overlapping or distributed windings, it results in a lack of periodicity in the winding where the cut has been performed to unroll it. Thus, each border of the linear winding has an empty space previously taken by the other border from the rotating configuration. Herein, such linear windings are always *incomplete*. Similarly to the strategy from the previous section, we propose to complete the empty spaces with conductive material by changing the cross-section of the tracks. The fill-factor of the winding is thus improved. We name this new winding a *completed* linear winding. It is presented in Fig. 4.6a for coils with *out-of-plane* distributed turns. Nevertheless, the same principle also stands for *in-plane* distributed turns. One can see that the thickness (length along the z -axis) of the turns at the border is increased in the *completed* version with respect to the *incomplete* one. The different filling colors refer to different phases, and the different outline colors refer to different coil groups. The individual coils from the different coil groups are connected in series for each phase.

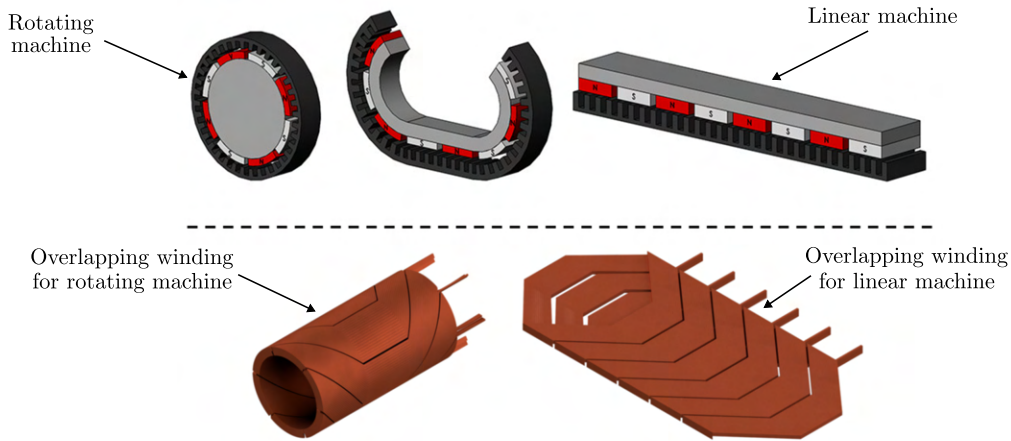


Figure 4.5: Winding for rotating (radial flux) machine VS linear machine: (top) unrolled perception of a slotted stator [113], (bottom) application to an overlapping winding for a coreless/slotless electric motor [136].

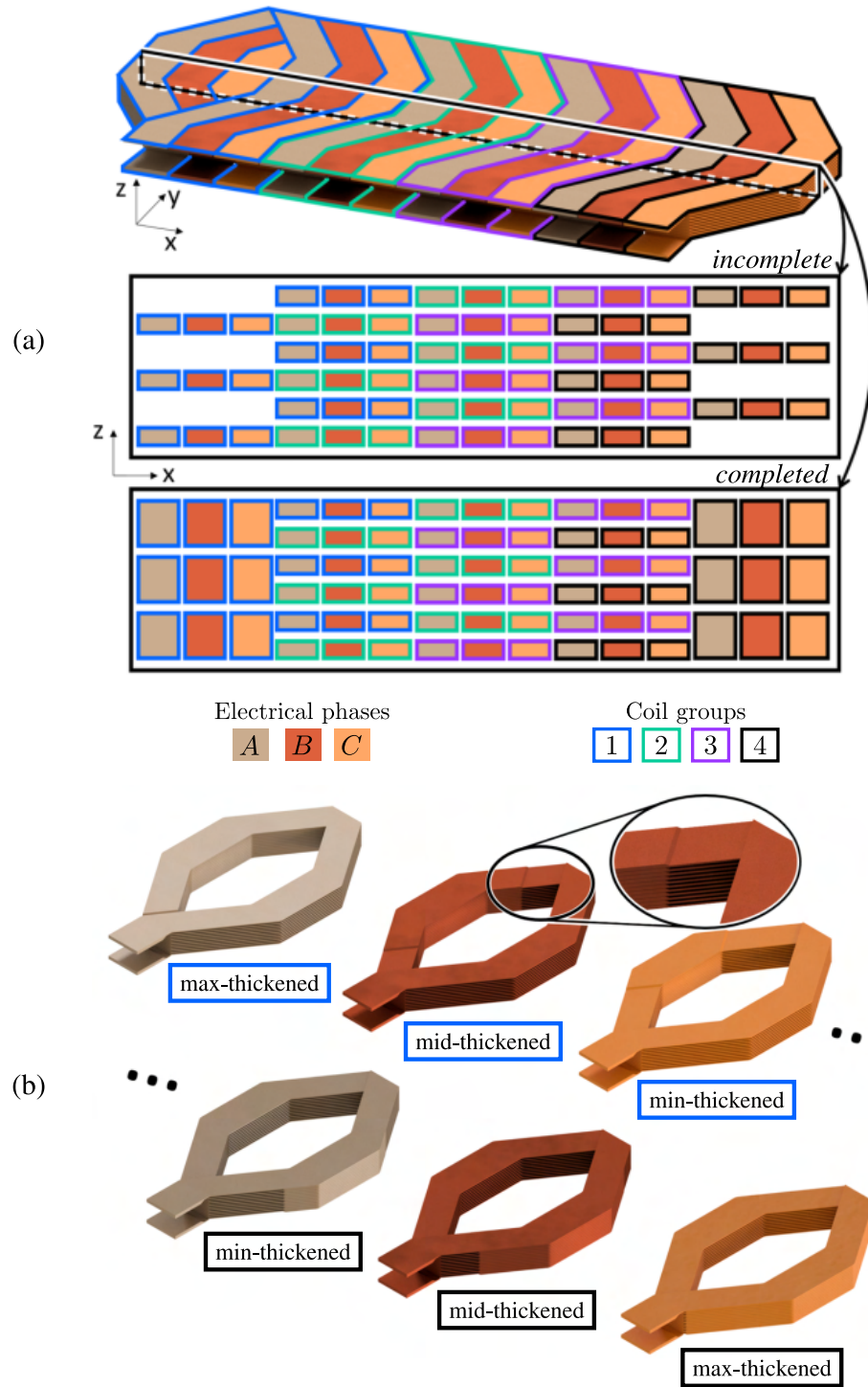


Figure 4.6: Extension of the thickness of the tracks to complete the overlapping winding of linear motors: (a) concept with only 3 turns per coil for showcase, (b) modified (thickened) coils to complete the rest of the winding made of non-thickened coils. Figure reused from [135]. ©2022 IEEE.

Table 4.1: Simulated resistance R and relative change r of the different types of coil with *out-of-plane* distributed turns in a *completed* winding made of pure copper. Table reused from [135]. ©2022 IEEE.

	Resistance [$m\Omega$]	Relative change [%]
Non-thickened	9.53	0.0
Min-thickened	8.56	-10.2
Mid-Thickened	7.84	-17.8
Max-Thickened	7.12	-25.3

The local extensions of the tracks' thickness result in coils with different shapes depending on their position within the winding. Three coils at each border are affected as shown in Fig. 4.6b. They are named: max-, mid-, and min-thickened coils depending on the proportion of their path that has been thickened. As the cross-section locally varies, the different coils have different resistances² which are summarized in Table 4.1. The values are small compared to conventional winding because of the small number of turns, resulting in relatively large cross-sections and, thus, small resistances. This change in coil resistance between the groups affects the total phase resistance, potentially creating an electrical imbalance between the phases. Indeed, two of the three phases are composed of the same coil types, but the third differs, affecting their total resistances. For this work, each phase comprises $C_{pp} = 4$ coils (i.e. number of coil groups) connected in series. Phase A and C both have: one max-thickened coil, two non-thickened ones, and one min-thickened. However, phase (B), physically placed between the two others, will have: two non-thickened coils and two mid-thickened coils. The corresponding phase resistances are formulated as follows:

$$R_{\text{phase}}^A = R_{\text{phase}}^C = R_{\text{phase}}^{A,C} = R^{\text{max-thick}} + (C_{pp} - 2)R + R^{\text{min-thick}} \quad (4.1)$$

$$R_{\text{phase}}^B = (C_{pp} - 2)R + 2R^{\text{mid-thick}}, \quad (4.2)$$

with R , $R^{\text{max-thick}}$, $R^{\text{mid-thick}}$, $R^{\text{min-thick}}$ the resistance of a non-, max-, mid- and min-thickened coil respectively. Each coil resistance can be defined as a function of the non-thickened one R and their relative change r listed in Table 4.1:

$$R^{i\text{-thick}} = R(1 + r^{i\text{-thick}}), \quad \text{with } i \in \{\text{min}, \text{mid}, \text{max}\}. \quad (4.3)$$

Electrical balance between the phases can be assured if $R_{\text{phase}}^{A,C} = R_{\text{phase}}^B$. However, in practice, a small unbalance is acceptable to not affect the control, resulting in the following condition: $(R_{\text{phase}}^{A,C} - R_{\text{phase}}^B) / R_{\text{phase}}^{A,C} < \varepsilon_R$, with ε_R a small tolerance³. It can be reformulated as:

$$r^{\text{max-thick}} + r^{\text{min-thick}} - 2(1 + \varepsilon_R) \cdot r^{\text{mid-thick}} < \varepsilon_R \cdot C_{pp} \quad (4.4)$$

The arrangement studied in this work assumes at least two coils per phase, which satisfies (4.4) considering the relative changes from Table 4.1. Nonetheless, suppose one desires to

²The inductances are unaffected because the mean path described by the current loops stays the same.

³A value of $\varepsilon_R = 5\%$ is considered reasonable for motor control and the dedicated electronics.

apply this concept to another winding topology (or to one with a different aspect ratio). In that case, attention should be put on the relative changes of the coil resistances $r^{i\text{-thick}}$ and the number of coils per phase.

The proposed winding comprises 12 coils, among which 6 are non-thickened, and 6 are thickened (2 trios of max-, mid-, and min-). The total decrease of the phase resistance of the *completed* linear winding from the *incomplete* one is $\Delta R_{\text{phase}} = -8.91\%$. This value is assumed to be equal between all the phases because the difference is negligible in this case. Such an improvement would not have been possible without using additive manufacturing technologies. Indeed, as the cross-section of the tracks constituting the coils evolves along their path, it cannot be easily manufactured with conventional technologies (even PCB ones). This reinforces the interest in such techniques for manufacturing high-performance electrical machines.

4.2.3 Multi-functional winding

This last strategy presents the possibility of integrating multiple functions of the electromagnetic system into a single component thanks to the design freedom provided by AM. In this work, we propose to combine the electromagnetic coil used to drive the motor, with the heat guides or heat sinks, cooling down the winding and enabling better heat dissipation. This leads to electrical machines with higher power density without the need for an additional cooling system and without increasing the volume of permanent magnets. The presented concept is shown on coils with *out-of-plane* distributed turns, but the same idea stays valid for coils with *in-plane* distributed turns. The importance of great heat dissipation in electric motors is first presented. The chosen method achieving such a goal is then described. Finally, the reference and novel winding thermal properties are studied and compared.

4.2.3.a Extract the heat directly from the source

In order to prevent such failures, either the generated heat has to be limited (assuming only Joule losses, this results in the limitation of the input current), or the cooling properties have to be improved⁴. As many electromagnetic devices strive for larger power density, increasing the input current magnitude is appealing, which leads us to improve the heat dissipation properties. It is more effective to extract the heat directly from the source and not from other pieces that may be in contact with it. Hollow conductors with in-wire cooling are a good alternative for large machines with a strong operating mode but degrade the fill-factor for smaller machines with high dynamics. A strategy conserving a good fill factor is to increase the length of the wire constituting the coil to better couple it with a cooling system in the end-winding [137, 138]. However, such a method increases the initial phase resistance at room temperature, which has to be further compensated by the chosen cooling system.

In this thesis, we propose extending the coil's head in the end-winding to form heat sinks directly within the coil as shown in Fig. 4.7. This creates a multi-functional winding. It achieves its electromagnetic purpose as well as cooling itself down. With the proposed method, natural

⁴As mentioned earlier, the resistivity and thus the Joule losses also depend on the temperature. If the heat dissipation properties are improved, the heat generation will also be reduced for the same input current.

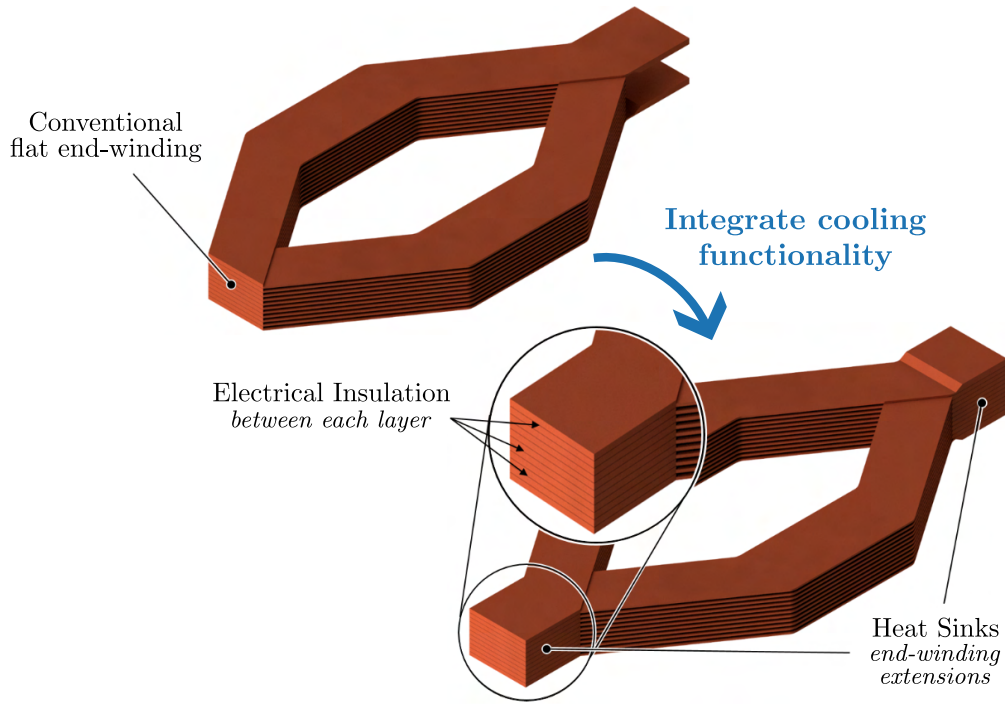


Figure 4.7: Single-functional (top) and multi-functional (bottom) coil with integrated heat sinks. Figure reused from [135]. ©2022 IEEE.

or forced cooling better guides the heat to the environment. The heat is directly extracted from within the source without intermediate media. This solution does not affect the effective length traveled by the electric current. The increased cross-section of the coil head has a negligible effect on the current flow because the extension is normal to its direction. Thus the proposed end-winding extension has no effect on the resistance of the coils (even at room temperature). It is confirmed in Fig. 4.8 where the electric potential distributions of the single- and multi-functional coils are compared. One can see that the coil head is a floating electric potential that is not affected when extended as proposed. Each extension must be electrically insulated to prevent short circuits between the different turns and keep the electric potential floating in the coil head. Naturally, the proposed system partially increases the device's footprint like any other cooling system. Nonetheless, the proposed method will be more compact and efficient than state-of-the-art ones due to the absence of intermediate pieces or media. The resulting heat sink has a length of 10 mm, increasing the winding y-footprint by +13% while keeping the other ones constant. The expected better heat dissipation will allow a larger operating current and, thus, a larger power density for the same volume of permanent magnets.

Through the proposed extension, the end-winding, usually identified as the weak spot of coreless machines (because it does not contribute to the force generation), is actually used as a heat sink cooling down the whole winding. Natural convection cooling is assumed here, but the concept can extend to a forced cooling system. As the design of heat sinks is a widely investigated topic [139, 140], their design is beyond the scope of this work. A simple straight extension of the coil head has been performed so as to still fit the machine of interest.

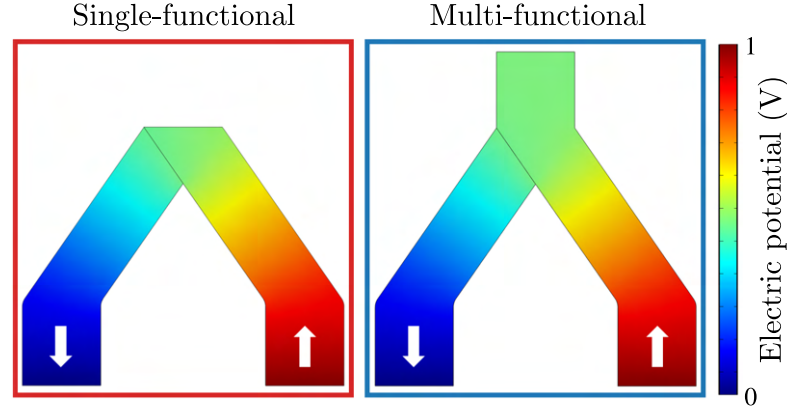


Figure 4.8: Simulated electric potential distribution resulting from a voltage drop applied over half a turn. The magnitude has been normalized for better representation. The white arrows indicate the current direction. Figure reused from [135]. ©2022 IEEE.

Nonetheless, other designs are shortly discussed in the perspectives in Section 5.2.

4.2.3.b Thermal properties

The thermal properties could have been modeled and studied based on analytical modeling as recently suggested for PCB windings [141]. However, we opted for finite element simulations to get a more comprehensive understanding. The problem set-up is shown in Fig. 4.9, and the material properties considered in the simulations are shown in Table 4.2. A linearized resistivity conduction model performs non-linear coupling between the two. It links the material electrical conductivity σ with the temperature T :

$$\sigma(T) = \frac{1}{\rho_0^{\text{elec}} (1 + \alpha(T - T_{\text{ref}}))}, \quad (4.5)$$

with ρ_0^{elec} the reference resistivity, α a resistivity temperature coefficient, and T_{ref} the reference temperature set to 20°C.

Only half of the winding is considered because of symmetry. The housing size is fixed with respect to the footprint of the multi-functional winding for a fair comparison. The two windings are in an *incomplete* configuration to show that the two innovations proposed in this chapter do not depend on each other. A fixed input current density is imposed on the cross-section of one end of each turn while the other is grounded. The symmetry is imposed by forcing the heat flow \mathbf{q} to be perpendicular to \mathbf{n} , the vector normal to the symmetric plane: $-\mathbf{n} \cdot \mathbf{q} = 0$. A convective heat flux boundary condition is only applied to the five external surfaces of the winding housing: $\mathbf{q}_0 = h(T - T_{\text{ext}})$, with a heat transfer coefficient set to $h = 7 \text{ W/(m}^2\text{K)}$ to approximate natural convection conditions [142]. The external temperature T_{ext} is set to the reference one T_{ref} . As already introduced, the problem is multi-physic, resulting in a non-linear analysis with dependencies between the two physics. Electric conduction is solved with:

$$\mathbf{E} = -\nabla U; \quad \mathbf{J} = \sigma(T)\mathbf{E}, \quad (4.6)$$

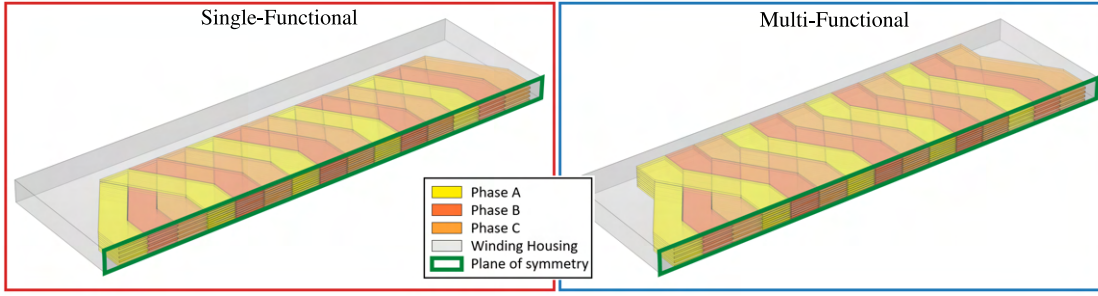


Figure 4.9: Set-up of the winding for the multi-physics simulation. Only one-half is used because of symmetry. A convective heat flux boundary condition is only applied to the five external surfaces of the winding housing. The chosen heat transfer coefficient is set to $h = 7$ $[W/(m^2K)]$ to represent the natural convection cooling. Figure reused from [135]. ©2022 IEEE.

with U the electric potential, E the electric field and J the current density. The heat generated by the current flow can be expressed as Joule losses Q :

$$Q = J \cdot E. \quad (4.7)$$

First, a stationary analysis is performed. The winding is assumed static, so Poisson's equation governs the heat transfer:

$$\nabla \cdot \mathbf{q} = Q, \quad (4.8)$$

with \mathbf{q} the resulting heat flow defined as:

$$\mathbf{q} = -k \nabla T, \quad (4.9)$$

considering k the thermal conductivity. The effect of the motion of the winding on the cooling properties is beyond the scope of this work. The stationary temperature of any point inside the mesh can be determined after several iterations of the non-linear solver.

The simulations are performed with the commercial software COMSOL[®]. Joule heating, described by the above equations, is simulated by coupling an ELECTRIC CURRENT with a HEAT TRANSFER IN SOLID physic interface. Multiple analyses have been performed comparing the single and multi-functional winding for different conductive and housing materials. Fig. 4.10a shows the maximal stationary temperature over the winding, obtained for different input current densities assuming no housing (air). One can see that the multi-functional winding heats less than the single-functional one. The simulations are not performed for large values of input current density because the temperature would increase too much, invalidating the linearized resistivity conduction model defined in (4.5) and resulting in divergence of the solver. In order to extract quantitative information from these simulations, it has been decided to compare the maximal critical input current J_{crit} reaching the critical temperature T_{crit} ; as well as the stationary temperature resulting from a constant nominal input current density $J_0 = 3.2 \text{ A/mm}^2$. The critical temperature is chosen as $T_{\text{crit}} = 130^\circ\text{C}$ to prevent degrading the winding lifetime, assuming a common Class-H type of electrical insulation. J_{crit} is defined for DC operation. The input current density can go beyond this value for a short time. It

4.2 Harvesting the design freedom provided by additive manufacturing

Table 4.2: Material properties used for simulations. Table reused from [135]. ©2023 IEEE.

	Copper	Aluminum	Parylene	Air
Electrical conductivity $\sigma [MS/m]$	59.98	37.74	-	-
Mass density $\rho_{\text{mass}} [g/cm^3]$	8.96	2.70	1.11	0.0012
Mass conductivity $\zeta [S.m^2/g]$	6.69	13.98	-	-
Thermal conductivity $k [W/(m.K)]$	400	238	0.09	0.02
Heat capacity $C [J/(kg.K)]$	385	900	711.8	1012
Reference resistivity (at 20°C) $\rho_0^{\text{elec}} [\mu\Omega.mm]$	17.2	26.5	-	-
Resistivity temperature coefficient $\alpha [1/K]$	0.0039	0.00429	-	-

Table 4.3: Results of the thermal simulations for various winding and housing materials, comparing the single- and multi-functional winding types.

Housing type		Parylene		No Housing (air)	
Winding functionality		Single	Multi	Single	Multi
J_{crit} [A/mm ²]	Cu	4.03	4.46 (+10.7%)	3.73	4.18 (+12.0%)
	Al	3.20	3.46 (+7.8%)	3.01	3.27 (+8.6%)
T_{stat} [°C] at J_0	Cu	81.1	68.5 (−15.6%)	95.3	77.5 (−18.7%)
	Al	135.7	108.5 (−20.0%)	165.3	125.7 (−24.0%)

is used here as a comparison point⁵. The different simulation results are summarized in Table 4.3. Despite having the same room temperature resistance, it can be seen that multi-functional windings perform better than single-functional ones. The maximal input current density can be increased up to +12% in the multi-functional case compared to the single one. This means that a force 12% larger can be expected for the same permanent magnet volume. This improvement of heat dissipation properties is confirmed by the stationary temperature attained for a fixed nominal input current density J_0 . A decrease of temperature down to −20% can be achieved by the multi-functional winding compared to the single-functional. We can conclude that the multi-functional system has better dissipation properties without an additional cooling system and can be described as *self-cooling winding* due to its integrated heat sinks.

⁵In any case, if a configuration has a larger J_{crit} , larger input current densities can be applied for transient operation.

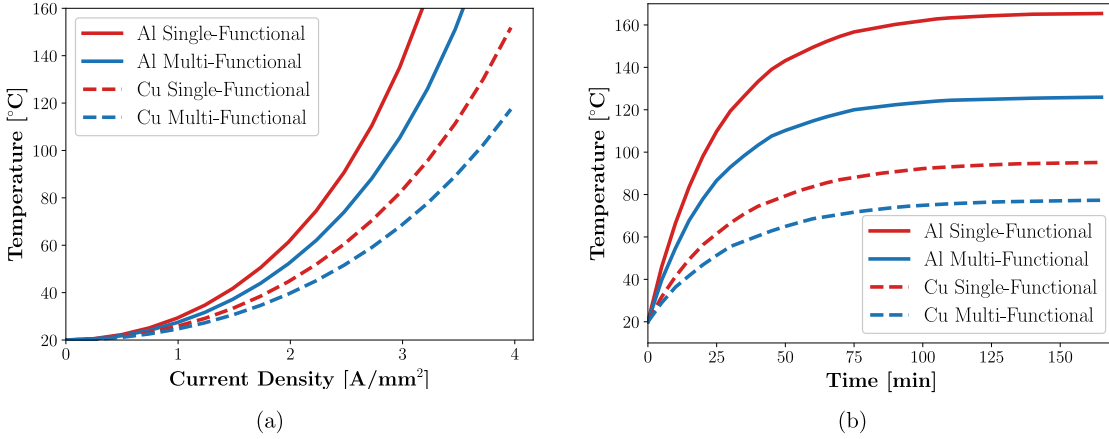


Figure 4.10: Results from multi-physics simulations for different conductor materials without housing (air): (a) dependency of stationary temperature with input current density; and (b) transient temperature increase at $J_0 = 3.2 \text{ A/mm}^2$. Figure reused from [135].

An additional analysis is performed to study the transient behavior of this cooling. The input current density is kept constant (DC analysis), and the winding is mechanically static. For a transient thermal analysis, (4.8) becomes:

$$\rho^{\text{mass}} C \frac{dT}{dt} + \nabla \cdot \mathbf{q} = Q, \quad (4.10)$$

with C the heat capacity, and t the time. Fig. 4.10b shows the transient temperature increase of the single- and the multi-functional windings assuming no housing (air). A linear regression can be performed to fit the following equation so as to extract the system time constant:

$$T(t) = T_{\text{stat}} \cdot \left(1 - \exp(-t/\tau)\right), \quad (4.11)$$

with T_{stat} the stationary temperature and τ the time constant. In all cases, the time constant is $\tau \approx 30 \text{ min}$ expressing no difference between the windings in a mechanically static operation. The modified geometry of the winding is expected to affect the time constant in a dynamic configuration with moving winding. Such a phenomenon is beyond the scope of this work.

4.2.4 Conclusion

This part investigates different possibilities for improving electromagnetic devices through novel winding designs to be additively manufactured. The first proposed strategy is to opt for coils made of turns with varying cross-sections. It achieves better packing of the different turns and reduces the coil's resistance through an increased fill-factor. Then, the same idea is further harvested for windings in linear motors. Compared to the unfolded rotating version, the concept of a *completed* winding is proposed to fill the empty space left at its borders. This simple change permits an additional reduction of the phase resistance by almost 9% for the machine of interest.

Finally, it is proposed to combine two sub-functionalities of the electric motor: the generation

of the electromagnetic force driving the motor, with the system responsible for dissipating the generated heat, into a single component. This results in a novel multi-functional winding with integrated heat sinks, achieving self-cooling capabilities. This approach is demonstrated by considering a straight extension of the coil head forming the integrated heat sinks. This simple geometry enables a proof of concept, but more advanced ones could be investigated to push even further the performance. As additive manufacturing provides great freedom in the design process, the geometry of these extensions could be further optimized to better accommodate specific forced cooling systems.

Nevertheless, the proposed idea enables a significant increase up to +12% of the electric current input to the machine. The same improvement of output force is expected (if no saturation effects) for a fixed amount of permanent magnet. This work is showcased on a linear machine with natural convection cooling, but the proposed concepts can easily be extended to other types of machines and cooling systems. In most motors, the end-winding is a weak spot that can be extended to better exchange heat with the environment or a specific cooling system.

If the concepts of *completed* linear winding and multi-functional coils were to be combined, the maximal input current is expected to be increased even further. Indeed, let us consider a fixed amount of Joule losses that the multi-functional winding can dissipate before reaching the critical temperature. Then, the corresponding maximal current could be increased by +4.8% to keep the product RI^2 constant in a *completed* linear winding. This results in a total output force increase of +17.3% with respect to the *uncompleted* and single-functional winding. This important improvement demonstrates the potential of additively manufactured windings for the next generation of cutting-edge electromagnetic devices.

Publication related to this chapter:

G. Burnand, A. Thabuis, D. M. Araujo and Y. Perriard, "Novel Optimized Shape and Topology for Slotless Windings in BLDC Machines," in IEEE Transactions on Industry Applications, vol. 56, no. 2, pp. 1275-1283, March-April 2020, doi: 10.1109/TIA.2019.2956717, [18].

A. Thabuis, X. Ren, and Y. Perriard, "Enhanced Electric Motors using Multi-Functional 3D Printed Winding with Integrated Heat Sinks," in IEEE Transactions on Energy Conversion, 2022, doi: 10.1109/TEC.2022.3221189, [135].

X. Ren, A. Thabuis and Y. Perriard, "Innovative Design of 3D-printed Winding for Linear Motor," 2022 25th International Conference on Electrical Machines and Systems (ICEMS), 2022, pp. 1-6, doi: 10.1109/ICEMS56177.2022.9982962, [143].

4.3 Experiments



ADDITIVE manufacturing (AM) specifically applied to fabricating electromagnetic coils is a recent alternative only lightly documented in the literature. This section presents the general fabrication method and covers the challenges and solutions specific to the coil shapes. Some of the lessons learned throughout this thesis are also revisited here. A working electromagnetic coil requires a combination of two materials: one for the tracks conducting electricity (metal) and another for electrically insulating and protecting the tracks (polymer or ceramic). Despite recent advances in the field [144, 145, 146], AM of multiple materials with different natures is still in its early stages with limited performances⁶, the fabrication of working coils is divided into two parts: the printing process and the post-processing steps, such as the electrical insulation of the tracks. Finally, some tests are performed to characterize the electromagnetic and thermal properties of the fabricated coils.

4.3.1 Printing process

4.3.1.a Materials and methods

AM of metals has been largely developed in the last years mainly for structural mechanics purposes. More recently, 3D printing of highly conductive (electrically and thermally) materials like silver, gold, aluminum, or copper has been investigated, providing additional functionalities to AM pieces in electronics and thermal management. Despite being described as achieving parts with *limitless* complexity, AM still has a few limitations depending on the material and method used to print. The first methods initially developed for manufacturing pieces made of polymers like the Fused Filament Fabrication (FFF), SLA or material jetting have been modified to fabricate metallic pieces [147, 89]. It often relies on combining metallic particles with a binder for printing, which can be removed (or not) in a post-processing step. However, these methods rarely achieve a high volumetric metal density inside the resulting part. That is why powder fusion technology such as SLS is often preferred for such materials as it can achieve highly dense and conductive metallic parts. Its principle is illustrated in Fig. 4.11a. A laser fuses material particles together, layer by layer, to create a solid object. The process begins by spreading a thin layer of fine powder material on a build platform. A laser scans the surface of the powder, selectively fusing the particles together in the desired shape of the object. The build platform is then lowered, and another layer of powder is spread on top of the previous layer. The process is repeated until the workpiece is completed.

The different AM methods all fabricate the part layer by layer, thus sharing common design limitations. Some of them are presented in Fig. 4.11b. The well-known *wall thickness* and maximal *overhang angle* must be considered for any piece to print. The minimal *wall thickness* is related to the maximal resolution a feature inside the piece can get, and the *overhang angle* is the angle to the vertical (standing) axis. A piece cannot have this angle too large for a too-large length; otherwise, some supports will be required to prevent the part from falling

⁶The resolution and aspect ratio of the different materials are still of the same order of magnitude. However, electromagnetic coils should extensively be composed of conducting material and only covered by a thin layer of insulating materials.

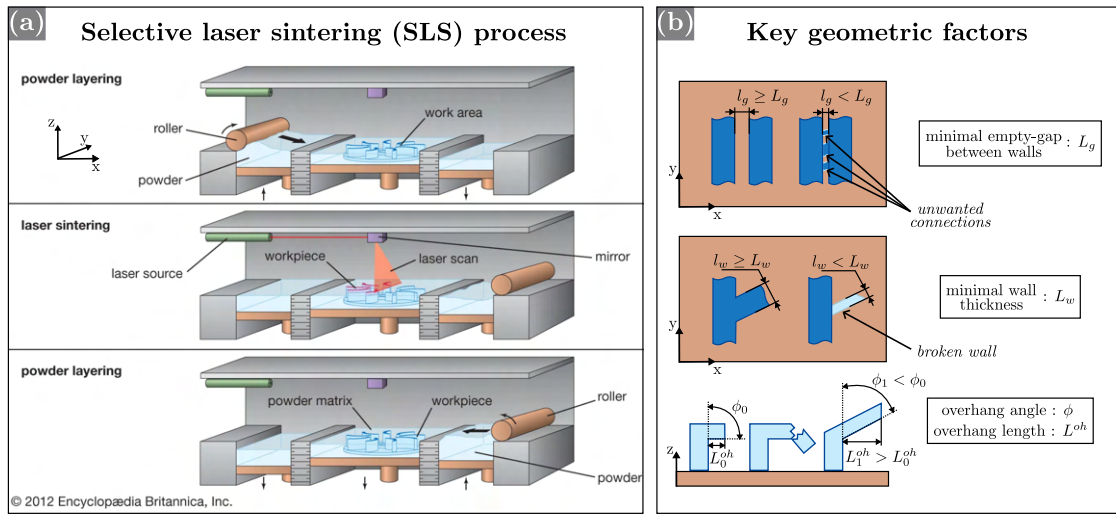


Figure 4.11: Additive manufacturing: (a) Illustration of the selective laser sintering (SLS) process [148]; and (b) key geometric factors to consider for AM.

off (because of gravity). Recent development in the slicing technology, determining the ideal path taken by the laser or the extruding nozzle at each layer, exhibited parts with no almost overhang limitations removing possible needs for supports [133]. The presence of supports is not an issue by itself but requires some post-processing to remove them. The supports are also wasted materials as it is not directly used to compose the piece. However, material waste is tremendously lower for additively manufactured parts than with subtractive methods. Generally, the piece's orientation to print is determined to minimize the *overhang angles* and the number of supports. It is also preferred to have supports directly connected to the build-plate because they are easier to remove than the ones possibly connecting different parts within the structure. Additional factors must be considered when printing complex parts such as a coil. The thin nature of the turns covering a wide area imposes large *aspect-ratio* within the structure to fabricate. It can be an issue when additively manufacturing such pieces because they are more likely to have position fluctuations (due to irregular forces or heat distribution across the piece), resulting in degraded tolerances and possible breaking of the part. Furthermore, the minimal *empty-gap between walls* is also important because it corresponds to the minimal length between two walls that can be assured without unwanted connections. Indeed, the printing process induces thermally affected regions larger than the nozzle or laser point because heat partially conducts within the powder and part. Thus, these regions can be partially sintered, creating unwanted connections between different parts of the structure. The important factors are listed below and briefly discussed specifically to the design of coils:

- the minimal *wall thickness* corresponds to the smallest structural feature size. This affects a turn's minimal size/thickness and limits the maximal number of turns constituting a coil with a fixed footprint.
- the *aspect-ratio* generally refers to the ratio between a wall's height and thickness. A thin wall cannot be too high to ensure proper printing. It can be improved by adding supports

connected to the walls, improving the effective stiffness of the printed structure.

- the minimal *empty-gap between walls* corresponds to the minimal length that can be assured between two walls without unwanted connections. This is critical for electromagnetic coils (as opposed to general structural mechanics) because unwanted connections may result in short circuits between the turns that constitute the printed coil. It indirectly affects the fill factor of the resulting winding⁷. Indeed, the empty-gaps between walls/turns will be filled with insulation and not active material.

These parameters differ depending on the selected material and printed method. The SLS method achieves the best performances for pure metals. Considering costs and manufacturing feasibility, two principal materials stand out: copper and aluminum. Despite often being alloyed with other materials to ease the print, these two provide interesting geometric specifications with large electrical conductivity. An extensive comparison between them is provided in [95]. Generally, while pieces printed in copper alloy exhibit better electric and thermal properties, aluminum ones are lighters. They can also be composed of features with smaller sizes, such as the minimal *wall thickness* and minimal *empty-gap* length. The high reflectivity and thermal conductivity of copper can explain this. Indeed, it requires a more powerful laser and longer exposure time to sinter the powder to stay in the conduction regime. This affects the minimal *wall thickness*, *empty-gap* lengths achievable by the printing process, as well as the roughness of the piece [149, 150, 151].

4.3.1.b Fabricated coils

In this work, the printed winding is integrated into a coreless machine only driven by the Lorentz force. For a fixed electromagnetic potential, coils with a large number of turns are preferred to prevent significant heat. Furthermore, the current AM technology can not achieve the same minimal feature size as the mature wire technology. Hence, considering the portfolio of different manufacturers, a specific aluminum alloy achieving small feature sizes is chosen for the proof-of-concept. It allows the manufacture of coils with a maximal number of turns at the scale of interest. The different coils were fabricated at the CSEM (Swiss Center for Electronics and Microtechnology) in the aluminum alloy AlSi12 with the SLS technology. The printing process (scanning speed, laser power, etc) developed in this center achieves the following sizes:

- minimal *wall thickness*: 300 μm for large aspect ratio, and 150 μm for smaller aspect ratio. The machine could go down to 100 μm with more tuning of the parameters.
- minimal *empty-gap* between turns: 120 μm .
- built-in chamber size: diameter of 100 mm for a height of 80-90 mm.

⁷This empty-gap between walls/turns can be artificially reduced in the final part. It can first be increased while printing and reduced after the print by compressing the piece in order to keep a competitive fill-factor. It is straightforward for coils with *out-of-plane* distributed turns but possibly not feasible for coils with *in-plane* distributed turns.

The position and orientation of the pieces to print naturally depend on their geometry. The turns distributed *in-plane* for the first coil type require the piece to be printed flat onto the build-plate. This prevents the different turns from fusing together or the need for supports in between them. Similarly, the turns distributed *out-of-plane* for the second coil type require the piece to be printed standing up onto the build-plate for the same reasons. An important aspect to consider is that the minimal empty-gap length between printed walls l_g is larger than the minimal insulation thickness to be later applied to the coil. It means that the gaps between turns must be increased to be printed correctly, resulting in coils with poor fill-factor. However, this limitation can be alleviated for the coil with *out-of-plane* distributed turns. Indeed, the coil can be "elongated" similarly to pulling a traction spring to increase the empty-space between the turns when printing. The insulated coil is later compressed back when integrated into the motor. It prevents the turns from fusing together when additively fabricated while assuring a large fill-factor of the insulated coil. It is illustrated in Fig. 4.12 with an exaggerated elongation for clarity. Considering the size of the build chamber of the manufacturer, only two coils with *in-plane* turns can be manufactured at once, while seven coils with *out-of-plane* turns can be manufactured at once. It shows a first manufacturing advantage for the *out-of-plane* type. The manufacturer adds supports to ensure proper positioning of the long turns with a large aspect ratio. Indeed, these pieces do not have excellent structural stability and are subject to uneven heat distribution within the chamber (hotter close to the laser and colder elsewhere). This induces possible position fluctuation of the already printed features preventing a correct printing of the following layers if not supported by an additional rigid structure.

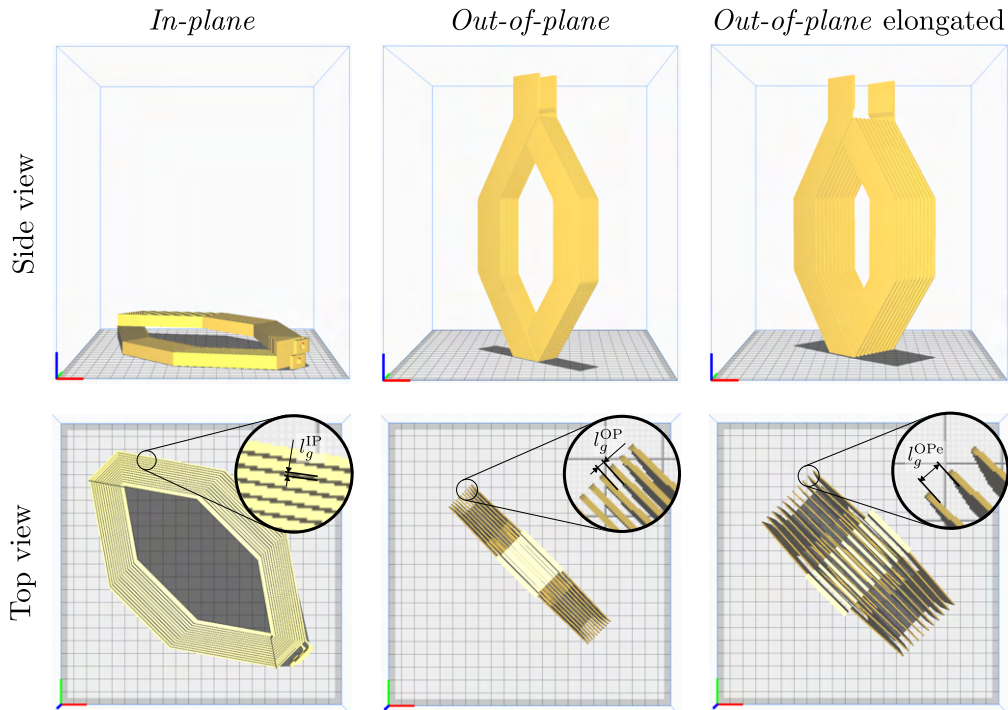


Figure 4.12: Printing orientation of the different coil types with elongated version increasing the empty gap length between turns. The size of the depicted build-chamber differs from the one used for manufacturing. The supports are also not shown here.

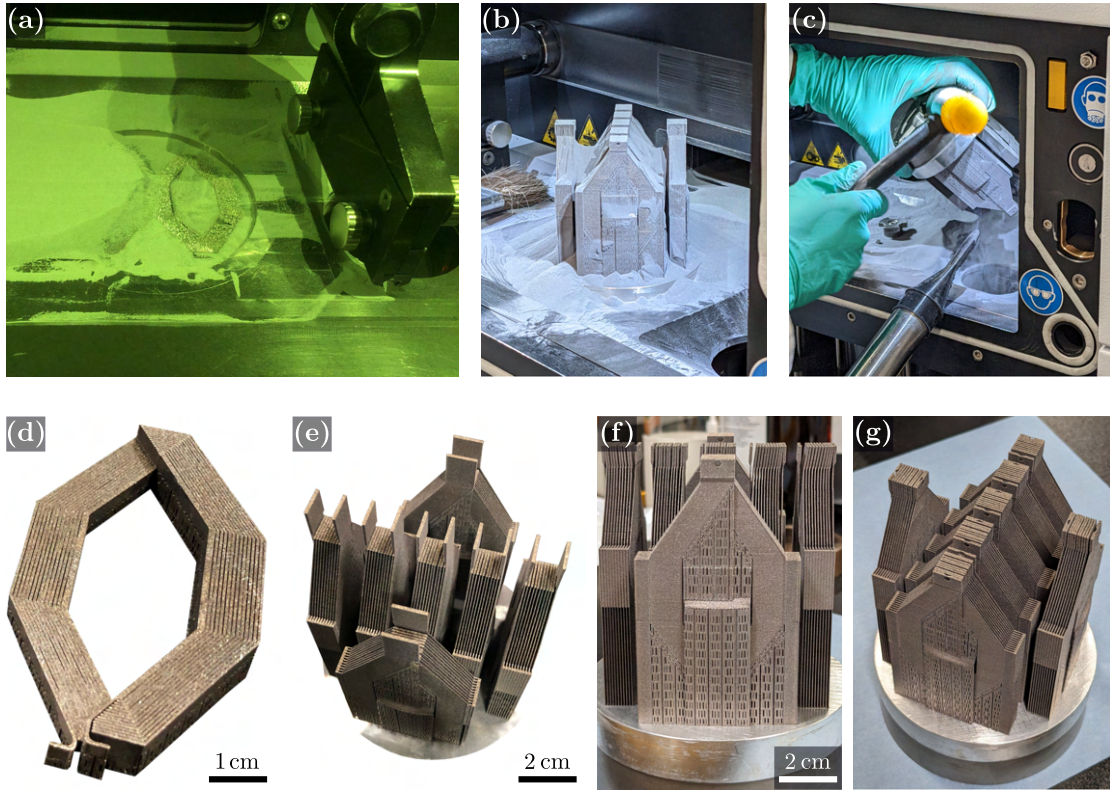


Figure 4.13: Printed coils: (a) *in-plane* types inside the printer; (b) *out-of-plane* types outside the powder bed; (c) removal of excess powder stuck between the pieces; resulting pieces with supports after powder removal for the (d) *in-plane* type, (e) *out-of-plane* types, and (f-g) *out-of-plane* with integrated heat sinks types.

Based on the sizes achievable by the manufacturer and the orientation of the pieces, the *in-plane* type has a track width of $150\ \mu\text{m}$, a length between turns of $130\ \mu\text{m}$ (i.e. minimal empty-gap between walls with a small margin), resulting in a coil constituted of 14 turns. 15 turns were originally planned, but the thin nature of the turns made the inner one break at the sharp angle of the *diamond* shape. Thus, the two inner turns have been combined into a thicker one. The *out-of-plane* type has a track width of $300\ \mu\text{m}$ (due to its large height inside the chamber), and a length between turns of $600\ \mu\text{m}$, resulting in a coil made of 11 turns. It took 42 hours to print 7 multi-functional coils with *out-of-plane* distributed turns. The process is expected to be much faster on a machine dedicated to an industrial scale once the printing parameters are optimized.

Once printed, the unfused powder inside the chamber is removed and recycled for later prints. Some remaining powder is likely stuck between the different pieces and between the different constituting features and supports. The build-plate with the pieces mounted onto it is removed from its piston and gently shaken with a hammer to detach a maximum amount of remaining powder. It is illustrated in Fig. 4.13 next to multiple pictures of the different printed coils.

4.3.2 Post-processing of the coils

4.3.2.a Heat treatment

An important part to consider when printing conductive materials is the effective conductivity of the pieces. Indeed, the performances after printing are lower than the bulk material and depend on the printing direction. It is discussed in detail by Wu and colleagues in [95]. The researchers showed that the electrical conductivity was higher parallel to the building direction, reinforcing the interest in printing the coils "standing-up" like for the *out-of-plane* type. Nevertheless, heat treatments are often applied post-printing to the pieces in order to improve the effective material properties. The researchers suggest a T6 heat treatment to reduce the orientation dependency and increase the effective conductivity. In the case of the considered coils, the manufacturer assured an effective electrical conductivity of $\sigma = 15.38 \text{ MS/m}$, corresponding to 70% of a reference die cast *AlSi12* (norm EN AC-44300) with conductivity $\sigma_{\text{ref}} = 22 \text{ MS/m}$ [152]. The company already performed a heat treatment before removing the supports in order to reduce residual stresses within the structure. The pieces were put in an oven at 200°C for 30 minutes. It had the effect of partially increasing the effective conductivity to 16 MS/m . Once the manufacturing supports were removed from the parts, the pieces were slightly deformed due to the residual stresses within the structure. This results in unaligned turns. The coils were thus mounted on a realigning structure in steel, forcing the turns to be aligned, and soft annealed in an oven for 4 hours at 400°C . It is shown in Fig. 4.14. The pieces had a slightly different color than before while regaining their correct shape and increasing their electrical conductivity to $\sigma_{\text{proto}} = 25.19 \text{ MS/m}$. This corresponds to 114% of the conductivity of the reference alloy and 66.7% of pure aluminum. Such an improvement is possible because a specific alloy was considered. For pure materials, it is impossible to go beyond their annealed version's conductivity. It has been shown in the literature that electrical conductivity as high as 97% IACS (International Annealed Copper Standard) could be achieved for additively manufactured copper (after post-process heat treatment) [94], which is promising for printed windings in the future. The *realigning* step could be removed for the next iterations with a better design of the printing supports and an improved printing process (laser intensity, scanning speed ...). However, a heat treatment will likely always be carried out to improve the effective conductivity.

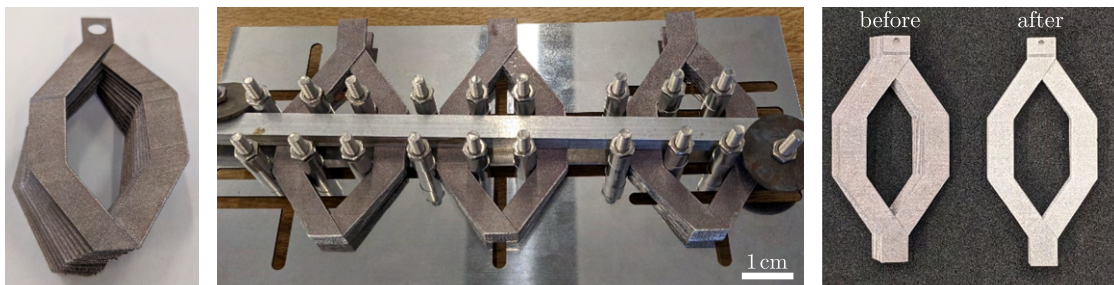


Figure 4.14: Realignment of the coils: (left) deformed coil with misaligned turns after supports removal, (center) realignment set-up to be placed in the oven, (right) comparison before and after the heat treatment for the coils with integrated heat sinks.

4.3.2.b Connections

The electrical connections between the different coils or the power supply are conventionally performed by soldering copper wires. However, in the case of coils made of aluminum, this is more complicated. Indeed, an oxide layer that immediately forms at the surface of the piece, even when scratched, prevents conventional electrical soldering. Various soldering methods exist, such as spot welding, clinching, or ultrasonic welding, but they ensure irreversible mechanical connections. Other dismountable methods are preferred for prototyping reasons. Two possibilities have been found in this thesis. The first consists of plating the aluminum pad with copper to perform traditional soldering with copper wires. Electroplating in galvanic baths can be performed in the industry. In this work, a more straightforward approach [153] purely chemical using copper sulfate and salt at room temperature has been undertaken. The second method consists of a simple bolt and screw connection, assuring a mechanical contact between the pads of the coils and crimps connectors into which copper wires are fixed. These are illustrated in Fig. 4.15.

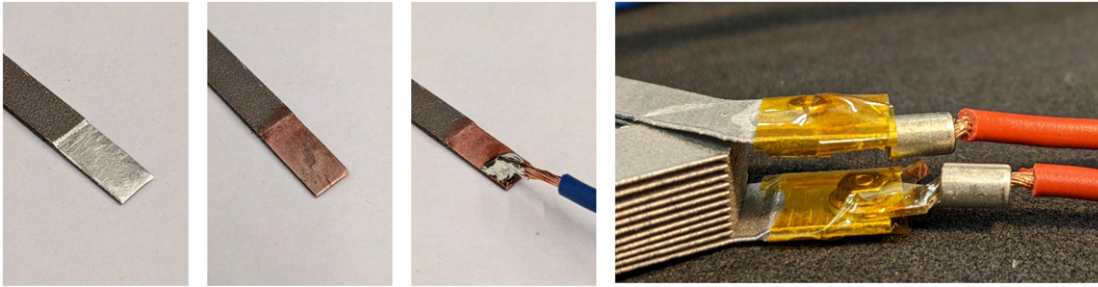


Figure 4.15: Deposition of copper onto aluminum for soldering wires; and mechanical connection of the coils

4.3.2.c Insulation

Electrical insulation is a mandatory step to ensure the proper operation of an electromagnetic coil. Indeed, it prevents short circuits from happening between the turns of the coil itself or with the ones of the other coils constituting the winding. It also protects the tracks in metal from oxidation and corrosion due to the environment. Ideally, this process would be integrated with the printing process of the conducting tracks. Multi-material AM is a promising field expected to improve in the future (to achieve small insulation thickness and thus a large fill-factor). Specific interest is put on machines capable of printing ceramic insulation due to their larger heat conductivity and melting point than traditional polymer-based ones [101]. However, in this work, a polymer-based insulation layer has been applied manually after fabrication and heat treatment of the metallic coils. The first step is to ensure that the different turns do not touch each other to prevent regions from being inaccessible to the insulation coating. As shown in Fig. 4.16 for a coil with *in-plane* distributed turns, the turns are properly spaced when the coil is printed and still maintained by the supports. However, when the supports are removed, the remaining stress within the part and the absence of strong structural stability make the turns deform and move, slightly touching each other. That is why the coil is first mounted onto a bench to manually insert some plastic spacers between each turn,

avoiding short circuits. They are heated up by a hot air gun to partially melt and stay in position. Finally, the coil is impregnated in a transparent varnish to fix in place the whole geometry and cover every part of the metallic tracks. The impregnation varnish PLASTIK 70 from Kontakt Chemie is used here. This insulation of the *in-plane* coil type is long and tedious. For industrial production, other methods should be investigated. A possibility would be to impregnate the coil with supports into the varnish. This would fix the position of the different turns preventing short-circuits but require another insulating layer to be applied once the supports are removed.

Regarding the coils with *out-of-plane* distributed turns, they need to be elongated similarly to a traction spring and mounted onto a rigid support to prevent the different turns from touching. Three different insulation methods have been investigated. The first consists of dipping the elongated sample within the impregnation varnish used for the other coil type, as shown in Fig. 4.17. It was then mounted onto a rotating device to dry the varnish. A particular angle was enforced between the rotating axis and the diamond coil's symmetric axis. This prevents the accumulation of varnish droplets at the edges of the coil when rotated. The coils were immersed into the varnish for 5 minutes and then left on the rotating device for 15 minutes while regularly alternating rotation. It was then suspended onto fixed supports for several

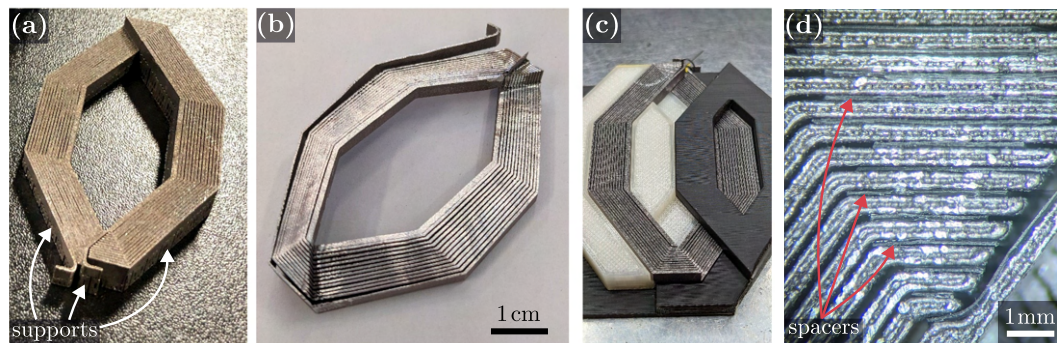


Figure 4.16: Insulation process of a coil with *in-plane* distributed turns: (a) printed coil with supports; (b) coil after support removal; (c) bench maintaining the coil in position, and (d) zoomed view of the coil head with thin plastic spacers placed between the aluminum tracks.

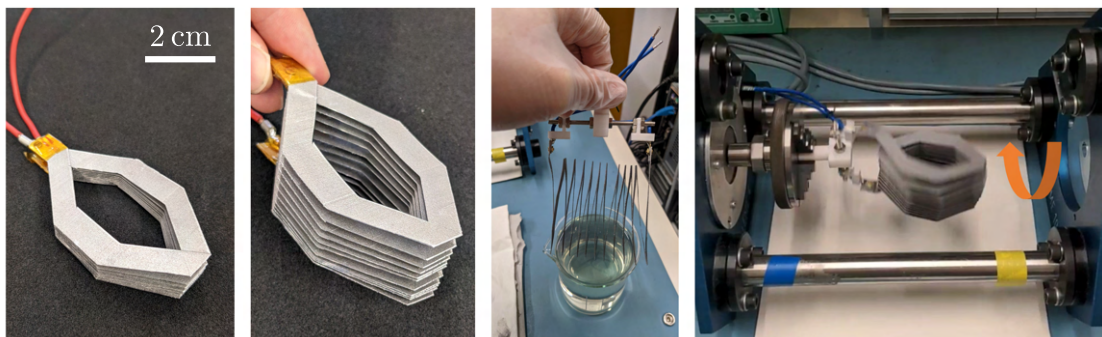


Figure 4.17: Insulating a coil with *out-of-plane* distributed turns by immersion into an impregnating varnish.

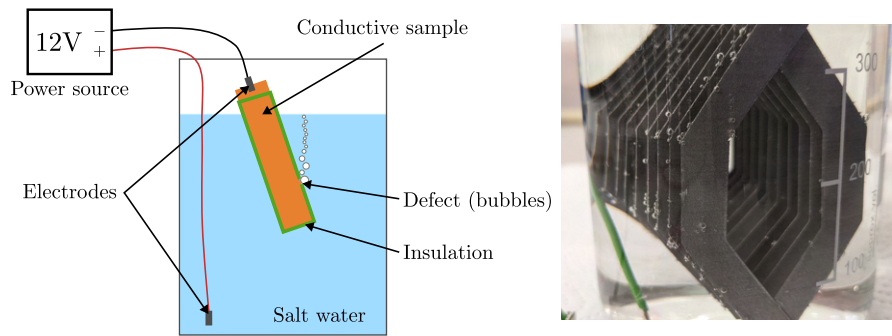


Figure 4.18: Pinhole test for identification of insulation defects: (left) schematic for principle, (right) picture of a coil with many defects for illustration.

hours to finish drying. This process was repeated 3 times to apply multiple layers of varnish and ensure a good coating of every surface and edge. Despite several tests, the deposition thickness is complicated to control with this manual process, but better results could be expected with automated tools. The second method investigated parylene deposition, applied at ambient temperatures with the chemical vapor deposition (CVD) method. A dedicated workshop from EPFL has performed it. After multiple runs, the deposited layer is assured to be $30\text{ }\mu\text{m}$ thick. The last insulation method is the powder coating process consisting of electrostatic spraying charged powder to the elongated pieces. The material used is a black polyamide (PA11) deposited at room temperature. This has been outsourced to a Swiss company named EPOSINT, which assured a deposition thickness between 70 and $130\text{ }\mu\text{m}$. An insulated coil is displayed in Fig. 4.21. The three different methods properly insulate the coils when considering individual pieces. However, this was not always the case after assembly with multiple samples. It is further discussed in Section 4.3.2.d.

The presence of short circuits between turns or coils can easily be determined with a multimeter. However, in the presence of a short circuit, it is not straightforward to determine its exact location. It is proposed here to perform a *pinhole-test* which consists of salt water electrolysis. Despite being initially developed for single copper wire [154], we adapted the same method to a coil with a complex shape. The principle is to place a positive electrode at the bottom of a container filled with water into which some salt has been dissolved. Then, a negative electrode is attached to the coil at a non-insulated part like the connecting pads. The piece is then submerged into the container (except the part connected to the electrode). If the piece is insulated correctly, no electrons will be exchanged between the two electrodes. On the other hand, if there is a defect, free electrons will induce a reaction with the water molecules creating hydrogen gas at the position of the defect. This results in tiny bubbles that can be visually identified as shown in Fig. 4.18.

4.3.2.d Assembly

Once the coils are insulated, they are assembled to form a complete winding. It is straightforward for the coils with *in-plane* distributed turns, but it is more challenging for the ones with *out-of-plane* distributed turns. Indeed, these coils need to be elongated and carefully assembled because of their intertwined turns. The rail shown in Fig. 4.19 permits a proper

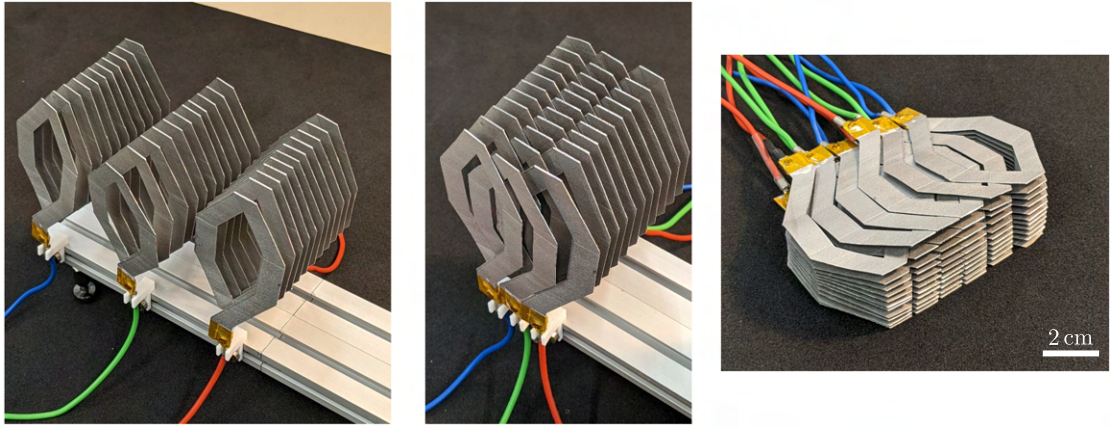


Figure 4.19: Rail for assembly of the *out-of-plane* coil type: (left) elongation of the coils; (center) slid coils for assembly; (right) assembled coils removed from rail.

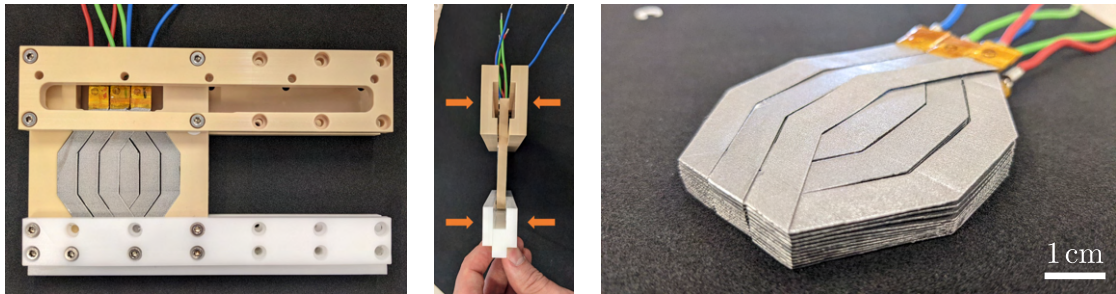


Figure 4.20: Assembly process: integration/pressing within a glider

assembly of multiple coils without damaging them. Once detached from the rail, the coils tend to elongate similarly to compression springs due to their geometry. That is why they must be maintained firmly to fit properly within the air-gap of the machine. In an industrial framework, the coils could be potted (i.e. placed within a mold into which an epoxy resin is injected at high pressure) to form a compact block containing the coils. This was not performed for two reasons: first, once potted, the glider is non-dismountable, preventing changes from being applied onto the coils (common while prototyping). Secondly, the size of this mold is quite restricting in terms of coil designs, and a new one is expensive for too few units to be tested. Thus, a mechanical housing was developed to maintain the coils compressed and form a glider that can slide between the magnet arrays of the machine of interest. Depending on the number of coils integrated within the winding, several mounting positions were possible. An example is shown in Fig. 4.20 for three coils. The different structural pieces are in PEAK and POM to prevent the formation of eddy currents within the structure while sliding between the magnets.

The pressing process stresses the different coils due to the large number of turns and important fill-factor desired. It induces the insulation to deform and partially fuse together (similar to pressed orthocyclic winding made of round copper wire). This is supported by the fact that the different coils remain pressed together even when removed from the housing, as shown on the right side of Fig. 4.20. It has a downside for these samples, though. The remaining porosity

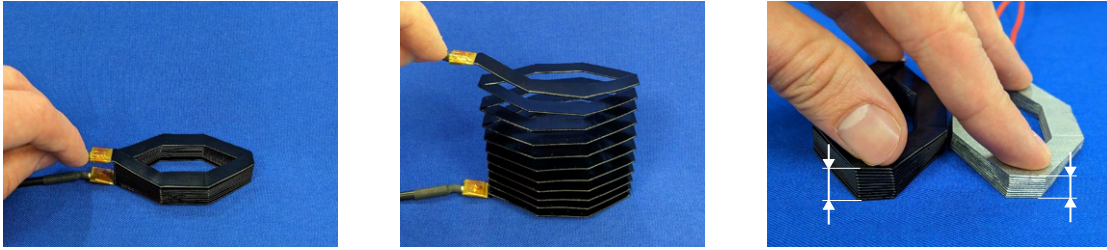


Figure 4.21: Coil insulated with a black powder coating: (left) non-elongated; (center) elongated, and (right) comparison of the total coil thickness when pressed between a coil insulated with the black powder and one insulated with the transparent varnish.

and sharp edges from the aluminum coils' manufacturing process pierce through the thin insulation layer creating short circuits. It happened for the coils insulated with parylene or the impregnation varnish. When considering the coils insulated with the black powder coating, the insulating layer was too thick even when compressed compared to the others, as shown in Fig. 4.21. They do not fit the air-gap of the machine of interest. Thus, it has been decided to perform the electromagnetic tests described in Section 4.3.3 with only single coils instead of the assembled ones. This does not compromise the proof-of-concept for this thesis, but we still propose different possibilities to solve this issue in the future:

1. More margin on the tracks and insulation thickness could be considered to prevent insulation damage when pressed.
2. The printed parts could be polished or sanded to evaluate the effect of the surface roughness or edges sharpness on the insulation deposition and possible damages.
3. Different insulating materials and methods could be explored to establish a more controlled process with thin and strong insulating layer deposition. Alternatives are automated dipping with different varnishes, anodization, or electrodeposition.

In total, 2 non-thickened coils with *in-plane* distributed turns; 7 non-thickened, 2 min-, 2 mid-, and 2 max-thickened coils with *out-of-plane* distributed turns have been successfully manufactured and individually insulated. Furthermore, 7 non-thickened multi-functional coils with *out-of-plane* distributed turns, and integrated heat sinks have been realized too.

4.3.3 Electromagnetic properties

4.3.3.a Electrical resistance

The effective conductivity of the pieces provided in Section 4.3.2.a was determined by the deviation of the measured resistance from the one defined by a high-resolution simulation: $\sigma_{\text{proto}} = \sigma_{\text{simu}} \cdot R_{\text{simu}} / R_{\text{proto}}$, with σ_{simu} , σ_{proto} , and R_{simu} , R_{proto} the electrical conductivity and resistance of the simulated coil and the prototype respectively. A milli-Ohmmeter (HIOKI RM3545) is used to measure the low resistance of the coils with high precision. The probes have Kelvin clips to perform a 4-point-measurement and remove the influence of the probe wires. The average resistances of the printed coils after heat treatment are reported here. The coils with *in-plane* distributed turns have an average value of $R^{\text{IP}} = 58.6 \text{ m}\Omega$, and the one for the non-thickened coils with *out-of-plane* distributed turns an average value of $R^{\text{OP}} = 22.8 \text{ m}\Omega$. The comparison with the average resistance for the thickened coils is shown in Table 4.4. It is concordant with the relative changes expected from the values for the coils simulated in pure copper from Table 4.1. A slightly larger difference of 1% is observed for the mid-thickened types but is still within the error margin coming from the small number of samples considered.

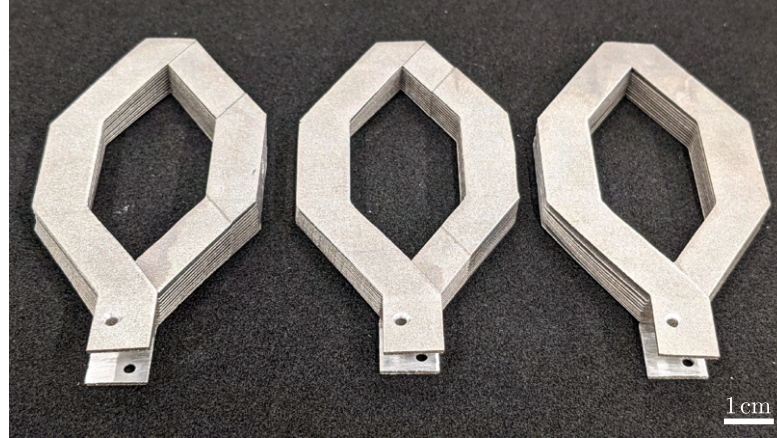


Figure 4.22: Additively manufactured thickened coils for *completed* linear winding. From left to right: min-, mid-, and max-thickened types, respectively. Figure reused from [135]. ©2022 IEEE.

Table 4.4: Measured resistance R and relative change r of the different types of coil with *out-of-plane* distributed turns in a *completed* winding made of aluminum AlSi12 after heat treatment.

	Resistance [$m\Omega$]	Relative change [%]
Non-thickened	22.8	0.0
Min-thickened	20.3	-10.9
Mid-Thickened	18.5	-18.9
Max-Thickened	17.1	-25.0

An example of each thickened coil is shown in Fig. 4.22. The multi-functional coils with *out-of-plane* distributed turns have an average resistance of $R^{\text{OP-MF}} = 22.7 \text{ m}\Omega$. This corresponds to a negligible difference from the single-functional ones, confirming the statement of unchanged resistance at room temperature.

4.3.3.b Back-EMF measurements

As already introduced, a full working winding cannot be fitted to the machine of interest due to some limitations in the insulation process. That is why individual coils (one per phase) are mounted in a glider to measure the back-electromotive force (back-EMF) induced from the motion relative to the fixed permanent magnet rail. Some dummy coils or intermediate pieces have been realized to maintain and position the metallic coils properly. In the case of coils with *in-plane* distributed turns, a glider of only two phases could be assembled due to the limited number of available units. On the other hand, three coils could be mounted for the coils with *out-of-plane* distributed turns, forming three different phases. Fig. 4.23 shows some examples of the assembled gliders. While only individual coils (per phase) are tested here, the expected performances of a full winding made of 4 coils per phase can be realistically obtained by scaling the obtained values accordingly. The back-EMF is not affected by mutual effects coming from the other coils; only the effective winding inductance is expected to be affected. A commercial linear motor drives the glider with the different AM coils. It enabled us to perform measurements for different linear velocities ranging from 100 mm/s to 1000 mm/s. Considering a magnetic period of 64 mm fixed by the permanent magnets, the tested velocity range corresponds to a frequency range starting from 1.56 Hz to 15.6 Hz. Ideally, higher

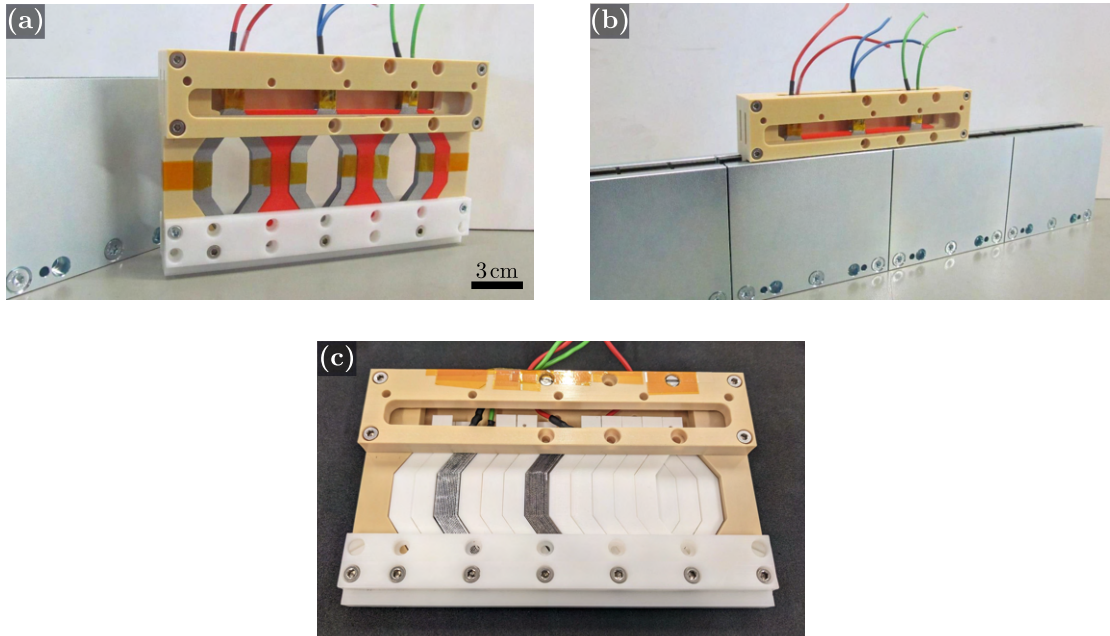


Figure 4.23: Assembled gliders to be tested: (a) assembly with three coils having *out-of-plane* distributed turns, one per phase; (b) glider mounted between the magnet arrays forming the rail; and (c) assembly with two coils having *in-plane* distributed turns forming two phases.

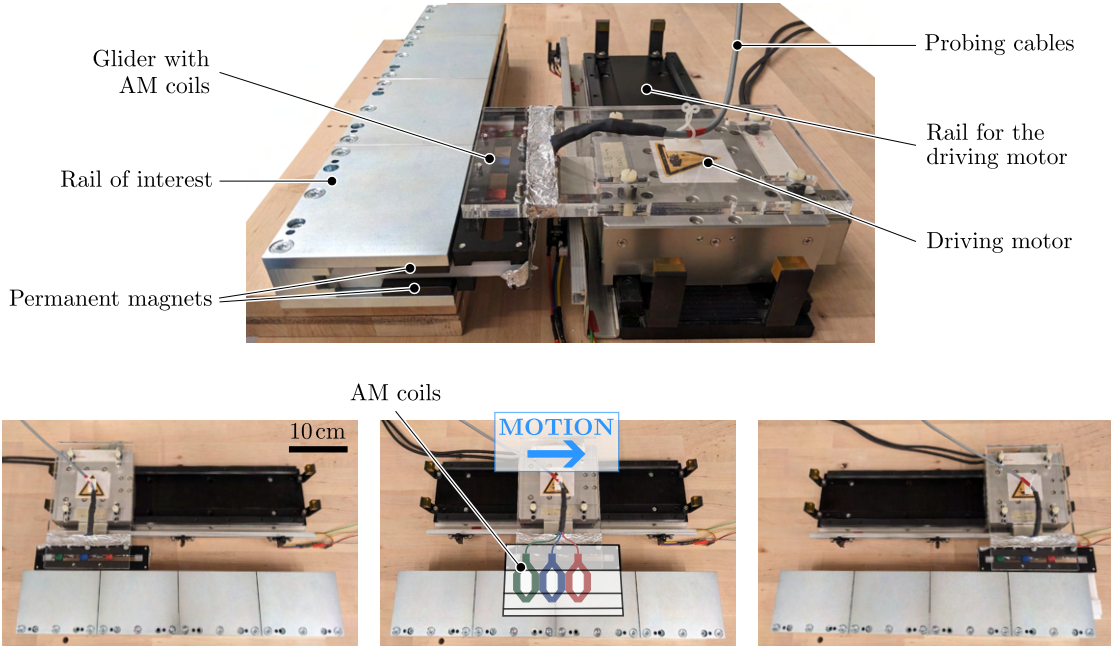


Figure 4.24: Test-bench for back-EMF measurements

frequencies would have been tested, but the maximal speed achievable by the driving motor limited this. Nevertheless, high-performance linear motors usually achieve a maximal velocity below 10 m/s at the considered scale. This difference should not be large enough to observe significant high-frequency phenomena such as eddy currents. The mounted test bench is shown in Fig. 4.24. Shielded cables have been used to connect the coils to the oscilloscope to reduce possible EMI. The output cables from each coil are grounded together to fix the neutral point. The back-EMF measured are the phase-to-neutral induced voltages. Some aluminum foil is added near the connecting cables to reduce EMI coming from the driving motor or other electronic equipment in the room.

The obtained signals $U_A(t)$, $U_B(t)$ and $U_C(t)$ are sinusoidal with an increasing, then stationary, finally decreasing magnitude. They correspond to the samples' acceleration, constant speed, and deceleration regimes across the rail of interest. An example is shown in Fig. 4.25a for a speed of 1 m/s with a glider composed of coils with *out-of-plane* distributed turns. A low-pass filter with a critical frequency of 50 Hz has been applied to the signal to remove the high-frequency noise coming from EMI. Part of the stationary regime of a duration Δt is extracted for further study. The associated spectrum analysis⁸ is investigated by performing a Fourier transform of the different restrained signals considering a sampling rate of 100 kHz. It is shown in Fig. 4.25b. The fundamental component of the different back-EMF appears at the expected $f_0 = 15.6$ Hz. A secondary peak is seen at $f_3 = 3f_0 = 46.8$ Hz but with a much lower magnitude. It confirms that the back-EMF is mainly sinusoidal at a constant speed. The same behavior is observed for a coil with *in-plane* distributed turns. The root-mean-squared (RMS) values of

⁸This analysis is performed on the non-filtered signal to highlight the significance of the low-frequency components compared to the higher ones.

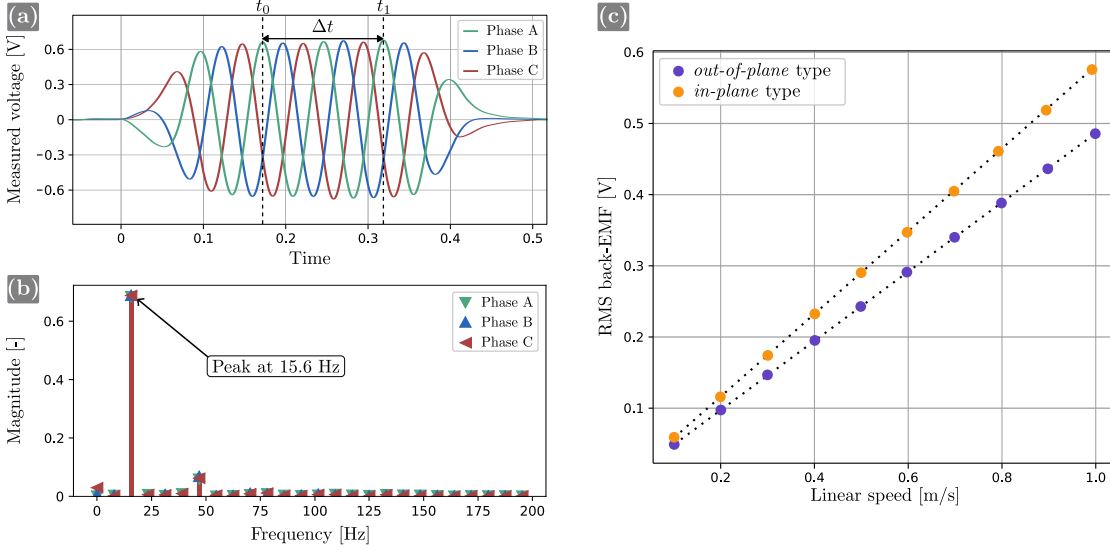


Figure 4.25: Back-EMF measurements and results: (a) Filtered back-EMF measured in the three phases driven at 1.0 m/s; (b) frequency spectrum (Fourier transform with normalized magnitude) of the non-filtered measurements in the Δt frame; and (c) results of the back-EMF experiments for different coil types and different speeds.

each signal during this regime are computed as follows:

$$U_i^{\text{RMS}} = \sqrt{\frac{\int_{t_0}^{t_1} U_i^2(t) dt}{\Delta t}} \quad \text{for } i = A, B, C. \quad (4.12)$$

The averaged value between the phases is computed $U^{\text{RMS}} = (U_A^{\text{RMS}} + U_B^{\text{RMS}} + U_C^{\text{RMS}})/3$. The experiment is repeated for different linear velocities controlled by the driving motor. The obtained average back-EMF for different speeds are plotted in Fig. 4.25c for the gliders composed of different coil types. The coil with *in-plane* distributed turns exhibited a back-EMF constant of $k_u^{\text{IP}} = 0.581 \text{ V/(m/s)}$, while the one with *out-of-plane* distributed turns exhibited a back-EMF constant of $k_u^{\text{OP}} = 0.486 \text{ V/(m/s)}$. These values correspond to the slopes of the dotted curves fitted to the measurements in Fig. 4.25c. The coil with *in-plane* distributed turns has a larger back-EMF constant because it has a larger number of turns than the one with *out-of-plane* distributed turns. However, one can observe that despite being both *diamond-shaped*, the two coil types do not have the same value when dividing their back-EMF constant by their respective number of turns. This shows that the turn distributions also have an effect independent of the number of turns as discussed in Section 4.1.2 and illustrated in Fig. 4.3.

The machine of interest is purely electrodynamic, meaning the motor is only driven by the Lorentz force F without reluctant components. The Lorentz force is linearly proportional to the input current $F = k_F I$, with k_F the force constant. Assuming a symmetric three-phase winding supplied with three-phase currents in phase with the different back-EMFs, the force constant can be formulated as [82]:

$$k_F = \frac{3\sqrt{2}}{2} \frac{\pi}{W_{\text{PM}}} \hat{\Psi}_0, \quad (4.13)$$

with $\hat{\Psi}_0$ the peak value of the fundamental component of the magnetic flux $\Psi(t)$ linked to the motor winding. Only the fundamental flux harmonic produces a non-zero mean force in that kind of machine. The other components could only induce a small ripple. When considering the i -phase, the linked flux is related to the corresponding back-EMF as follows:

$$U_{i(t)} = \frac{d\Psi_i}{dt} \quad \text{for } i = A, B, C.. \quad (4.14)$$

Numerical integration of the signals $U_A(t)$, $U_B(t)$ and $U_C(t)$ inside the Δt range is performed to obtain the associated fluxes. The signals are almost pure sinusoidal, so the fundamental component is directly available when integrated. This value should be independent of the velocity and the considered phase. Thus the mean value is computed to average possible differences coming from the measurements and positioning tolerances between the phases $\hat{\Psi}_0 = (\hat{\Psi}_{A0} + \hat{\Psi}_{B0} + \hat{\Psi}_{C0})/3$. For the coil with *in-plane* distributed turns, the value $\hat{\Psi}_0^{\text{IP}} = 8.64 \times 10^{-3}$ Wb is obtained, and $\hat{\Psi}_0^{\text{OP}} = 7.34 \times 10^{-3}$ Wb for the coil with *out-of-plane* distributed turns. This results in a force constant of $k_F^{\text{IP}} = 1.80$ N/A and $k_F^{\text{OP}} = 1.53$ N/A for a single coil with *in-plane*, and *out-of-plane* distributed turns respectively. The corresponding motor constants can be derived based on (3.16), resulting in $k_m^{\text{IP}} = 7.43$ N/ \sqrt{W} , and $k_m^{\text{OP}} = 10.12$ N/ \sqrt{W} . One can observe that the motor constant is larger for coils with *out-of-plane* distributed turns than for coils with *in-plane* distributed turns. It is explained by the smaller resistance of the *out-of-plane* type compared to the other. Thus, despite a smaller force constant, the *out-of-plane* type performs better due to its great trade-off between its magnetic coupling with respect to its electrical resistance. The different values are summarized in Table 4.5. Attention is drawn to the fact that the provided values assume a winding composed of only one coil per phase, as done in the experiments. However, the proposed design initially considered four coils per phase, corresponding to more significant values when scaled accordingly.

Table 4.5: Measured electromagnetic properties of a single coil per phase.

	R [m Ω]	k_u [V/(m/s)]	$\hat{\Psi}_0$ [mWb]	k_F [N/A]	k_m [N/ \sqrt{W}]
<i>in-plane</i> (IP)	58.6	0.581	8.64	1.80	7.43
<i>out-of-plane</i> (OP)	22.8	0.486	7.34	1.53	10.12

4.3.4 Thermal properties

This section studies the difference in thermal properties between a single- and a multi-functional coil with *out-of-plane* distributed turns. Only individual coils are examined because the insulation layer is thicker than expected, making studying a fully assembled winding unrealistic. Acrylic (PMMA) supports are used to maintain the coils compressed in order to characterize their thermal behavior. As shown in Fig. 4.26, minimal contact with the pieces has been ensured to prevent the support from reducing the effective exchange surface with the environment used for cooling. The coils were not potted to still allow disassembly for prototyping reasons. Thermocouples, in contact with the coil, are maintained in position by a small piece of KAPTON taped on the PMMA support (to minimize its effect on the cooling properties of the samples). The samples have been placed in an insulated box to prevent possible external air flows from disturbing the measurements. A DC power supply CPX400DP

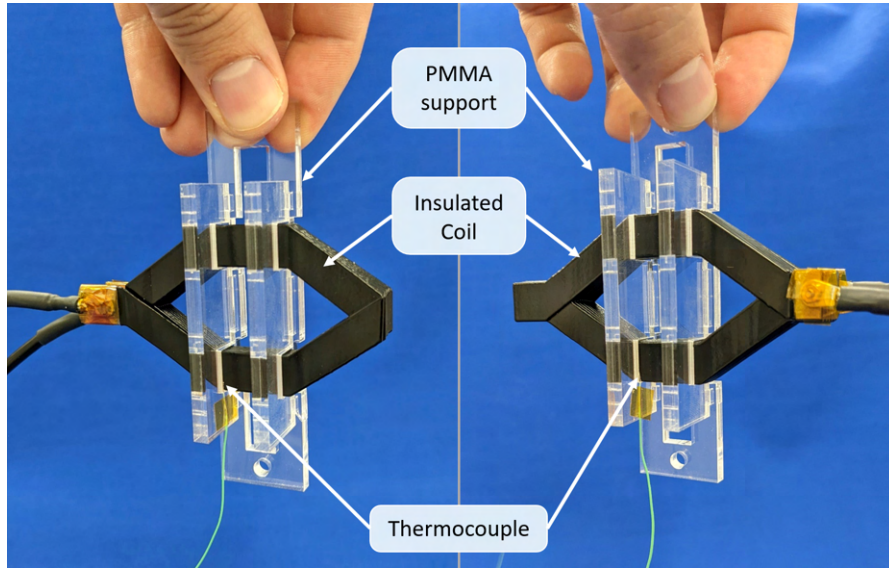


Figure 4.26: Single- (left) and multi-functional (right) insulated coils maintained compressed by a PMMA support. Thermocouples are fixed to the supports and in direct contact with the coils. The pieces are suspended in the air to prevent heat exchange with other surfaces. They are kept in a closed box to prevent perturbation coming from the environment. Figure reused from [135]. ©2022 IEEE.

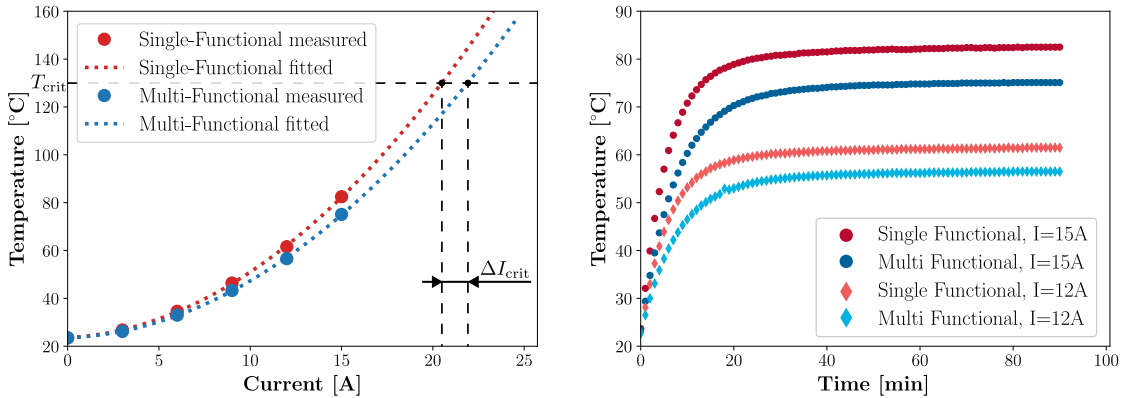


Figure 4.27: Experimental results from the thermal tests on single coils: (left) dependency of stationary temperature with input current; and (right) example of transient temperature increase for two different current levels. Figure reused from [135]. ©2022 IEEE.

Dual 420Watt from AIM-TTI is used to power the coils with a constant current. Several tests are performed at different current levels up to 15A as shown in Fig. 4.27. The supports in PMMA cannot sustain temperatures larger than 90 °C, limiting the maximal tested current. In practice, the maximal temperature is limited by the insulation material melting point around 180 °C, providing a larger maximal current limit. Nevertheless, the stationary temperature with respect to the input current is expected to behave quadratically in this range. Thus, a polynomial function of order two is fitted to the measurements. The temperature for larger currents can be extrapolated from it. The single- and multi-functional coils are estimated to

reach the critical temperature of $T_{\text{crit}} = 130\text{ }^{\circ}\text{C}$ at a current of 20.49 A and 21.90 A, respectively. This shows an increase $\Delta I_{\text{crit}} = 1.41\text{ A}$, corresponding to +7% for the maximal current flowing inside the multi-functional coil. As the generated force is directly linearly proportional to the input current, it will also be improved by +7%. The experiment studies a single coil with a lower conductivity than the bulk. Nevertheless, we expect results similar to the ones presented in Section 4.2.3 if a full winding of 12 coils with bulk conductivity is considered. For future works, a careful characterization of the effective thermal conductivity of the printed samples could be performed. It would permit a direct comparison to simulations with realistic settings. Indeed, the material properties of additively manufactured metals are anisotropic and depend on the printing direction and possible heat treatments. This has been recently discussed in [155, 156].

4.3.5 Conclusion

Despite a lower electrical conductivity than copper, aluminum is chosen as the material of interest. This material's technology is more mature, and a smaller resolution is available. More advanced machines and printing processes will soon permit copper pieces to achieve features of size close to the current aluminum. New machines with heated chambers also reduce thermal fluctuations, enabling larger aspect ratios without supports. Different technologies to print metals, such as SLA, are now achieving results similar to SLS [157] and could be worth investigating in the future. A general rule for fastly developing technologies such as AM is to renew the state of the art often because much improvement is achieved yearly. In addition to the printing process, different post-processing steps are discussed. Heat treatments increasing the effective conductivity are presented, as well as connections with the power supplying wires, and the insulation process. The insulation step has been more challenging than expected for the *out-of-plane* type due to its overlapping nature with multiple turns. It requires elongating the coils to press them later together, sometimes damaging the insulation. More work is needed on this process, with the study of automated methods for better control of the deposited layer thickness and the analysis of different materials for supporting the pressing step while not requiring too thick insulation. Nevertheless, the fabrication process of additively manufactured coils is studied and described in detail. Different solutions are provided, such as the pinhole test for identifying insulation defects.

Finally, different tests are performed to characterize the manufactured electromagnetic coils. The effective conductivity of the samples is first determined. Then, back-EMF measurements permit the evaluation of the magnetic coupling of the different fabricated coils with the permanent magnets inside the motor. The coils with *in-plane* distributed turns achieve better magnetic coupling with the permanent magnets of the rail due to their larger number of turns. However, the coils with *out-of-plane* distributed turns have a smaller resistance achieving a relatively better motor constant than the coils with *in-plane* distributed turns despite their lower number of turns. The self-cooling capability of the proposed multi-functional coils is validated. The integrated heat sink inside the coils made of an aluminum alloy enables an increase of current of +7% before reaching critical temperature. It corresponds to a similar rise in output force. The other consequence of such improved thermal properties is the improved motor efficiency for fixed input current. Indeed, as the reached winding temperature is lower, the resistivity and, thus, the Joule losses will be lower too.

4.4 Conclusion



WHILE conventional electromagnetic coils consist of a rounded wire wound into a concentric shape; this chapter demonstrates the advantages and the feasibility of additively manufacturing these devices for electric motors. The machine of interest is a linear coreless permanent magnet machine with moving winding. It offers the possibility for the different coils to overlap across the air-gap due to the absence of iron slots. Nevertheless, the proposed concepts can be extended to other types of machines. A reference topology, the *diamond-shaped*, is selected for further study. Two types of turns distributions are considered: the *in-plane* one and the *out-of-plane* one.

Various new strategies are proposed to improve the performance of the selected winding by harvesting the design freedom provided by AM technologies. The first one consists of increasing the cross-section of the coil's tracks, when possible, to reduce their resistance locally. It permits better packing of the different coils and better fills the available space with active material. The second method is the possibility of creating a *completed* linear winding. Indeed, the lost periodicity coming from the unfolding of its rotating counterpart provides available space to increase the cross-section of the tracks at the borders locally. This method permits an additional reduction of the phase resistance of almost 9% without degrading the winding footprint. Reducing the resistance results in reducing the losses for a fixed input current, leading to electric motors with better efficiency. The last strategy is to combine multiple of its functionalities within a single component: an additively manufactured self-cooling electromagnetic coil. It is achieved by extending the coil head, forming heat sinks directly integrated within the coil without affecting the current path. It permits direct heat dissipation from the source, achieving better cooling capabilities. The maximal input current can be significantly increased by +12% before reaching a critical temperature. As opposed to the state-of-the-art, this new device can achieve larger forces without increasing the volume of permanent magnets or the electrical resistance. An even more significant improvement is expected for future iterations with a dedicated heat sink design. The presented concepts could also be combined to reach even better performances. Indeed, a *completed* multi-functional winding is expected to achieve a force +17.3% larger than the *uncomplete* single-functional one.

Finally, the experimental works demonstrate the feasibility of AM for working electromagnetic coils. The fabrication process is first studied and presented. Multiple coils are 3D-printed in an aluminum alloy for demonstration. Various post-processing steps are required to obtain a final coil, such as a heat treatment to increase the conductivity and the insulation of the different turns. A developed test bench characterizes the electromagnetic properties of the manufactured coils. The back-EMF of the samples sliding inside a magnetic rail is measured. It permits evaluating each coil type's back-EMF-, force-, and motor-constants. While the coils with *out-of-plane* distributed turns achieve a lower magnetic coupling than with an *in-plane* distribution due to their lower number of turns, they achieve a better motor constant due to their smaller resistance. Lastly, the capability for better heat dissipation with multi-functional coils is demonstrated with a thermal characterization.

5 SUMMARY AND PERSPECTIVES

Content

5.1 Original contributions	108
5.2 Perspectives	109
5.3 List of publications	111
5.3.1 Patents	111
5.3.2 Journals	111
5.3.3 Conferences	112



THE maturity of electromagnetic technologies has resulted in a reliance on state-of-the-art components, limiting their full potential. However, advancements in numerical methods, material science, and manufacturing techniques could significantly improve such building blocks, possibly accessing novel applications with harsher requirements. Driven by such a desire, this thesis focuses on a critical component of electromagnetic devices: the electromagnetic coil. The general strategy relies on additive manufacturing technologies to open new design spaces previously unattainable by the conventional wound rounded wire technology. Furthermore, computational design is proposed to harvest the available design freedom. A topology optimization framework is developed and tested, demonstrating the automated design of electromagnetic coils in a wide range of scenarios. Novel coil topologies are generated for motor windings and a 3-D electromagnet manipulators. Additive manufacturing is demonstrated as a viable technology for achieving electromagnetic coils with cutting-edge performances affecting a wide range of applications. A synthesis of the fabrication process is proposed, and additional design features are outlined to further push forward the specifications and functionalities of such devices.

5.1 Original contributions

The main contributions to the fields of computational design and additive manufacturing of electromagnetic coils are summarized as follows:

- ***Topology optimization of electric conductors in 2-D to design coils***

A density-based topology optimization framework is developed for the automated design of conductor tracks in 2-D. For the first time, an environment made of materials with different natures (ferromagnetic regions) is considered. It required the integration of different physics for the simulation constituting the computational design method of interest.

- ***Multi-coil interpolation scheme to design windings with topology optimization***

A specific interpolation scheme is proposed to enable the design of winding made of multiple coils sharing the same design space. This lifts the restriction on fixing the position of the coils prior to design and leaves the computational framework to determine the ideal winding packing. The simple yet efficient approach does not require additional constraints or changes in the optimization problem; only the material interpolation scheme is modified.

- ***2.5-D formulation for designing overlapping windings efficiently***

A 2-D topology optimization cannot achieve the design of overlapping windings because the coil topology is constrained to the plane. Instead of implementing a computationally demanding and time-consuming 3-D topology optimization method, a "2.5-D" formulation is proposed. It combines two 2-D layers, one on top of the other, to enable the design of coils with variable thickness and possibly overlapping across the third dimension. This method keeps a low computational cost while covering a more extensive solution space. Its effectiveness is demonstrated by generating a new topology for motor winding with overlapping coils achieving a motor constant 17% better than the reference one.

- **Topology-optimization of coils in 3-D achieving asymmetric windings design**

Topology optimization of 3-D electromagnetic coils is demonstrated for the first time. Additionally, multiple coils with different purposes are designed simultaneously by combining multiple loading cases with the previously developed multi-coil interpolation scheme into a multi-objective optimization framework. It led to the design of a new electromagnet manipulator achieving a region with field uniformity 7 times larger and with balanced characteristics.

- **Realization of a 3D-printed winding for coreless electric motor with different turns distributions**

Additively manufactured electromagnetic coils with *in-plane* distributed turns are realized for the first time. It shows an alternative to the already existing *out-of-plane* turns distribution. Furthermore, the design freedom provided by additive manufacturing is harvested to have conductor tracks with varying cross-sections, which enables, among other possibilities, linear windings to be *completed* at their border for a decreased resistance. These new design features reduce the generated losses for the same electromagnetic potential, thus, resulting in more efficient electric motors.

- **Combining the electromagnetic and cooling functionalities inside a single additively manufactured winding**

The concept of self-cooling windings is proposed and demonstrated in this thesis. The additional design freedom provided by additive manufacturing technologies enables the integration of heat sinks directly within the coil head, better extracting the generated heat to the environment without degrading the electromagnetic properties. A single component (the coil) is responsible for generating the magnetic field driving the motor and also cooling itself down without needing an additional heat extraction system. It enables an operating current increased by 12% for an *uncomplete* linear winding, and by 17.3% for a *completed* one, resulting in stronger machines for the same volume of permanent magnets and same phase resistance. This contribution opens the path for the next generation of electromagnetic systems with cutting-edge performance.

5.2 Perspectives

Beyond the work performed in this thesis, there are naturally multiple opportunities to push things further. Some of them are discussed here as interesting perspectives.

- **Post topology optimization: coil reconstruction and parametrization for further improvement**

A short-term perspective is adding post-processing steps to the developed topology optimization framework. A distribution of material onto a mesh describes the generated topology, which is not the format commonly used in mechanical modeling software. A *coil-reconstruction* step could be implemented to bridge the design stage to the manufacturing one. It has already been investigated for other applications [158, 159]. Furthermore, this could also help parametrize the resulting topologies with a few geometric parameters. They could then be fed to a global optimization framework, investigating the global optimum of the design problem.

- ***Turns modeling in topology optimization of coils***

The developed framework considers an explicit description of the turns, restricting it to only a few turns without degrading the computational cost. Indeed, modeling a larger number of turns would require a thinner mesh to improve the resolution. This limitation is alleviated by designing a single turn that is repeated post-process as shown in Fig. 3.30. However, for some applications, implicitly considering the turns is interesting to obtain the correct current density distribution across the designed coil or study higher-order phenomena like eddy currents or proximity effects. It is achieved in conventional electromagnetic FEA with homogenization techniques [160] but becomes more challenging when considered part of a topology optimization framework without a pre-defined geometry. Future work in this area is encouraged to obtain a more versatile tool.

- ***Design of multi-functional windings***

As demonstrated in Section 4.2.3, the cooling properties of an electromagnetic coil can enable larger input currents resulting in stronger devices. Thus, the developed topology optimization framework for designing electromagnetic coils could be extended to a multi-physic one considering the addition of heat dissipation properties to design multi-functional windings automatically. Furthermore, this could provide a versatile tool exploring the combination with forced cooling methods or other heat dissipation systems. The concept of multi-functional winding has recently been extended to a motor with forced cooling [161], reinforcing the interest in such systems for creating the next generation of electromagnetic devices.

- ***Consider AC phenomena in the design process of 3D printed coil***

AC losses in the winding have not been investigated in this work. However, depending on the application, they can significantly affect the device's efficiency and power output. Thinner conductors with *in-plane* distributed turns are used in conventional coils. Slits performed in the tracks have also been recently proposed as an alternative in the literature [86]. This method could be implemented in the AM coils with *out-of-plane* distributed turns proposed here. Modeling these AC effects could be integrated into the topology-optimization framework to find other alternatives. Additionally, these phenomena could also occur in the extended heat sink of the proposed multi-functional winding due to the alternating current traveling the coil. Again, slits or laminated extensions would reduce their effect, but other geometries could be explored too. The great flexibility provided by AM technologies is promising for tackling such issues.

- ***Improved performance in the additive manufacturing process***

From a general perspective, improving the performance of manufacturing machines and processes is always attractive. Smaller resolution and larger aspect ratios for printing copper would ease the integration of this technology in smaller machines. They would also enable having AM coils with a larger number of turns. Furthermore, it would significantly contribute to the field if high-performance multi-material printing machines were available. Indeed, it is desired to manufacture the conductive tracks (metals) and the coil's insulation (polymers or ceramics) simultaneously with a significant metal fill-factor. It would ease the implementation of coils with *in-plane* distributed turns that are expected to have better AC performance and ease the industrialization of such devices.

5.3 List of publications

Throughout this thesis, several works have been published in journals, shared with the scientific community at international conferences, and even resulted in some patents. Some of them cover applications beyond the scope of this manuscript. Nevertheless, as they contributed to strengthening some of the knowledge and skills acquired during this thesis, they are listed alongside the works directly affiliated with this research.

5.3.1 Patents

- Adrien Thabuis, Alessandro Fasolo, Daniele Veronesi, Xiaotao Ren, and Yves Perriard, "High-performance coil for electrical machine and coil assembly for a linear motor," European Patent 4 092 878 A1, Nov. 2022, (*filed 19th May 2021*) [162].
- Sofia Ntella, Kenny Jeanmonod, Adrien Thabuis, Bhawnath Tiwari, Christian Koechli, Yoan Civet, Zoltan Pataky, and Yves Perriard, "Miniaturized magnetorheological valve using electropermanent magnets," (*filed December 2022, pending*)

5.3.2 Journals

- G. Burnand, A. Thabuis, D. M. Araujo and Y. Perriard, "Novel Optimized Shape and Topology for Slotless Windings in BLDC Machines," **IEEE Transactions on Industry Applications**, Apr. 2020, doi: 10.1109/TIA.2019.2956717.
- X. Ren, A. Thabuis, A. Hannukainen and Y. Perriard, "Shape Optimization of Soft Magnetic Composites Using Level-Set Method," **IEEE Transactions on Magnetics**, May 2021, doi: 10.1109/TMAG.2021.3064185.
- A. Thabuis, S. Thomas, T. Martinez, P. Germano, and Y. Perriard, "Designing compliant mechanisms composed of shape memory alloy and actuated by induction heating," **Smart Materials and Structures**, Aug. 2021, doi: 10.1088/1361-665X/ac1b15
- L. Chen, A. Thabuis, Y. Fujii, A. Chiba, M. Nagano and K. Nakamura, "Principle and Analysis of Radial-Force-Based Swirling Actuator for Low-Speed High-Torque Applications," **IEEE Transactions on Industry Applications**, April 2022, doi: 10.1109/TIA.2022.3142118.
- A. Thabuis, X. Ren, T. Duong, and Y. Perriard, "Exploring Beyond the Helmholtz Coils for Uniform Magnetic Field Generation With Topology Optimization," **IEEE Transactions on Magnetics**, Sept. 2022, doi: 10.1109/TMAG.2022.3183362, (*presented at COMPUMAG 2021*).
- X. Ren, A. Thabuis, R. Corcolle, A. Hannukainen, and Y. Perriard, "Level-Set-Based Shape Optimization on Soft Magnetic Composites With Isotropy Constraint," **IEEE Transactions on Magnetics**, Sept. 2022, doi: 10.1109/TMAG.2022.3165350, (*presented at COMPUMAG 2021*).
- A. Thabuis, X. Ren and Y. Perriard, "Enhanced Electric Motors using Multi-Functional 3D Printed Winding with Integrated Heat Sinks," **IEEE Transactions on Energy Conversion**, Nov. 2022, doi: 10.1109/TEC.2022.3221189.

- [A. Thabuis](#), S. L. Ntella, B. Tiwari, K. Jeanmonod, C. Koechli, and Y. Perriard, "Highly Efficient Miniaturized Magnetorheological Valves Using Electropermanent Magnets," **IEEE Robotics and Automation Letters**, Jan. 2023, doi: 10.1109/LRA.2023.3238669, *(will be presented at IROS 2023)*.
- [A. Thabuis](#), M. C. Rivera, X. Ren, and Y. Perriard, "Topology Optimization of an Electromagnet Manipulator for 3D Uniform Magnetic Field," **IEEE Transactions on Magnetics**, Feb. 2023, doi: 10.1109/TMAG.2023.3247867, *(presented at CEFC 2022)*.
- [A. Thabuis](#), X. Ren and Y. Perriard, "Topology Optimization of Motor Windings for Coreless Electrical Machines," 2023 *(submitted to IEEE Access and available on TechRxiv)*, doi: 10.36227/techrxiv.22666105).

5.3.3 Conferences

- [A. Thabuis](#), X. Ren, G. Burnand and Y. Perriard, "Density-Based Topology Optimization of Conductor Paths for Windings in Slotted Electrical Machines," 22nd International Conference on Electrical Machines and Systems (**ICEMS**), 2019, pp. 1-6, doi: 10.1109/ICEMS.2019.8921728.
- X. Ren, [A. Thabuis](#), A. Belahcen and Y. Perriard, "Topology Optimization for Coils of Electric Machine with Level-set Method," 2019 22nd International Conference on Electrical Machines and Systems (**ICEMS**), 2019, pp. 1-4, doi: 10.1109/ICEMS.2019.8921847.
- C. H. Mejia, J. Jayet, P. Germano, [A. Thabuis](#) and Y. Perriard, "Linear Impact Generator for Automated Dataset Acquisition of Elastic Waves in Haptic Surfaces," 2019 22nd International Conference on Electrical Machines and Systems (**ICEMS**), 2019, pp. 1-5, doi: 10.1109/ICEMS.2019.8922478.
- L. Chen, [A. Thabuis](#), A. Chiba, M. Nagano, and K. Nakamura, "Radial-Force-Based Swirling Actuator with Surface-Permanent-Magnet Structure for Low-Speed High-Torque Applications," 2019 IEEE Energy Conversion Congress and Exposition (**ECCE**), 2019, pp. 6106-6113, doi: 10.1109/ECCE.2019.8912163.
- [A. Thabuis](#), S. Thomas, T. Martinez and Y. Perriard, "Shape Memory Effect of Benchmark Compliant Mechanisms Designed With Topology optimization," 2020 IEEE/ASME International Conference on Advanced Intelligent Mechatronics (**AIM**), 2020, pp. 571-576, doi: 10.1109/AIM43001.2020.9158984.
- [A. Thabuis](#), S. Thomas, T. Martinez and Y. Perriard, "Multi-Output Compliant Shape Memory Alloy Bias-Spring Actuators," 2020 IEEE/ASME International Conference on Advanced Intelligent Mechatronics (**AIM**), 2020, pp. 795-800, doi: 10.1109/AIM43001.2020.9158997.
- S. Thomas, G. Maquignaz, [A. Thabuis](#) and Y. Perriard, "A Self-Biasing Shape Memory Alloy Gripper for Lightweight Applications," 2021 IEEE/RSJ International Conference on Intelligent Robots and Systems (**IROS**), 2021, pp. 8211-8216, doi: 10.1109/IROS51168.2021.9636155.

- C. Hernandez-Mejia, X. Ren, A. Thabuis, J. Chavanne, P. Germano and Y. Perriard, "Generative Adversarial Networks for Localized Vibrotactile Feedback in Haptic Surfaces," 2021 24th International Conference on Electrical Machines and Systems (**ICEMS**), 2021, pp. 105-110, doi: 10.23919/ICEMS52562.2021.9634513.
- X. Ren, A. Thabuis and Y. Perriard, "Innovative Design of 3D-printed Winding for Linear Motor," 2022 25th International Conference on Electrical Machines and Systems (**ICEMS**), 2022, pp. 1-6, doi: 10.1109/ICEMS56177.2022.9982962.
- A. Thabuis, X. Ren, and Y. Perriard, "Automated Design of Conductor Tracks for Electromagnetics," 24th International Conference on the Computation of Electromagnetic Fields (**COMPUMAG**), 2023 (*accepted*).

A Weak form for electric conduction problem with current source

The weak form of the electric conduction problem has been defined assuming voltage sources. It results in an electric current magnitude dependent on the layout of the conductor being designed. Indeed, the distribution of conductors over the design space can evolve at each iteration of the optimization process, resulting in a possible varying electric resistance. This implies a varying electrical current magnitude flowing through the conductor for a fixed voltage source. An example is shown in Fig. A.1 comparing the same conductor layout for different electrical sources. The dependency mentioned above could be limiting depending on the type of application. For example, in the magnetic manipulation problem presented in Section 3.3, the magnitude of the generated magnetic flux density is critical. Thus, fixing the electrical current associated with this magnetic flux is interesting to remove a constraint while designing the coil layout.

This annex presents the weak form associated with a single current source. The boundary of the design domain Ω is defined as follows: $\delta\Omega = \Gamma_C \cap \Gamma_D^{\text{GND}} \cap \Gamma_{N0}$, with Γ_C the boundary onto which a current source is applied, Γ_D^{GND} the boundary onto which the electric potential is grounded (GND), and Γ_{N0} the remaining boundaries onto which null Neumann BCs are assured. The current source results in a floating electric potential U_{float} onto the associated

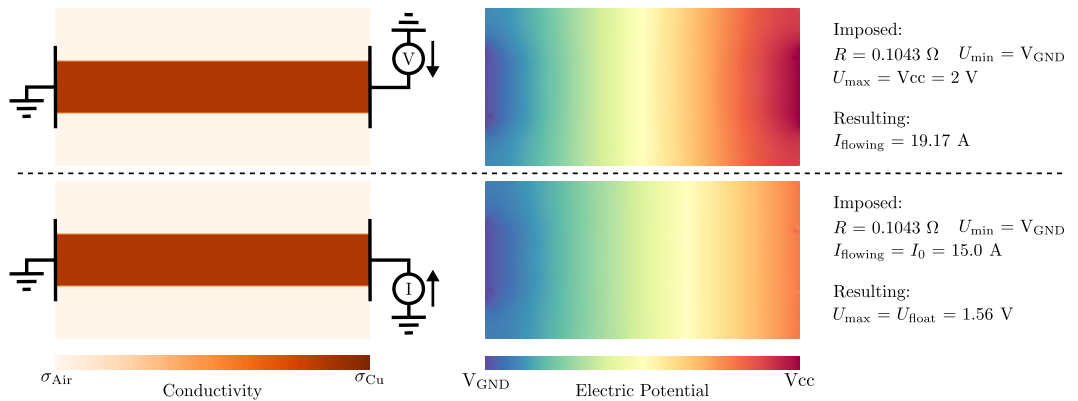


Figure A.1: Example of a 2-D design domain with different electric boundary conditions: (top) Voltage source, and (bottom) current source.

boundary:

$$U(x,y) = U_{\text{float}} \text{ on } \Gamma_C, \quad \text{and} \quad \int_{\Gamma_C} \mathbf{J}(x,y) \cdot \mathbf{n} d\Gamma = -I_0, \quad (\text{A.1})$$

with \mathbf{n} the normal vector to the boundary, and I_0 the magnitude of the imposed current. An average current density is deducted $J_{\text{avg}} = -I_0/|\Gamma_C|$. In a domain with fixed distributions of materials ($\sigma(x,y)$ known), the condition from (A.1) is equivalent to determining the correct electric field on the boundary. It corresponds to enforcing specific Neumann BCs. However, in the case of topology optimization with evolving material properties between iterations, a more general formulation is required. Equation 3.3 subject to the aforementioned BCs is thus reformulated as the following variational problem¹:

$$\text{Find: } (u, u_{\text{float}}) \in \mathcal{U} \times \mathbb{R}, \quad \forall (v, v_{\text{float}}) \in \mathcal{V} \times \mathbb{R}$$

such that:

$$\begin{aligned} & \iint_{\Omega} \sigma(x,y) \nabla u \cdot \nabla v d\Omega - \int_{\Gamma_C} v \sigma(x,y) \nabla u \cdot \mathbf{n} d\Gamma \\ & + \int_{\Gamma_C} (u - u_{\text{float}}) \sigma(x,y) \nabla v \cdot \mathbf{n} d\Gamma \\ & + \int_{\Gamma_C} (J_{\text{avg}} + \sigma(x,y) \nabla u \cdot \mathbf{n}) v_{\text{float}} d\Gamma = 0, \end{aligned} \quad (\text{A.2})$$

with $u = u(x,y)$ the trial function, u_{float} the trial constant, $v = v(x,y)$ the test function, and v_{float} the test scalar. $\mathcal{U} \subset H^1(\Omega)$ is the trial space satisfying the Dirichlet BCs specific to this problem, and $\mathcal{V} \subset H^1(\Omega)$ is the corresponding test space. The Dirichlet BCs are not the same as the ones from the equivalent voltage source problem. Once (A.2) is solved, the trial function and scalar correspond to the electric scalar potential $U(x,y)$, and the floating potential U_{float} respectively.

¹The author would like to thank Prof. David Kamensky from UC San Diego for his assistance with the formulation of the variational problem (<https://david-kamensky.eng.ucsd.edu/>).

B Sizing and scaling of the diamond topology

The sizing of the coils additively manufactured in Section 4.1 is presented here. Some scaling laws are also provided to adapt the designed geometry to other motor sizes. A more detailed description is available in the following conference paper [143]. The first step is to describe the diamond topology with a few geometric parameters. The coupling with the magnetic flux generated by the permanent magnets of the linear machine is an important criterion to consider. Thus, a dependency between the size of the magnets and the coil geometric parameters is expected. A 3-D static FEA simulation is performed in COMSOL[®] to evaluate the performance of the winding. Only the coils with *out-of-plane* distributed turns are considered. The sizes of the diamond forming the coils with *in-plane* distributed turns will be fixed to the ones determined here. The analysis first considers an air-gap and magnets with fixed dimensions. Three coils with only 5 turns each are considered to keep a reasonable mesh size.

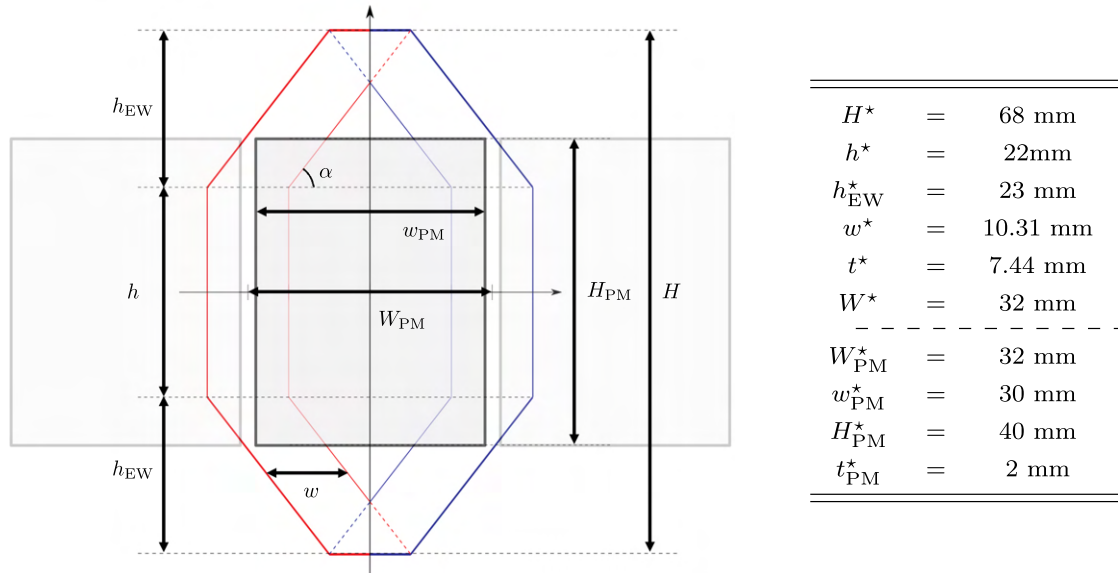


Figure B.1: Schematic defining the characteristic parameters of the coil and magnet geometry (left), and set of parameters resulting from the sizing process (right).

Appendix B. Sizing and scaling of the diamond topology

The different coils are powered by a constant electric current correctly scaled corresponding to a *frozen* scenario of a triphase system. While not ideal to evaluate the absolute value of the performance, this arrangement enables a relative evaluation of the performance with respect to the different dimensions of the coil. The following parameters describe the magnets and the coil topology:

- w_{PM} , H_{PM} , and t_{PM} the PM width, height and thickness respectively
- H , h , h_{EW} , w the coil total height, the length of the straight segment, the height of the end-winding, and the width of the tracks (straight segments), respectively.

The coil-pitch is fixed to the magnetic pole-pitch W_{PM} , while the width of the tracks w is fixed to slightly less than a third of it ($w = W_{\text{PM}}/3 - \epsilon$, with ϵ a small value) so as to account for packing with the other phases. The maximal total coil height is fixed to 1.7 times the PM height. Coreless rotating machines often constrain the overlapping winding height to be equal to the magnet height, but linear ones often do not have such a requirement. It increases the footprint of the winding but enables a better coupling with the magnetic field coming from the PM that spreads a bit beyond its active length inside the air-gap. The design of the selected diamond topology can be restricted to only determining the total coil height H and the straight segment length h . These two parameters are swept through various values stepped by 0.5 mm so as to still satisfy the maximal total height and maximize the motor constant. The resulting set of *optimized* and fixed parameters are shown in the table of Appendix B. They are indicated by a $*$ superscript for reference.

Now that the coil has been sized to the machine dimensions, we desire to formulate an appropriate scaling of these parameters with respect to the ones of the machine. A proper strategy is to rely on electromagnetic scaling laws [163, ch. 4]. For an isotropic machine scaling, we define the ratio of the lengths as $l^* = l'/l$ (with l^* and l' the length before and after scaling, respectively). If we decide to keep a constant temperature rise while scaling ($\Delta T^* = 1$), the current density scales as follows: $J^* = 1/\sqrt{l^*}$. Following such assumptions, the force scales as: $F^* = J^* (l^*)^4 = l^{*3.5}$, while the resistance scales as: $R^* = 1/l^*$. This results in a motor constant scaling as: $k_m^* = l^{*4}$. It means that if a motor constant two times larger than the reference one is desired, the machine's dimensions have to be multiplied by $\sqrt[4]{2}$. In order to conserve a maximal motor constant, the optimized parameters should be isotropically scaled if one is changed.

However, establishing a direct relationship is more complex if an anisotropic change is performed. Indeed, no analytical relationship between the coil parameters and the PM ones could be established for a non-isotropic scaling. Additional limits arise in terms of geometry feasibility too. Such a problem becomes another complex trade-off to be possibly determined using optimization methods. Nevertheless, we propose some *rules of thumb* to size an initial coil topology with respect to the permanent magnet size to perform further optimization later. We first propose a constant ratio between the permanent magnet height H_{PM} and the coil height H , to keep the relative footprint the same. Then, the angle formed by the diamond topology should be conserved: $\alpha = \arctan(2h_{\text{EW}}^*/W_{\text{PM}}^*)$. It means that, for a fixed pole pitch W_{PM} , if the height of the permanent magnet H_{PM} is increased, only the straight length of the coil h increases accordingly. On the other hand, if the magnet height H_{PM} is kept constant, and

the pole pitch W_{PM} is increased, the straight length decreases while the end-winding lengths increase. With these assumptions, there is an upper and lower limit to the pole pitch. These limits also affect the maximal and minimal aspect ratio the shape of the permanent magnet can take. The lower limit corresponds to the point where the coil's straight length equals the permanent magnet height. It can be formulated as follows:

$$\underline{W_{\text{PM}}} = \frac{W_{\text{PM}}^{\star}(H - H_{\text{PM}})}{2 \cdot h_{\text{EW}}^{\star}} = 0.487 \cdot H_{\text{PM}}. \quad (\text{B.1})$$

The upper limit corresponds to the point where the straight length becomes null, transforming the diamond topology into a rhombus one:

$$\overline{W_{\text{PM}}} = \frac{H \cdot W_{\text{PM}}^{\star}}{2 \cdot h_{\text{EW}}^{\star}} = 1.183 \cdot H_{\text{PM}}. \quad (\text{B.2})$$

The recommended anisotropic scaling rules are shown in Table B.1.

Table B.1: Scaling of the geometric parameters

H	=	$1.7 \cdot H_{\text{PM}}$
h_{EW}	=	$0.719 \cdot W_{\text{PM}}$
w	=	$(W_{\text{PM}}/3) - \epsilon$
W	=	W_{PM}

Bibliography

- [1] M. Nolte, “Kerr dam.” https://commons.wikimedia.org/wiki/File:SQK_Dam_DSC_3657.jpg. Accessed: 2022-12-07.
- [2] “A healthy wind.” <https://news.mit.edu/2022/wind-health-impact-1202>. Accessed: 2022-12-07.
- [3] “Industrial steam turbine DG040/040 -MAN Energy Solutions | Linquip.” <https://www.linquip.com/device/2688/industrial-steam-turbine-dg040040>. Accessed: 2022-12-07.
- [4] “Overview of the SPARC tokamak.” <https://www.psfc.mit.edu/sparc>, 2020. Publisher: Cambridge University Press, "Cutaway of the SPARC engineering design" Author: CFS/MIT-PSFC - CAD Rendering by T. Henderson. Accessed: 2022-12-07.
- [5] “Flexible Transformers Transform the Grid of the Future.” <https://www.energy.gov/oe/articles/flexible-transformers-transform-grid-future>. Accessed: 2022-12-07.
- [6] “Our trains | SBB.” <https://www.sbb.ch/en/station-services/during-your-journey/our-trains.html>. Accessed: 2022-12-07.
- [7] Q. a.-P. a. P. W. Movement, “Growth Sector: Electric Vehicles Sales And The New Electric Economy Have Arrived.” <https://www.forbes.com/sites/qai/2022/09/24/growth-sector-electric-vehicles-sales-and-the-new-electric-economy/>. Section: Money. Accessed: 2022-12-07.
- [8] “Clemson, Carnegie Mellon to Develop Next-Gen Manufacturing Robots | 2017-01-16 | Assembly Magazine | ASSEMBLY.” <https://www.assemblymag.com/articles/93695-clemson-carnegie-mellon-to-develop-next-gen-manufacturing-robots>. Accessed: 2022-12-07.
- [9] “Legged Robots Learn to Hike Harsh Terrain.” <https://spectrum.ieee.org/legged-robots-anymal>. Section: Robotics, Photograph: Takahiro Miki, Accessed: 2022-12-29.
- [10] “Ultra-high field MRI detects differences in brain’s ‘hippocampus’.” <https://www.eurekalert.org/news-releases/815499>. Brain MRI Getty images, Accessed: 2022-12-07.
- [11] “Proton therapy at the Paul Scherrer Institute (PSI) in Switzerland: a success story that started 25 years ago.” <https://www.psi.ch/en/media/our-research/success-story-started-25-years-ago>. Accessed: 2022-12-07.

Bibliography

- [12] “Small Electric Motors | ASAP Appliance Standard Awareness Project.” <https://appliance-standards.org/product/small-electric-motors>. Accessed: 2022-12-07.
- [13] “Welcome to KUK Group, customer-specific winding goods and assemblies.” <https://www.kukcoils.com>. Accessed: 2019-01-18.
- [14] A. P, “The Complete Guide to Laser Powder Bed Fusion in 3D Printing.” <https://www.3dnatives.com/en/direct-metal-laser-sintering100420174-2/>, Sept. 2019. Accessed: 2023-01-09.
- [15] “TruPrint 5000 Green Edition for copper printing.” https://www.trumpf.com/en_IN/products/machines-systems/additive-production-systems/truprint-5000-green-edition/. Accessed: 2019-01-18.
- [16] “Copper for 3D printing | EOS GmbH, project partner Delva Oy.” <https://www.eos.info/en/additive-manufacturing/3d-printing-metal/dmls-metal-materials/copper>. Accessed: 2023-01-09.
- [17] E. M. Dede, J. Lee, and T. Nomura, *Multiphysics Simulation*, Simulation Foundations, Methods and Applications, Springer London, London, 2014.
- [18] G. Burnand, A. Thabuis, D. M. Araujo, and Y. Perriard, “Novel optimized shape and topology for slotless windings in bldc machines,” *IEEE Transactions on Industry Applications* **56**(2), pp. 1275–1283, 2020.
- [19] B. Dehez, F. Baudart, and Y. Perriard, “Analysis of a new topology of flexible PCB winding for slotless BLDC machines,” in *2017 IEEE International Electric Machines and Drives Conference (IEMDC)*, pp. 1–8, May 2017.
- [20] R. Marler and J. Arora, “Survey of multi-objective optimization methods for engineering,” *Structural and Multidisciplinary Optimization* **26**, pp. 369–395, Apr. 2004.
- [21] C. Dapogny, R. Estevez, A. Faure, and G. Michailidis, “Shape and topology optimization considering anisotropic features induced by additive manufacturing processes,” *Computer Methods in Applied Mechanics and Engineering* **344**, pp. 626–665, Feb. 2019.
- [22] D. I. Papadimitriou and K. C. Giannakoglou, “Aerodynamic Shape Optimization Using First and Second Order Adjoint and Direct Approaches,” *Arch Computat Methods Eng* **15**, pp. 447–488, Dec. 2008.
- [23] C. M. Lalau-Keraly, S. Bhargava, O. D. Miller, and E. Yablonovitch, “Adjoint shape optimization applied to electromagnetic design,” *Opt. Express* **21**, pp. 21693–21701, Sep 2013.
- [24] M. Tarek and T. Ray, “Robust and stochastic compliance-based topology optimization with finitely many loading scenarios,” *Struct Multidisc Optim* **64**, pp. 3439–3452, Dec. 2021.
- [25] K. Gao, D. M. Do, S. Chu, G. Wu, H. A. Kim, and C. A. Featherston, “Robust topology optimization of structures under uncertain propagation of imprecise stochastic-based uncertain field,” *Thin-Walled Structures* **175**, p. 109238, June 2022.

-
- [26] O. Sigmund and K. Maute, "Topology optimization approaches," *Struct Multidisc Optim* **48**, pp. 1031–1055, Dec. 2013.
- [27] J. D. Deaton and R. V. Grandhi, "A survey of structural and multidisciplinary continuum topology optimization: post 2000," *Structural and Multidisciplinary Optimization* **49**, pp. 1–38, Jan. 2014.
- [28] F. Lucchini, R. Torchio, V. Cirimele, P. Alotto, and P. Bettini, "Topology optimization for electromagnetics: A survey," *IEEE Access* **10**, pp. 98593–98611, 2022.
- [29] S. Boyd and L. Vandenberghe, *Convex Optimization*, Cambridge University Press, Cambridge, UK ; New York, 1st edition ed., Mar. 2004.
- [30] M. P. Bendsøe and O. Sigmund, *Topology optimization: theory, methods, and applications*, Engineering online library, Springer, Berlin Heidelberg, second ed., 2011. OCLC: 711862335.
- [31] O. Sigmund, "On the usefulness of non-gradient approaches in topology optimization," *Struct Multidisc Optim* **43**, pp. 589–596, May 2011.
- [32] T. Sato, K. Watanabe, and H. Igarashi, "Multimaterial Topology Optimization of Electric Machines Based on Normalized Gaussian Network," *IEEE Transactions on Magnetics* **51**, pp. 1–4, Mar. 2015.
- [33] M. Zhou and G. I. N. Rozvany, "The COC algorithm, Part II: Topological, geometrical and generalized shape optimization," *Computer Methods in Applied Mechanics and Engineering* **89**, pp. 309–336, Aug. 1991.
- [34] K. Svanberg, "The method of moving asymptotes—a new method for structural optimization," *International Journal for Numerical Methods in Engineering* **24**, pp. 359–373, Feb. 1987.
- [35] A. Wächter and L. T. Biegler, "On the implementation of an interior-point filter line-search algorithm for large-scale nonlinear programming," *Math. Program.* **106**, pp. 25–57, Mar. 2006.
- [36] S. Rojas-Labanda and M. Stolpe, "Benchmarking optimization solvers for structural topology optimization," *Struct Multidisc Optim* **52**, pp. 527–547, Sept. 2015.
- [37] T. Y. S. Hoshina, I. F. M. Menezes, and A. Pereira, "A simple adaptive mesh refinement scheme for topology optimization using polygonal meshes," *J Braz. Soc. Mech. Sci. Eng.* **40**, p. 348, June 2018.
- [38] J.-M. Jin, *The Finite Element Method in Electromagnetics*, Wiley, Hoboken, NJ, 3. ed ed., 2014.
- [39] S. Sanogo, F. Messine, C. Hénaux, and R. Vilamot, "Topology Optimization for Magnetic Circuits Dedicated to Electric Propulsion," *IEEE Transactions on Magnetics* **50**, pp. 1–13, Dec. 2014.
- [40] M. Kollmann, *Sensitivity Analysis: The Direct and Adjoint Method*. PhD thesis, Johannes Kepler University Linz, 2010.

Bibliography

- [41] Y. Cao, S. Li, and L. Petzold, "Adjoint sensitivity analysis for differential-algebraic equations: Algorithms and software," *Journal of Computational and Applied Mathematics* **149**, pp. 171–191, Dec. 2002.
- [42] A. M. Bradley, "Pde-constrained optimization and the adjoint method." https://cs.stanford.edu/~ambrad/adjoint_tutorial.pdf, 2019. Accessed: 2021-11-14.
- [43] S. W. Funke and P. E. Farrell, "A framework for automated PDE-constrained optimisation," *arXiv:1302.3894 [cs]* -, Feb. 2013.
- [44] J. Yan, R. Xiang, D. Kamensky, M. T. Tolley, and J. T. Hwang, "Topology optimization with automated derivative computation for multidisciplinary design problems," *Struct Multidisc Optim* **65**, p. 151, Apr. 2022.
- [45] G. Allaire, *Conception optimale des structures*, no. 58 in Mathématiques & applications, Springer, Berlin, 2007. OCLC: 180941820.
- [46] G. Allaire, F. Jouve, and A.-M. Toader, "Structural optimization using sensitivity analysis and a level-set method," *Journal of Computational Physics* **194**, pp. 363–393, Feb. 2004.
- [47] E. Kuci, M. Jansen, and O. Coulaud, "Level set topology optimization of synchronous reluctance machines using a body-fitted mesh representation," *Structural and Multidisciplinary Optimization* **64**, pp. 3729–3745, Dec. 2021.
- [48] G. Allaire and B. Bogosel, "Optimizing supports for additive manufacturing," *Structural and Multidisciplinary Optimization* **58**, pp. 2493–2515, Dec. 2018.
- [49] J.-W. Luo, L. Chen, Z. Wang, and W. Tao, "Topology optimization of thermal cloak using the adjoint lattice Boltzmann method and the level-set method," *Applied Thermal Engineering* **216**, p. 119103, Nov. 2022.
- [50] S. Park, S. Min, S. Yamasaki, S. Nishiwaki, and J. Yoo, "Magnetic Actuator Design Using Level Set Based Topology Optimization," *IEEE Transactions on Magnetics* **44**, pp. 4037–4040, Nov. 2008.
- [51] B. S. Lazarov and O. Sigmund, "Filters in topology optimization based on Helmholtz-type differential equations," *International Journal for Numerical Methods in Engineering* **86**, pp. 765–781, May 2011.
- [52] B. S. Lazarov, F. Wang, and O. Sigmund, "Length scale and manufacturability in density-based topology optimization," *Arch Appl Mech* **86**, pp. 189–218, Jan. 2016.
- [53] F. Wang, B. S. Lazarov, and O. Sigmund, "On projection methods, convergence and robust formulations in topology optimization," *Struct Multidisc Optim* **43**, pp. 767–784, June 2011.
- [54] S. Sanogo and F. Messine, "Topology optimization in electromagnetism using SIMP method: Issues of material interpolation schemes," *COMPEL - The international journal for computation and mathematics in electrical and electronic engineering* **37**, pp. 2138–2157, Oct. 2018.

- [55] M. P. Bendsøe and O. Sigmund, "Material interpolation schemes in topology optimization," *Archive of Applied Mechanics (Ingenieur Archiv)* **69**, pp. 635–654, Nov. 1999.
- [56] A. Takezawa, J. Lee, and M. Kitamura, "Design methodology of magnetic fields and structures for magneto-mechanical resonator based on topology optimization," *Optim Eng* **19**, pp. 19–38, Mar. 2018.
- [57] J. Lee, J. Lee, T. Jung, and J. Yoo, "Topology optimization for three-dimensional design of segmented permanent magnet arrays," *Struct Multidisc Optim* **62**, pp. 3089–3104, July 2020.
- [58] T. Jung, J. Lee, and J. Lee, "Design and Fabrication of Magnetic System Using Multi-Material Topology Optimization," *IEEE Access* **9**, pp. 8649–8658, 2021.
- [59] N. Aage, E. Andreassen, B. S. Lazarov, and O. Sigmund, "Giga-voxel computational morphogenesis for structural design," *Nature* **550**, pp. 84–86, Oct. 2017.
- [60] N. Aage and B. S. Lazarov, "Parallel framework for topology optimization using the method of moving asymptotes," *Struct Multidisc Optim* **47**, pp. 493–505, Apr. 2013.
- [61] F. Baudart, B. Dehez, J. Denies, M. Markovic, and Y. Perriard, "Shape optimization of flexible PCB slotless windings in BLDC machines," in *2013 International Conference on Electrical Machines and Systems (ICEMS)*, pp. 943–948, Oct. 2013.
- [62] B. Dehez, F. Baudart, M. Markovic, and Y. Perriard, "Theoretical and Experimental Investigation of Flex-PCB Air-Gap Windings in Slotless BLDC Machines," *IEEE Transactions on Industry Applications* **50**, pp. 3153–3160, Sept. 2014.
- [63] J.-K. Byun, I.-H. Park, W. Nah, J.-H. Lee, and J. Kang, "Comparison of shape and topology optimization methods for HTS solenoid design," *IEEE Transactions on Applied Superconductivity* **14**, pp. 1842–1845, June 2004.
- [64] W. J. Cheon, K. H. Lee, K. S. Seo, and I. H. Park, "Shape sensitivity analysis and optimization of current-carrying conductor for current distribution control," *IEEE Transactions on Magnetics* **54**(3), pp. 1–4, 2018.
- [65] J.-H. Lee, J.-K. Byun, K. Choi, and S.-Y. Hahn, "Faster calculation of sensitivity in the source current distribution problem using reciprocity theorem," *IEEE Transactions on Magnetics* **37**, pp. 3596–3599, Sept. 2001.
- [66] A. Canelas, A. A. Novotny, and J. R. Roche, "Topology design of inductors in electromagnetic casting using level-sets and second order topological derivatives," *Struct Multidisc Optim* **50**, pp. 1151–1163, Dec. 2014.
- [67] T. Labbe, *Topology optimization methods for the design of electromagnetic actuators*. PhD thesis, UCL - Université Catholique de Louvain, 2011.
- [68] T. Labbe and B. Dehez, "Convexity-Oriented Method for the Topology Optimization of Ferromagnetic Moving Parts in Electromagnetic Actuators Using Magnetic Energy," *IEEE Transactions on Magnetics* **46**, pp. 4016–4022, Dec. 2010.

Bibliography

- [69] J. Lee, E. M. Dede, and T. Nomura, "Simultaneous Design Optimization of Permanent Magnet, Coils, and Ferromagnetic Material in Actuators," *IEEE Transactions on Magnetics* **47**, pp. 4712–4716, Dec. 2011.
- [70] J. S. Choi and J. Yoo, "Simultaneous structural topology optimization of electromagnetic sources and ferromagnetic materials," *Computer Methods in Applied Mechanics and Engineering* **198**, pp. 2111–2121, May 2009.
- [71] W. Kim, J. E. Kim, and Y. Y. Kim, "Coil configuration design for the Lorentz force maximization by the topology optimization method: applications to optical pickup coil design," *Sensors and Actuators A: Physical* **121**, pp. 221–229, May 2005.
- [72] H. Pan, F. Jia, Z.-Y. Liu, M. Zaitsev, J. Hennig, and J. G. Korvink, "Design of small-scale gradient coils in magnetic resonance imaging by using the topology optimization method," *Chinese Physics B* **27**, p. 050201, May 2018.
- [73] K. Nomura, S. Yamasaki, K. Yaji, H. Bo, A. Takahashi, T. Kojima, and K. Fujita, "Topology optimization of conductors in electrical circuit," *Struct Multidisc Optim* **59**, p. 2205–2225, Jan. 2019.
- [74] K. Nomura, A. Takahashi, T. Kojima, S. Yamasaki, K. Yaji, H. Bo, and K. Fujita, "Topology-Optimization-Based EMC Design," in *2019 International Symposium on Electromagnetic Compatibility - EMC EUROPE*, pp. 933–937, Sept. 2019. ISSN: 2325-0364, 2325-0356.
- [75] A. J. Mäkinen, R. Zetter, J. Iivanainen, K. C. J. Zevenhoven, L. Parkkonen, and R. J. Ilmonemi, "Magnetic-field modeling with surface currents. Part I. Physical and computational principles of bfieldtools," *Journal of Applied Physics* **128**, p. 063906, Aug. 2020. Publisher: American Institute of Physics.
- [76] R. Zetter, A. J. Mäkinen, J. Iivanainen, K. C. J. Zevenhoven, R. J. Ilmonemi, and L. Parkkonen, "Magnetic-field modeling with surface currents. Part II. Implementation and usage of bfieldtools," *Journal of Applied Physics* **128**, p. 063905, Aug. 2020. Publisher: American Institute of Physics.
- [77] A. Selema, M. N. Ibrahim, and P. Sergeant, "Electrical Machines Winding Technology: Latest Advancements for Transportation Electrification," *Machines* **10**, p. 563, July 2022.
- [78] Windings, "Basic motor design tutorial." <https://www.windings.com/technical-reference/basic-motor-design-tutorial/>, 2021. Accessed: 2022-12-29.
- [79] A. GmbH, "Electric motors." <https://www.aumann.com/en/services/industry-solutions/e-mobility-automotive/electric-drive/electric-motors/>, 2021. Accessed: 2021-11-11.
- [80] Portescap, "Brushless dc motor design." <https://www.portescap.com/en/products/brushless-dc-motors/all-bl-dc-motors>, 2021. Accessed: 2022-12-29.
- [81] S. Jumayev, K. O. Boynov, J. J. H. Paulides, E. A. Lomonova, and J. Pyrhönen, "Slotless PM Machines With Skewed Winding Shapes: 3-D Electromagnetic Semianalytical Model," *IEEE Transactions on Magnetics* **52**, pp. 1–12, Nov. 2016. Conference Name: IEEE Transactions on Magnetics.

-
- [82] G. Colinet, W. Lamberts, F. Baudart, and B. Dehez, "Investigation on the potential of PCB winding technology for high-dynamic and high-precision linear actuators," in *2020 IEEE Energy Conversion Congress and Exposition (ECCE)*, pp. 3615–3622, Oct. 2020. ISSN: 2329-3748.
- [83] ECM, "Pcb stator technology." <https://pcbstator.com/technology>, 2021. Accessed: 2021-10-14.
- [84] X. Wang, H. Lu, and X. Li, "Winding Design and Analysis for a Disc-Type Permanent-Magnet Synchronous Motor with a PCB Stator," *Energies* **11**, p. 3383, Dec. 2018.
- [85] B. Dehez, F. Baudart, and Y. Perriard, "Analysis of a new topology of flexible PCB winding for slotless BLDC machines," in *2014 International Conference on Electrical Machines (ICEM)*, pp. 1963–1969, Sept. 2014.
- [86] G. Francois and B. Dehez, "Impact of slit configuration on eddy current and supply current losses in PCB winding of slotless PM machines," *IEEE Transactions on Industry Applications* -, pp. 1–1, 2022.
- [87] S. Mohan, "Thermal Comparison of FR-4 and Insulated Metal Substrate PCB for GaN Inverter," Tech. Rep. TIDA030, Texas Instruments, 2019.
- [88] A. Bandyopadhyay and K. D. Traxel, "Invited review article: Metal-additive manufacturing—Modeling strategies for application-optimized designs," *Additive Manufacturing* **22**, pp. 758–774, Aug. 2018.
- [89] A. Selema, M. N. Ibrahim, and P. Sergeant, "Metal Additive Manufacturing for Electrical Machines: Technology Review and Latest Advancements," *Energies* **15**, p. 1076, Jan. 2022.
- [90] R. Wrobel and B. Mecrow, "A Comprehensive Review of Additive Manufacturing in Construction of Electrical Machines," *IEEE Transactions on Energy Conversion* **35**, pp. 1054–1064, June 2020. Conference Name: IEEE Transactions on Energy Conversion.
- [91] H. Tiismus, A. Kallaste, A. Belahcen, A. Rassolkin, T. Vaimann, and P. Shams Ghahfarokhi, "Additive Manufacturing and Performance of E-Type Transformer Core," *Energies* **14**, p. 3278, Jan. 2021. Number: 11 Publisher: Multidisciplinary Digital Publishing Institute.
- [92] A. Drives, "3d-printed windings." <https://www.additive-drives.de/>, 2021. Accessed: 2021-11-14.
- [93] H3X, "Integrated motor drives." <https://www.h3x.tech/>, 2021. Accessed: 2021-11-14.
- [94] Q. Jiang, P. Zhang, Z. Yu, H. Shi, D. Wu, H. Yan, X. Ye, Q. Lu, and Y. Tian, "A Review on Additive Manufacturing of Pure Copper," *Coatings* **11**, p. 740, June 2021.
- [95] F. Wu, A. M. EL-Refaie, and A. Al-Qarni, "Additively Manufactured Hollow Conductors for High Specific Power Electrical Machines: Aluminum vs Copper," in *2021 IEEE Energy Conversion Congress and Exposition (ECCE)*, pp. 4397–4404, Oct. 2021. ISSN: 2329-3748.

Bibliography

- [96] T. Q. Tran, A. Chinnappan, J. K. Y. Lee, N. H. Loc, L. T. Tran, G. Wang, V. V. Kumar, W. a. D. M. Jayathilaka, D. Ji, M. Doddamani, and S. Ramakrishna, "3D Printing of Highly Pure Copper," *Metals* **9**, p. 756, July 2019. Number: 7 Publisher: Multidisciplinary Digital Publishing Institute.
- [97] F. Wu and A. M. EL-Refaie, "Minimization of Winding AC Losses Using Inhomogeneous Electrical Conductivity Enabled by Additive Manufacturing," in *2020 IEEE Energy Conversion Congress and Exposition (ECCE)*, pp. 3607–3614, Oct. 2020. ISSN: 2329-3748.
- [98] N. Simpson, S. P. Munagala, A. Catania, F. Derguti, and P. H. Mellor, "Functionally graded electrical windings enabled by additive manufacturing," in *2022 International Conference on Electrical Machines (ICEM)*, pp. 1477–1483, 2022.
- [99] F. Wu, A. M. EL-Refaie, and A. Al-Qarni, "Additively manufactured hollow conductors integrated with heat pipes: Design tradeoffs and hardware demonstration," *IEEE Transactions on Industry Applications* **57**(4), pp. 3632–3642, 2021.
- [100] C. Wohlers, P. Juris, S. Kabelac, and B. Ponick, "Design and direct liquid cooling of tooth-coil windings," *Electr Eng* **100**, pp. 2299–2308, Dec. 2018.
- [101] F. Lorenz, J. Rudolph, and R. Werner, "Design of 3D Printed High Performance Windings for Switched Reluctance Machines," in *2018 XIII International Conference on Electrical Machines (ICEM)*, p. 7, 2018.
- [102] F. Lorenz, J. Rudolph, and R. Werner, "High Temperature Operation and Increased Cooling Capabilities of Switched Reluctance Machines using 3D Printed Ceramic Insulated Coils," in *2018 IEEE Transportation Electrification Conference and Expo (ITEC)*, pp. 400–405, 2018.
- [103] "1910-1919 Roebel bars and turbines." <https://web.archive.org/web/20131030063807/http://www.abb.de/cawp/deabb201/16e1e5d67c1fe37ac12569fb003f506a.aspx>, Oct. 2013.
- [104] D. C. MacDonald, "Losses in Roebel bars: Effect of slot portion on circulating currents," *Proceedings of the Institution of Electrical Engineers* **117**, pp. 111–118, Jan. 1970.
- [105] D. C. MacDonald, "Circulating-current loss within Roebel-bar stator windings in hydro-electric alternators," *Proceedings of the Institution of Electrical Engineers* **118**, pp. 689–697, May 1971.
- [106] J. Jung, A. Helm, and J. Liebold, "Improved Efficiency of Electric Drives with Additively Manufactured Roebel Bar Windings," *MTZ Worldw* **82**, pp. 54–58, Apr. 2021.
- [107] N. Simpson, D. J. North, S. M. Collins, and P. H. Mellor, "Additive Manufacturing of Shaped Profile Windings for Minimal AC Loss in Electrical Machines," *IEEE Transactions on Industry Applications* **56**, pp. 2510–2519, May 2020. Conference Name: IEEE Transactions on Industry Applications.
- [108] N. Simpson, J. Jung, A. Helm, and P. Mellor, "Additive Manufacturing of a Conformal Hybrid-Strand Concentrated Winding Topology for Minimal AC Loss in Electrical Machines," in *2021 IEEE Energy Conversion Congress and Exposition (ECCE)*, pp. 3844–3851, Oct. 2021. ISSN: 2329-3748.

-
- [109] A. Selema, M. N. Ibrahim, and P. Sergeant, "Additively-Manufactured Ultra-Light Shaped-Profile Windings for HF Electrical Machines and Weight-Sensitive Applications," *IEEE Transactions on Transportation Electrification* **8**(4), pp. 4313–4324, 2022.
 - [110] I. H. Park, *Design Sensitivity Analysis and Optimization of Electromagnetic Systems*, Mathematical and Analytical Techniques with Applications to Engineering, Springer, Singapore, 2019.
 - [111] H. P. Langtangen and K.-A. Mardal, *Quick Overview of the Finite Element Method*, Texts in Computational Science and Engineering, Springer International Publishing, Cham, 2019.
 - [112] P. Instrumente, "Pi ironless linear motors." <https://www.youtube.com/watch?v=hX6lSAvjqms>, 2015. Accessed: 2019-01-11.
 - [113] F. Foundation, "Linear motors." <https://fab.cba.mit.edu/classes/865.18/motion/linear/index.html>, 2018. Accessed: 2022-12-29.
 - [114] P. E. Farrell, D. A. Ham, S. W. Funke, and M. E. Rognes, "Automated Derivation of the Adjoint of High-Level Transient Finite Element Programs," *SIAM Journal on Scientific Computing* **35**, pp. C369–C393, Jan. 2013. Publisher: Society for Industrial and Applied Mathematics.
 - [115] M. Stolpe and K. Svanberg, "An alternative interpolation scheme for minimum compliance topology optimization," *Structural and Multidisciplinary Optimization* **22**, pp. 116–124, Sept. 2001.
 - [116] M. Stolpe and K. Svanberg, "On the trajectories of penalization methods for topology optimization," *Structural and Multidisciplinary Optimization* **21**, pp. 128–139, Apr. 2001.
 - [117] M. Alnæs, J. Blechta, J. Hake, A. Johansson, B. Kehlet, A. Logg, C. Richardson, J. Ring, M. E. Rognes, and G. N. Wells, "The FEniCS Project Version 1.5," *Archive of Numerical Software* **3**, Dec. 2015.
 - [118] S. K. Mitusch, S. W. Funke, and J. S. Dokken, "Dolfin-adjoint 2018.1: Automated adjoints for FEniCS and Firedrake," *Journal of Open Source Software* **4**, p. 1292, June 2019.
 - [119] I. S. Duff, "MA57—a code for the solution of sparse symmetric definite and indefinite systems," *ACM Trans. Math. Softw.* **30**, pp. 118–144, June 2004.
 - [120] N. Ryu, W. S. Song, Y. Jung, and S. Min, "Multi-Objective Topology Optimization of a Magnetic Actuator Using an Adaptive Weight and Tunneling Method," *IEEE Transactions on Magnetics* **55**, pp. 1–4, June 2019.
 - [121] N. Ryu, M. Seo, and S. Min, "Multi-objective topology optimization incorporating an adaptive weighed-sum method and a configuration-based clustering scheme," *Computer Methods in Applied Mechanics and Engineering* **385**, p. 114015, Nov. 2021.
 - [122] Tokamac, "English: Illustration of the right-hand rule for the Lorentz force, cross product of an electric current with a magnetic field.." https://commons.wikimedia.org/wiki/File:Right_hand_rule_cross_product_F%3DJ%C3%97B.svg, Apr. 2018. Accessed: 2022-12-01.

Bibliography

- [123] A. Thabuis, X. Ren, G. Burnand, and Y. Perriard, "Density-Based Topology Optimization of Conductor Paths for Windings in Slotted Electrical Machines," in *2019 22nd International Conference on Electrical Machines and Systems (ICEMS)*, pp. 1–6, Aug. 2019.
- [124] S. Xu, J. Liu, B. Zou, Q. Li, and Y. Ma, "Stress constrained multi-material topology optimization with the ordered SIMP method," *Computer Methods in Applied Mechanics and Engineering* **373**, p. 113453, Jan. 2021.
- [125] A. Thabuis, X. Ren, and Y. Perriard, "Topology Optimization of Motor Windings for Coreless Electrical Machines," Apr. 2023.
- [126] C. Inc., "Comsol." <http://www.comsol.com/products/multiphysics/>, 2020. Accessed: 2021-11-14.
- [127] S. Schuerle, S. Erni, M. Flink, B. E. Kratochvil, and B. J. Nelson, "Three-Dimensional Magnetic Manipulation of Micro- and Nanostructures for Applications in Life Sciences," *IEEE Transactions on Magnetics* **49**, pp. 321–330, Jan. 2013. Conference Name: IEEE Transactions on Magnetics.
- [128] L. Manamanchaiyaporn, T. Xu, and X. Wu, "Magnetic Soft Robot With the Triangular Head–Tail Morphology Inspired By Lateral Undulation," *IEEE/ASME Transactions on Mechatronics* **25**, pp. 2688–2699, Dec. 2020. Conference Name: IEEE/ASME Transactions on Mechatronics.
- [129] A. Thabuis, X. Ren, T. Duong, and Y. Perriard, "Exploring Beyond the Helmholtz Coils for Uniform Magnetic Field Generation With Topology Optimization," *IEEE Transactions on Magnetics* **58**, pp. 1–4, Sept. 2022.
- [130] J. J. Abbott, "Parametric design of tri-axial nested Helmholtz coils," *Review of Scientific Instruments* **86**, p. 054701, May 2015. Publisher: American Institute of Physics.
- [131] A. Thabuis, M. C. Rivera, X. Ren, and Y. Perriard, "Topology optimization of an electro-magnet manipulator for 3-d uniform magnetic field generation," *IEEE Transactions on Magnetics* **59**(5), pp. 1–4, 2023.
- [132] M. Sarap, A. Kallaste, P. Shams Ghahfarokhi, H. Tiismus, and T. Vaimann, "Utilization of Additive Manufacturing in the Thermal Design of Electrical Machines: A Review," *Machines* **10**, p. 251, Apr. 2022. Number: 4 Publisher: Multidisciplinary Digital Publishing Institute.
- [133] M. Wüthrich, M. Gubser, W. J. Elspass, and C. Jaeger, "A Novel Slicing Strategy to Print Overhangs without Support Material," *Applied Sciences* **11**, p. 8760, Jan. 2021. Number: 18 Publisher: Multidisciplinary Digital Publishing Institute.
- [134] Protiq, "Unique copper inducers from 3d printing." <https://www.protiq.com/en/3d-printing/service/copper-inductor/>, 2020. Accessed: 2020-10-09.
- [135] A. Thabuis, X. Ren, and Y. Perriard, "Enhanced electric motors using multi-functional 3d printed winding with integrated heat sinks," *IEEE Transactions on Energy Conversion*, pp. 1–11, 2022.

- [136] B. Guillaume, *Small scale very high speed slotless permanent magnet motors*. PhD thesis, Ecole Polytechnique Federale de Lausanne (EPFL), 2020.
- [137] V. Madonna, A. Walker, P. Giangrande, G. Serra, C. Gerada, and M. Galea, “Improved Thermal Management and Analysis for Stator End-Windings of Electrical Machines,” *IEEE Transactions on Industrial Electronics* **66**, pp. 5057–5069, July 2019. Conference Name: IEEE Transactions on Industrial Electronics.
- [138] H. Jichao, D. Jiechen, W. Yang, W. Chao, G. Baojun, and L. Weili, “Coupled Electromagnetic-Fluid-Thermal Analysis for End Zone With Electric Screen in Large Water-Hydrogen-Hydrogen Cooled Turbine Generator Under Different End Winding Extensions,” *IEEE Transactions on Energy Conversion* **36**, pp. 2703–2713, Dec. 2021.
- [139] R. Wrobel, “A technology overview of thermal management of integrated motor drives – Electrical Machines,” *Thermal Science and Engineering Progress* **29**, p. 101222, Mar. 2022.
- [140] H. E. Ahmed, B. H. Salman, A. S. Kherbeet, and M. I. Ahmed, “Optimization of thermal design of heat sinks: A review,” *International Journal of Heat and Mass Transfer* **118**, pp. 129–153, Mar. 2018.
- [141] N. Verbeek, S. Favresse, F. Baudart, and B. Dehez, “Estimation of Equivalent Thermal Conductivity of PCB Airgap Windings,” in *2022 International Conference on Electrical Machines (ICEM)*, pp. 1362–1368, Sept. 2022. ISSN: 2381-4802.
- [142] F. Farahmand, F. P. Dawson, and J. Douglas Lavers, “Temperature rise and free-convection heat-transfer coefficient for two-dimensional pot-core inductors and transformers,” *IEEE Transactions on Industry Applications* **45**(6), pp. 2080–2089, 2009.
- [143] X. Ren, A. Thabuis, and Y. Perriard, “Innovative design of 3d-printed winding for linear motor,” in *2022 25th International Conference on Electrical Machines and Systems (ICEMS)*, pp. 1–6, 2022.
- [144] M. Rafiee, R. D. Farahani, and D. Therriault, “Multi-Material 3D and 4D Printing: A Survey,” *Advanced Science* **7**(12), p. 1902307, 2020. _eprint: <https://onlinelibrary.wiley.com/doi/pdf/10.1002/adv.201902307>.
- [145] G. L. Goh, H. Zhang, T. H. Chong, and W. Y. Yeong, “3D Printing of Multilayered and Multimaterial Electronics: A Review,” *Advanced Electronic Materials* **7**(10), p. 2100445, 2021. _eprint: <https://onlinelibrary.wiley.com/doi/pdf/10.1002/aelm.202100445>.
- [146] J. Persad and S. Rocke, “Multi-material 3D printed electronic assemblies: A review,” *Results in Engineering* **16**, p. 100730, Dec. 2022.
- [147] M. Bhuvanesh Kumar and P. Sathiya, “Methods and materials for additive manufacturing: A critical review on advancements and challenges,” *Thin-Walled Structures* **159**, p. 107228, Feb. 2021.
- [148] Britannica, “3d printing - illustration of the selective laser sintering (sls) process.” <https://www.britannica.com/technology/3D-printing>. Accessed: 2023-01-26.

Bibliography

- [149] J. J. S. Dilip, S. Zhang, C. Teng, K. Zeng, C. Robinson, D. Pal, and B. Stucker, "Influence of processing parameters on the evolution of melt pool, porosity, and microstructures in Ti-6Al-4V alloy parts fabricated by selective laser melting," *Progress in Additive Manufacturing* **2**, pp. 157–167, Sept. 2017.
- [150] A. Keshavarzkermani, E. Marzbanrad, R. Esmailizadeh, Y. Mahmoodkhani, U. Ali, P. D. Enrique, N. Y. Zhou, A. Bonakdar, and E. Toyserkani, "An investigation into the effect of process parameters on melt pool geometry, cell spacing, and grain refinement during laser powder bed fusion," *Optics & Laser Technology* **116**, pp. 83–91, Aug. 2019.
- [151] H. Ghasemi-Tabasi, J. Jhabvala, E. Boillat, T. Ivas, R. Drissi-Daoudi, and R. E. Logé, "An effective rule for translating optimal selective laser melting processing parameters from one material to another," *Additive Manufacturing* **36**, p. 101496, Dec. 2020.
- [152] StenaAluminium, "Alloy Specifications." <https://www.stenaaluminium.com/Aluminium-alloys-and-services/alloy-specifications/>, 2022. Accessed: 2022-02-22.
- [153] A. Williams, "Solder to aluminum." <https://hackaday.com/2020/06/11/solder-to-aluminum/>, 2021. Accessed: 2021-11-14.
- [154] Vidyawire, "Explained: The importance of pinhole testing for enameled copper wires." <https://www.vidyawire.com/explained-the-importance-of-pinhole-testing-for-enameled-copper-wires/>, 2022. Accessed: 2022-01-25.
- [155] M. Sarap, A. Kallaste, P. S. Ghahfarokhi, H. Tiismus, and T. Vaimann, "The Effect of Build Direction on the Thermal Conductivity of Additively Manufactured AlSi10Mg and Silicon-steel Samples," in *2022 International Conference on Electrical Machines (ICEM)*, pp. 538–543, Sept. 2022. ISSN: 2381-4802.
- [156] M. Sarap, A. Kallaste, P. S. Ghahfarokhi, H. Tiismus, and T. Vaimann, "Determining the Thermal Conductivity of Additively Manufactured Metal Specimens," in *2022 29th International Workshop on Electric Drives: Advances in Power Electronics for Electric Drives (IWED)*, pp. 1–4, Jan. 2022. ISSN: 2767-7842.
- [157] H. PureForm, "Holo additive manufacturing." <https://holoam.com/>, 2021. Accessed: 2021-11-14.
- [158] F. Campelo, S. Ota, K. Watanabe, and H. Igarashi, "Generating Parametric Design Models Using Information From Topology Optimization," *IEEE Transactions on Magnetics* **44**, pp. 986–989, June 2008.
- [159] A. Amroune, J.-C. Cuillière, and V. François, "Automated Lofting-Based Reconstruction of CAD Models from 3D Topology Optimization Results," *Computer-Aided Design* **145**, p. 103183, Apr. 2022.
- [160] C. R. Vargas-Llanos, F. Huber, N. Riva, M. Zhang, and F. Grilli, "3D homogenization of the T-A formulation for the analysis of coils with complex geometries," *Superconductor Science and Technology* **35**, p. 124001, Oct. 2022. Publisher: IOP Publishing.

- [161] N. Simpson, G. Yiannakou, H. Felton, J. Robinson, A. Arjunan, and P. H. Mellor, “Direct Thermal Management of Windings enabled by Additive Manufacturing,” *IEEE Transactions on Industry Applications*, pp. 1–9, 2022.
- [162] A. Thabuis, A. Fasolo, D. Veronesi, R. Xiaotao, and Y. Perriard, “High-Performance Coil for Electrical Machine and Coil Assembly for a Linear Motor.” <https://worldwide.espacenet.com/patent/search/family/076011813/publication/EP4092878A1?q=pn%3DEP4092878A1>, Nov. 2022.
- [163] M. Jufer, *Electromécanique*, PPUR presses polytechniques, 1995. Google-Books-ID: xX7dD7_brXgC.

Adrien Thabuis

born on August 3rd 1994
in Ambilly, France
adrien.thabuis@gmail.com
Google Scholar
Linkedin



Education

- Jan 2019 - Apr 2023 **Ph.D. in Advanced Manufacturing**
Integrated Actuators Laboratory, EPFL, Switzerland
"Computational Design and Additive Manufacturing of Electromagnetic Coils"
Thesis Director: Prof. Yves Perriard
- Sep 2012 - Aug 2018 **Master in Micro-Engineering**
EPFL, Switzerland
Specialized in Robotics.

Professional Experience

- Jan 2019 - Apr 2023 **Doctoral Assistant - EPFL**, Neuchâtel Switzerland: Teaching assistant for the "Electromagnetic actuators and systems" and "Electrotechnics" courses. - Supervisor of Master theses and student projects.
- Feb 2018 - Aug 2018 **Visiting master student - Tokyo Institute of Technology**, Tokyo Japan: Master Thesis in Chiba lab. on the Design of a novel type of electromagnetic actuator for exoskeletons and humanoid robots
- July 2017 - Sep 2017 **Engineering Intern - Motosacoche**, Geneva Switzerland: - Design and construction of a new E-Moped (Cyclomoteur) of 1000W.

Skills

Python, Matlab, C++, Finite Element Analysis (COMSOL, ANSYS, open-source libraries), Optimization, Inventor, Solidworks, Machining, Soldering, Additive Manufacturing, Actuator Design, Automation, Project Management.